ULTRAHIGH RESOLUTION OPTICAL SPECTROSCOPY OF LIQUID MICRODROPLETS USING TAPERED OPTICAL FIBER WAVEGUIDES

by

Yasin Karadağ

A Thesis Submitted to the
Graduate School of Sciences and Engineering
in Partial Fulfillment of the Requirements for
the Degree of

Doctor of Philosophy

in

Physics

Koç University

October, 2013

Koç University

Graduate School of Sciences and Engineering

This is to certify that I have examined this copy of a doctoral dissertation by

Yasin Karadağ

and have found that it is complete and satisfactory in all respects,
and that any and all revisions required by the final
examining committee have been made.

Committee Members:

_____

Alper Kiraz, Ph. D.(Advisor)

_____

Metin Muradoğlu, Ph. D.

_____

Kaan Güven, Ph. D.

_____

Alexandr Jonáš, Ph. D.

_____

Selçuk Aktürk, Ph. D.

Date: _____

ABSTRACT

Optofluidics is a new research field that exploits unique properties of fluids for creating optical components and systems. Optofluidic devices combined with accurate control of liquids on small spatial scale via microfluidic technologies pave way for improved chemical and biological functionality in lab-on-a-chip analytical and preparative systems. Main advantages of such integrated systems are their compactness and direct compatibility with biological specimens. Examples of applications of integrated optofluidics include optical communication components, organic dye-based laser light sources, or biological sensing. Microdroplets, with their spherical gemetry and exceptionally smooth surfaces are ideally suited for applications in optofluidics. It is well known that spherical dielectric microobjects can act as optical resonators hosting so-called whispering gallery modes (WGMs) - optical resonances that possess very high quality factors while being confined to relatively small volumes near the microobject's rim. Consequently, very high optical field density can be achieved in microdroplets that can have already found many applications in quantum and nonlinear optics. Fundamental studies in cavity quantum electrodynamics have led to the demonstration of manipulation of the spontaneous emission rate of dye molecules. Dye lasing, stimulated Raman scattering, and Raman lasing in microdroplets have also been demonstrated at low pump threshold powers. Apart from their significance for the fundamental physics research, microdroplets are well suited to another important line of applications that benefit from the sensitivity of the WGMs to the microdroplet size as well as the refractive indices of the inner liquid and the outer medium. These properties naturally make microdroplets very attractive in biological and chemical sensing, and in developing optical devices that necessitate a tunable optical microcavity, e.g. tunable optical switches or light sources.

In order to utilize microdroplets in optofluidic applications, one must be able to stabilize their position in a controlled way. In this thesis, superhydrophobic surfaces were used to stabilize droplet position. Surface-supported microdroplets can host high-quality WGMs

and thus, they represent an ideal model system for studying fundamental optical properties and applications of liquid-based optical resonant cavities. The thesis is organized as follows..

In the first part, we introduce a novel method for the microscopic contact angle measurement that is based on the analysis of mechanical resonances of individual micrometer-sized liquid droplets supported by a vibrated superhydrophobic surface. Fluorescence spectra of the dye-doped droplets excited by laser light feature whispering gallery modes (WGMs) whose spectral widths depend on the droplet vibration amplitude, thus enabling precise measurements of the droplet mechanical resonant frequency. Following droplet size determination by WGM mode-matching, we calculate the contact angles from the dependence of the measured mechanical resonant frequency on the droplet size for two surfaces with different superhydrophobicity levels, and a good correlation with the values measured by direct imaging of millimeter-sized droplets is found. In addition to that oscillatory deformations of micrometer-sized NaCl-water droplets by an AC electric field are used for contact angle measurements on superhydrophobic surfaces.

In the second part, tapered optical fiber waveguide coupling is used instead of free-space coupling of light into the surface-supported droplets. Fiber tapers allow selective phase-matched excitation of individual WGMs with a spectral resolution limited only by the linewidth of the laser used. We measured ultrahigh quality factors (Q-factors) of the optical whispering-gallery modes excited via a tapered optical-fiber waveguide in single glycerol-water microdroplets standing on a superhydrophobic surface in air. Owing to the high contact angle of glycerol-water mixture on the superhydrophobic surface ($> 155°$), droplets with the geometry of a truncated sphere minimally distorted by gravity and contact line pinning effects could be generated. Q-factors up to 2.3×10^6 were observed for such droplets with radii of $100 - 200 \, \mu\text{m}$ exposed to the ambient atmosphere in a closed chamber with controlled relative humidity. Placement of microdroplets in a constant humidity environment permitted prolonged characterization of Q-factors of individual microdroplets. We found that the Q-factors of liquid droplets in air were stable over more than an hour and their measured values were limited mostly by the thermally-induced droplet shape fluctuations.

In the last part, we demonstrate long-term stabilization of the size of liquid optical microcavities based on surface-supported salt-water microdroplets surrounded by air. Single

tapered optical fibers were used to couple the light from independent heating and probe lasers into individual microdroplets that were kept on a superhydrophobic surface in a high-humidity chamber. Size stabilization of microdroplets resulted from competition between resonant absorption of the infrared heating laser by a microdroplet whispering gallery mode and water condensation in the sample chamber. Microdroplet size was continuously monitored using the tunable red probe laser. Thanks to the narrow linewidth of the heating laser, stabilization of the 110 μm radius of a microdroplet with a precision down to 0.54 nm was achieved for a period of 410 s. Additionally, we demonstrate controllable tuning of size of self-stabilized surface-supported liquid aerosols using a tunable IR heating laser which has a very narrow linewidth.

ÖZETÇE

Optofluidik, optik bileşenleri ve sistemleri oluşturmak için akışkanların eşsiz özelliklerini kullanan yeni bir araştırma alanıdır. Optofluidik cihazlar analitik entegre sistemlerin kimyasal ve biyolojik özellikleri incelenebilir. Entegre sistemlerin en büyük özelliği karmaşık olmamaları ve biyolojik örneklerle uyumlu olmalarıdır. Optik iletişim bileşenleri, organik boya bazlı lazer ışık kaynakları ya da biyolojik algılama entegre opto-akışkan uygulamaların örneklerindendir. Küresel simetrileriye ve yüzey pürüzsüzlüğüne sahip mikrodamlalar optofluidik uygulamaları için uygundur. Mikrodamlacıkların optofluidik uygulamaları için pozisyonlarının kontrollü bir şekilde sabitlenmesi gerekmektedir. Bu tezde damlacıkların pozisyonlarının sabitlenmesi için su tutmayan yüzeyler kullanılmıştır. Tezin ilk kısmında, titreştirilen süperhidrofobik bir yüzey üzerinde bulunan mikrometre ölçekli bireysel sıvı damlalarının mekanik rezonanslarının analizine bağlı olarak mikroskopik kontak açılarının ölçümü için yeni bir metot bulunmuştur. Bu amaçla, bu çalışmada, damlacığın mekanik rezonanslarının ve büyüklüklerinin eşzamanlı olarak belirlenebilmesi için ışıyan boya içeren damlacıkların lazer ışınıyla uyarılmasıyla elde edilen fısıldayan galeri kiplerinin (FGM) optik spektroskopisi kullanılmıştır. Damlacıklar, optik mikrokovuk rolü üstlenmişlerdir ve damlacıkların ışıma spektrumu, spektral genişlikleri damlacığın titreşim genliklerine bağlı olan fısıldayan galeri kiplerini karakterize eder. Fısıldayan galeri kipinin genişliğini, farklı büyüklüklü damlaların altlık titreşim frekanslarının bir fonksiyonu olarak izleyerek, damlacıkların maksimal fısıldayan galeri kiplerinin genişlemesinin olduğu frekanslardaki rezonans frekansları belirlenmiştir. Ardından, damlacık büyüklüğü, Lorenz-Mie saçılma teorisi kullanılmasıyla fısıldayan galeri kiplerin kip-eşleştirmesi ile belirlenmiştir. Verilen bir damlacık için, kontak açısı, yüzeyde duran damlacığın aksisimektrik salınımları için geliştirilen teori kullanılarak, damlacık mekanik rezonans frekansının ve büyüklüğünün bağımsız ölçümlerinden elde edilmiştir. Tezin ikinci kısmında ise inceltilmiş optik fiber kullanılmıştır. İnceltilmiş optik fiber ile damlacıkların FGMlerinin kalite faktörleri ölçülmüştür. Daha sonra ikinci bir lazer kullanarak damlacıkların hacmi sabitlenmiş ve FGMleri kontrol edilebilmiştir.

ACKNOWLEDGMENTS

TABLE OF CONTENTS

---

[1]This work has been published in "Probing Microscopic Wetting Properties of Superhydrophobic Surfaces by Vibrated Micrometer-Sized Droplets", Langmuir 27 (6), 2150-2154 (2011)

[2]This work has been published in "Determination of Microdroplet Contact Angles Using Electrically Driven Droplet Oscillations",Appl. Phys. Lett. 98, 194101 (2011)

[3]This work has been published in "Probing of ultrahigh optical Q-factors of individual liquid microdroplets in air using tapered optical fiber waveguides", J. Opt. Soc. Am. B 29 (12), 3240-3247 (2012)

---

[4]This work has been published in "Size-stabilization of surface-supported liquid aerosols using tapered optical fiber coupling", Opt. Lett. 38 (5), 793-795 (2013)

LIST OF TABLES

LIST OF FIGURES

xvii

NOMENCLATURE

a	microdroplet radius
x_A	mole fraction of water
$x_B = (1 - x_A)$	mole fraction of glycerol
V_A	molar volume of water
$V_m = x_A V_A + x_B V_B$	molar volume of the microdroplet
R	gas constant
$\Delta H_{vap,A}$	latent heat of vaporization of water
$\Delta H_{vap,B}$	latent heat of vaporization of glycerol
C_{PA}	molar heat capacity of water
$C_{PL} = x_A C_{PA} + x_B C_{PB}$	molar heat capacity of the microdroplet
D_A	gas phase diffusion coefficient of water in air
k_a	thermal conductivity of air
k_s	thermal conductivity of the substrate
T_∞	temperature of air in the chamber
$P_A^0(T)$	vapor pressure of water at temperature T
$P_B^0(T)$	vapor pressure of glycerol at temperature T
S_A	saturation ratio of water in air
N_A	number of moles of water in the microdroplet
$N = x_A N_A + x_B N_B$	total number of moles in the microdroplet
n_A	refractive index of water at 1064 nm
$\tilde{Q}_{abs}$	modified absorbtion efficiency
γ	surface tension
S_{in}	input signal
S_{out}	output signal
τ_o	intrinsic photon lifetime
$\Delta\lambda$	free spectral range

<div align="center">

Chapter 1

INTRODUCTION

</div>

1.1   Thesis Motivation

Optofluidics is a thrilling new research field that exploits unique properties of fluids for creating optical components and systems [1]. As fluids provide a great flexibility in shape and refractive index and enable generation of optically smooth interfaces, they can be used for designing novel optical devices that cannot be realized with classical solid materials. In addition to inspiring novel all-optical applications, optofluidic devices combined with accurate control of liquids on small spatial scale via microfluidic technologies pave way for improved chemical and biological functionality in lab-on-a-chip analytical and preparative systems. Main advantages of such integrated systems are their compactness and direct compatibility with biological specimens. Examples of applications of integrated optofluidics include optical communication components, organic dye-based laser light sources [2], or biological sensing.
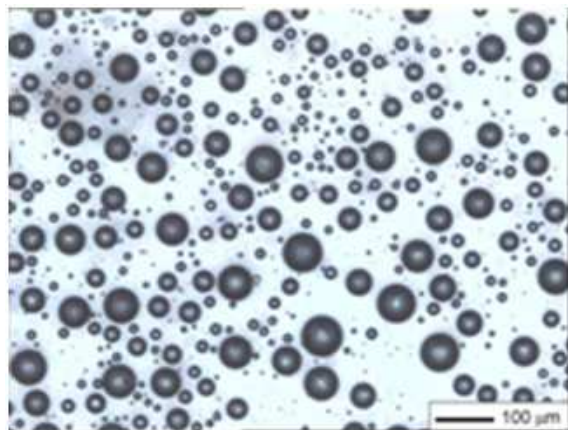
Figure 1.1: Top view of water microdroplets standing on a superhydrophobic surface

Microdroplets, with their spherical geometry and exceptionally smooth surfaces (see Fig. 1.1), are ideally suited for applications in optofluidics. It is well known that spherical dielectric microobjects can act as optical resonators hosting so-called whispering gallery modes (WGMs) - optical resonances that possess very high quality factors while being confined to relatively small volumes near the microobject's rim. Consequently, very high optical field density can be achieved in microdroplets that can mediate strong couplings between light and quantum systems (atoms, molecules, or quantum dots). Such strong couplings have already found many applications in quantum and nonlinear optics [3]. Fundamental studies in cavity quantum electrodynamics have led to the demonstration of manipulation of the spontaneous emission rate of dye molecules. Dye lasing, stimulated Raman scattering, and Raman lasing in microdroplets have also been demonstrated at low pump threshold powers. Apart from their significance for the fundamental physics research, microdroplets are well suited to another important line of applications that benefit from the sensitivity of the WGMs to the microdroplet size as well as the refractive indices of the inner liquid and the outer medium. These properties naturally make microdroplets very attractive in biological and chemical sensing, and in developing optical devices that necessitate a tunable optical microcavity, e.g. tunable optical switches or light sources [4]. In order to utilize microdroplets in optofluidic applications, one must be able to stabilize their position in a controlled way. Efforts to stabilize the position of liquid droplets date back to Millikan's famous oil drop experiment where droplets charged with only a few electrons were electrically levitated. For almost thirty years electrodynamic levitation [5], optical levitation [6], and optical tweezing [7] have been employed to study individual microdroplets over extended periods of time in optical spectroscopy experiments. Despite allowing many seminal demonstrations in quantum and nonlinear optics, chemical physics, aerosol science, and biophysics, these techniques suffered from fragility and did not allow integration with other optoelectronic components such as fiber optic cables, waveguides, or electrical contacts. Carefully optimized solid support substrates provide the way for incorporating intriguing optical properties of microdroplets into optofluidic devices. Microdroplets of water and other hydrophilic liquids take almost spherical shapes when standing on a superhydrophobic surface (see Fig. 1.1). Because of their small size (typical range of diameters between 10 and 100 microns) the shape of the droplets is dominated by surface tension with a negligible

influence of gravity-induced shape distortion. With their truncated-sphere geometry, these surface-supported microdroplets can host high-quality WGMs. For a well-leveled support substrate, the droplet's position is stable and its optical properties can be readily analyzed. In addition to preserving the sphericity of the microdroplets and increasing the robustness of the experimental configuration, the presence of a superhydrophobic surface also facilitates the integration of the liquid microdroplets within novel lab-on-a-chip optoelectronic devices.

The experimental setup that is used for the characterization of ultrahigh Q optical cavity whispering gallery modes (WGMs) is shown in Fig. 1.2. A tapered optical fiber is brought to the vicinity of a microdroplet standing on a superhydrophobic surface kept in a humidity chamber. Subsequently, the light launched into the fiber can be coupled into the studied microdroplet, thus exciting WGMs. This experimental configuration is frequently adopted in characterizing solid microsphere and microtoroid microcavities as well as photonic crystal defect nanocavities [8].

Q-factor measurements are based on coupling a tunable narrow-linewidth laser to a tapered optical fiber positioned in the vicinity of the microdroplet and monitoring fiber transmission as a function of the laser frequency. At light frequencies resonant with individual WGMs, optical coupling between the fiber and the microdroplet increases dramatically, resulting in decreased transmission. The transmission curve recorded as a function of the laser frequency features dips of finite spectral width localized at resonant frequencies; it is this spectral width together with the central frequency of the dip that reveal directly the ultrahigh optical Q-factors of the WGMs. The maximal Q-factor measurable with this technique is inversely proportional to the bandwidth of the laser. For our case, the central wavelength of the tunable external cavity diode laser used in the experiments (New Focus Velocity 6304) will be 635 nm and its typical linewidth 300 kHz. Hence, the maximum Q-factor that can be measured is found to be $\approx 10^8$. This upper limit is sufficient for our studies because even for very large microdroplets, the Q-factors are expected to be limited to $\approx 10^8$ due to the residual absorption of the droplet liquid at the central wavelength used [9] (water absorption coefficient at 635 nm is $\approx 10^{-3} cm^{-1}$. The experimental configuration shown in Fig. 1.2 allowed the characterization of the microdroplets with relatively large diameters (>10 μm). We studied the influence of the droplet size, shape (adjustable
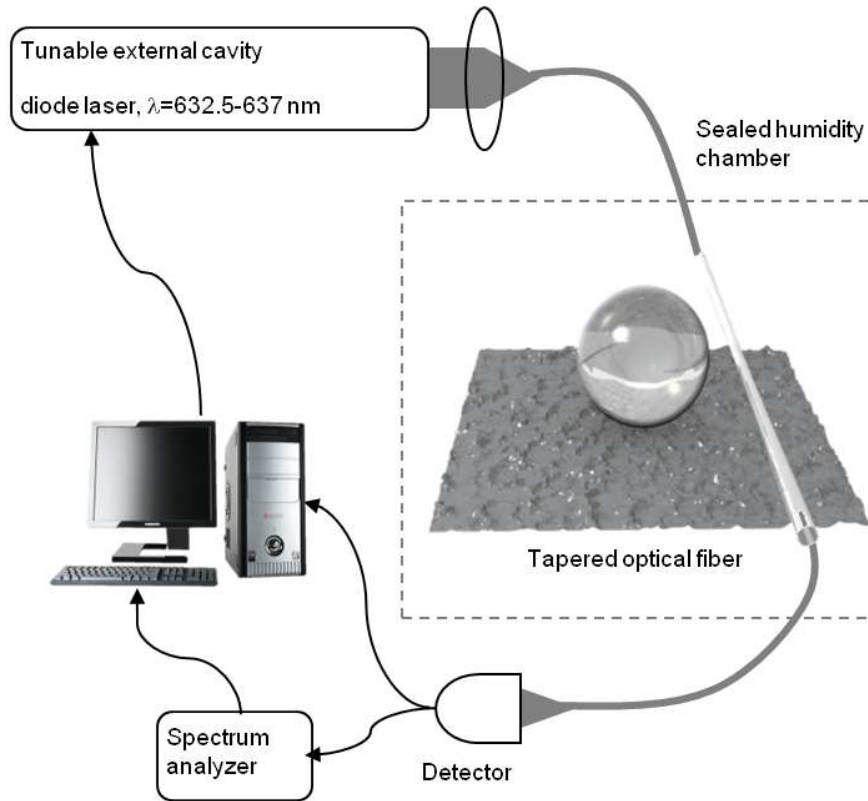
Figure 1.2: Illustration of the experimental setup that is used in characterizing ultrahigh quality WGMs and studying opto-mechanical coupling.

using the electric field), and refractive index on the attainable optical Q-factors. Composition of the droplets was adjusted by mixing suitable fluids (e.g. water and glycerol). It was expected to influence simultaneously both the optical and mechanical properties of the microdroplets through the variations of the liquid refractive index, viscosity, surface tension, and mass density. Preparation of tapered optical fibers and achievement of optimal coupling conditions between tapered fibers and microdroplets were the essential steps of the experiments. In order to obtain efficient coupling of light from the fiber into the microdroplet, the diameter of the tapered part of the fiber was appropriately chosen to fulfill phase-matching conditions of the fiber and droplet optical modes [10]. We adopted the standard flame technique that relies on heating of a small portion of the target fiber with a gas flame while pulling simultaneously on both fiber ends [8]. In order to achieve the desired properties of the taper (length, diameter), the position of the flame relative to the fiber and

the pulling speed had to be precisely controlled. During taper fabrication procedure, the fiber properties was monitored by recording the fiber transmission at the central wavelength used for optical Q-factor measurements.

1.2   Thesis Outline

In **Chapter 2**, optical modes and the quality factor (Q) of a microsphere based optical resonator are discussed.

Chapter 3 explains the superhydrophobic surface preparation and the lumped equation model for the evaporation and growth of water-glycerol and NaCl-water microdroplets standing on a superhydrophobic surface due to local heating by a focused infrared laser.

In **Chapter 4**, we report a contact angles measurement technique of micrometer-sized NaCl-water droplets on superhydrophobic surfaces by analyzing their lowest-order axisymmetric vibrational resonances driven by vertical oscillations of the surface

In **Chapter 5**, we describe the experimental infrastructure for fiber-tapering and high-Q factor measurement.

In **Chapter 6**, we demonstrate measurements of ultrahigh quality factors (Q-factors) of the optical whispering-gallery modes excited via a tapered optical-fiber waveguide in single glycerol/water microdroplets standing on a superhydrophobic surface in air.

In **Chapter 7**, we demonstrate long-term size stabilization of surface-supported liquid aerosols of salt-water resulting from competition between resonant absorption of the infrared heating laser by a microdroplet whispering gallery mode and water condensation in the sample chamber.

In **Chapter 8**, we follow up on the previous stabilization experiments and demonstrate controllable tuning of WGMs of self-stabilized surface-supported liquid aerosol using a tunable IR heating laser which has a very narrow linewidth.

Chapter 2

OPTICAL MODES OF A MICROSPHERE-WHISPERING GALLERY MODES (WGMS)

Resonance modes of real resonators with finite losses characterized by finite values of Q-factor are usually referred to as morphology-dependent resonances (MDRs), whispering-gallery modes (WGMs) and quasi-normal modes (QNMs). Optical properties of microspheres are related with the electromagnetic resonant modes of the cavity. Suitable boundary conditions are satisfied by some resonance frequencies. At these frequencies the electric field is confined notably in the cavity. The difference between the modes of Fabry-Perot cavities and the modes of microspheres is the number of dimensions of confinement. The mode confinement direction of microspheres and Fabry-Perot cavities is three and one, respectively [11].

Total internal reflection (TIR) occurs if the angle of incidence (θ_{inc}) of the light with wavelength λ propagating within a sphere of radius a and index of refraction $\mathbf{m}(\omega)$ is equal to or greater than the critical angle (θ_c).

$$\theta_{inc} \geq \theta_c = arcsin(1/\mathbf{m}(\omega)), \tag{2.1}$$

The resonance condition for a sphere with circumference $2\pi a >> \lambda$ and light propagating with $\theta_{inc} \sim 90^o$ is that the circumference of the sphere is nearly equal to the optical path length as demonstrated in Fig. 2.1. The allowed limits of n wavelengths in the dielectric is given by

$$\frac{2\pi a}{\lambda} \leq n \leq \frac{2\pi a}{\lambda/\mathbf{m}(\omega)}. \tag{2.2}$$

Using the size parameter which is dimensionless

$$x = \frac{2\pi a}{\lambda}, \tag{2.3}$$

the resonance condition is
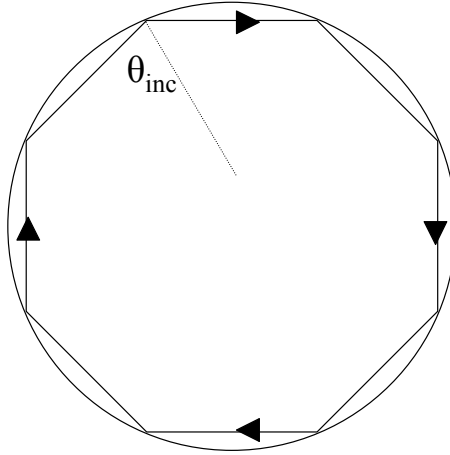
Figure 2.1: The ray at glancing angle is fully reflected. When the optical path is equal to the number of wavelengths, a resonance is formed.

$$x \leq n \leq \mathbf{m}(\omega)x. \tag{2.4}$$

An internal ray completes one roundtrip that corresponds to the phase-matching condition for the $n = \mathbf{m}(\omega)x$ mode and the external wave. If the rays are not confined to the $x - y$ plane(e.g., the equtorial plane), the normal to the orbit is inclined at angle θ with respect to the z-axis and z-component of the angular momentum of the mode is

$$m = ncos(\theta). \tag{2.5}$$

All of the m modes are degenerate (with $2n + 1$ degeneracy) for a perfect sphere. If the sphericity of the cavity is perturbed, the degeneracy is lifted. When there is a distortion like this, the integer values for m are $\pm$n,$\pm$(n-1)...0, where $\pm$ degeneracy rests since the resonance modes are independent of the circulation direction (clockwise or counterclockwise).

The electric field can be expressed in terms of TE modes and TM modes. For TE modes, there is no radial component of the electric field and for TM modes, there is no radial component of the magnetic field. The expressions for TE and TM modes are defined by

$$E_{TE} = z_n(\mathbf{m}(\omega)kr)X_{nm}(\theta, \phi), \tag{2.6}$$

$$E_{TM} = \nabla \times \{z_n(\mathbf{m}(\omega)kr)X_{nm}(\theta,\phi)\} \qquad (2.7)$$

where the wave vector in free space is $k = \omega/c$. The $z_n(\mathbf{m}(\omega)kr)$ is the spherical Bessel function for incident fields and internal fields that characterize the radial dependence of the fields, $z_n(\mathbf{m}(\omega)kr)$ is the spherical Hankel function for external fields. $\mathbf{m}(\omega)$ is the refractive index of the surrounding medium for incident fields, the refractive index of the sphere for the internal fields. $X_{nm}(\theta,\phi)$ is the vector spherical harmonics that characterizes the angular distribution of the electric fields and described by

$$X_{nm}(\theta,\phi) = \frac{-i}{\sqrt{n(n+1)}}r \times \nabla Y_{nm}(\theta,\phi), \qquad (2.8)$$

where $Y_{nm}(\theta,\phi)$ are the spherical harmonics. By matching the tangential components of $\mathbf{E}$ and $\mathbf{H}$ at the boundary, the characteristic equation is obtained. The characteristic equation of a sphere of radius a and index of refraction $\mathbf{m}(\omega) = \mathbf{m}_r(\omega) + i\mathbf{m}_i(\omega)$ in air for TM resonances defined by

$$\frac{\psi_n^{'}(\mathbf{m}(\omega)x)}{\psi_n(\mathbf{m}(\omega)x)} - \mathbf{m}(\omega)\frac{\zeta_n^{'}(x)}{\zeta_n(x)} = 0. \qquad (2.9)$$

The characteristic equation for TE resonances is

$$\mathbf{m}(\omega)\frac{\psi_n^{'}(\mathbf{m}(\omega)x)}{\psi_n(\mathbf{m}(\omega)x)} - \frac{\zeta_n^{'}(x)}{\zeta_n(x)} = 0, \qquad (2.10)$$

where $x = ka = 2\pi a/\lambda$ is the size parameter, ψ_n is the Ricatti-Bessel function, ζ_n is the Ricatti-Henkel function. If there is no absorption loss ($\mathbf{m}_i(\omega)$=0), the solutions to Eq.(2.9) and Eq.(2.10) are the complex resonance size parameters x_α. The resonant frequencies for a fixed radius sphere are designated by the real part of the size parameters. The leakage loss of the mode out of the absorptionless dielectric cavity is related with the imaginary part of the size parameter.

There are several independent equations represented by Eq.(2.9) and Eq.(2.10) for each mode number n. The solutions of these transcendental equations correspond to the resonances, or MDRs. Also, the radial mode number l is obtained from these solutions for each n. For a fixed n and $\mathbf{m}(\omega)$, the first and second solutions are labeled l=1 and l=2,

respectively. The physical interpretation is that the number of intensity maxima of the mode along $r = a/\mathbf{m}(\omega)$ to $r = a$ is l.

The resonance size parameters x_α of a perfect sphere are independent of m. The resonance modes are generally represented by their polarization $TM_{n,l}$ and $TE_{n,l}$. The relation between the real part of x_α and the resonance frequency is

$$\omega_\alpha = cRe(x_\alpha)/a. \tag{2.11}$$

The full width at half maximum(FWHM) of the MDR is twice the imaginary part of x_α. The FWHM of the mode is denoted Δx_α or $\Delta \omega_\alpha$. The quality factor (Q) of the resonance is represented as

$$Q = \frac{Re(x_\alpha)}{2Im(x_\alpha)} = \frac{\omega_\alpha}{\nabla \omega_\alpha} = \omega_\alpha \tau, \tag{2.12}$$

where τ is the wave lifetime on the resonance. Diffractive leakage losses limit the Q values. The maximum Q can be as high as 10^{100} for a perfect lossless sphere. There are some factors like volume inhomogeneities, surface roughness, shape deformations, nonlinear effects and absorption that limits the maximum Q values to be less than 10^{10} [3]. In chapter 6, we deal with measurement of the quality factor, Q of surface-supported microdroplets.

Chapter 3

SUPERHYDROPHOBIC SURFACE PREPARATION AND MODELLING OF PHOTOTHERMAL TUNING OF THE DROPLET SIZE

3.1   Superhydrophobic Surface Preparation

Superhydrophobic surfaces are extremely water-repellent surfaces. The contact angles of a water droplet exceeds 150° on these surfaces. Superhydrophobic surfaces were prepared by spin coating 50 mg/ml ethanol dispersion of hydrophobically-coated silica nanoparticles (Evonik, Aeroxide   LE1) on cover glasses [4, 12]. The average size of hydrophobic silica nanoparticles was between 7 nm and 20 nm. The superhydrophobic surfaces were transparent to visible light. After spin-coating, the superhydrophobically coated-cover glasses were dried in an oven at 85ºC, for one hour, for evaporation of the remaining ethanol after spin-coating. The measured average contact angle of millimeter-sized salt-water and glycerol/water droplets was larger than 155° on these surfaces. The average contact angle of micrometer-sized microdroplets is expected to be $1-2°$ smaller than that of millimeter sized droplets owing to Gibbs contact line tension [4, 13, 11].

If a droplet is placed on a textured surface with roughness, the roughness structures on the surface can be filled by the droplet liquid as shown in Fig.3.1a. This wetting state is called Wenzel state. Due to surface tension of the droplet liquid, penetration of liquid into surface pores can be prohibited as shown in Fig.3.1b. This wetting state is called as Cassie-Baxter state. Hydrophobic surfaces that have the Cassie-Baxter and Wenzel state are called *slippy* or *sticky* surfaces, respectively [14].
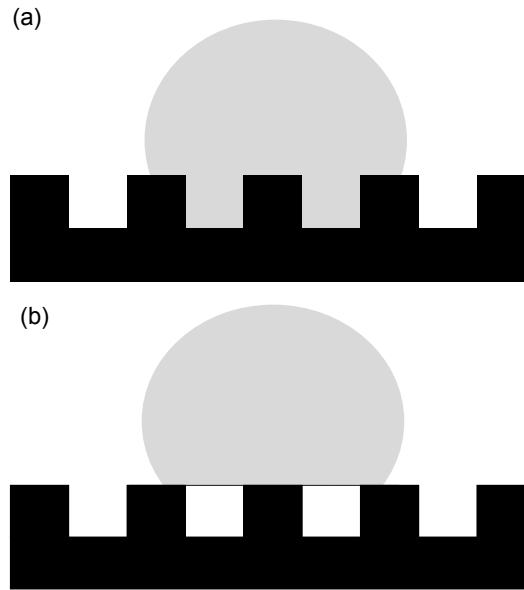
Figure 3.1: Wetting states of textured surfaces.(a)Wenzel state, (b)Cassie-Baxter state

3.2   Modelling of Photothermal Tuning of Liquid Microdroplets and $\tilde{Q}_{abs}$ Calculation

3.2.1   Introduction

We defined a lumped equation model for the evaporation and growth of water-glycerol and
NaCl-water microdroplets standing on a superhydrophobic surface due to local heating by a
focused infrared laser. The generalized Lorenz-Mie theory [15, 16, 17] was used to calculate
the absorption of the focused laser beam by the microdroplet.

3.2.2   Rate Equation Model for a Water-glycerol Microdroplet Standing on a Superhy-
drophobic Surface

The mass and heat transfer between the microdroplet and the chamber is simulated by
using a lumped system model according to Ray et al. [18, 19]. This model is based on the
uniform temperature and composition distributions within the microdroplet for all times.
This assumption holds if the heat and mass transfer within the microdroplet is much faster
than the heat and mass transfer across a microdroplet interface. In addition, we assume
that heat and mass transfer occur solely due to molecular diffusion in a quasi-stationary

state. Using these assumptions, the number of moles of component A (water) N_A and B (glycerol) N_B in the microdroplet of radius a is given by

$$\frac{dN_A}{dt} = -4\pi a f_{PB} D_A \frac{P_A^0(T_\infty)}{RT_\infty} (\gamma_A x_A \phi_A - S_A), \tag{3.1}$$

$$\frac{dN_B}{dt} = -4\pi a f_{PB} D_B \frac{P_B^0(T_\infty)}{RT_\infty} (\gamma_B x_B \phi_B - S_B), \tag{3.2}$$

where

$$\phi_A = \left(\frac{T_\infty}{T_d}\right) \frac{P_A^0(T_d)}{P_A^0(T_\infty)}; \quad \phi_B = \left(\frac{T_\infty}{T_d}\right) \frac{P_B^0(T_d)}{P_B^0(T_\infty)}. \tag{3.3}$$

In Eqs.(3.1-3.3), the subscripts A and B denote properties of the components A and B, respectively, $D_{A,B}$ is the molecular diffusivity in the gas mixture, $\gamma_{A,B}$ is the activity coefficient, $x_{A,B}$ is the mole fraction, $S_{A,B}$ is the relative humidity in the chamber, R is the universal gas constant, $P_{A,B}^0(T)$ is the vapor pressure at temperature T, and T_d and T_∞ are the temperatures at the microdroplet interface and in the chamber far from the microdroplet, respectively. The effects of the substrate on the mass transfer is included to the equations and defined as the correction factor f_{PB} defined by Picknett and Bexon [20, 21] equation:

$$f_{PB}(\theta) = \frac{1}{2} \begin{cases} 0.6366\theta + 0.09591\theta^2 - 0.06144\theta^3 & 0^o \leq \theta < 10^o \\ 0.000008957 + 0.6333\theta + 0.116\theta^2 - 0.08878\theta^3 + 0.01033\theta^4 & 10^o \leq \theta < 180^o, \end{cases} \tag{3.4}$$

where θ is the contact angle. The contact angle for millimeter-size droplets standing on a superhydrophobic surface is obtained experimentally about 160°. It is not very different for micrometer-size droplets standing on a superhydrophobic surface. The temperature change of the microdroplet with time can be written as:

$$\frac{dT_d}{dt} = \frac{\Delta H_{vap,A}}{NC_{PL}} \frac{dN_A}{dt} + \frac{\Delta H_{vap,B}}{NC_{PL}} \frac{dN_B}{dt} - \frac{3k_{\text{eff}} V_m}{a^2 C_{PL}} (T_d - T_\infty) + \frac{\tilde{Q}_{abs} P_{inc}}{NC_{PL}}, \tag{3.5}$$

where V_m is the molar specific volume, N is the total number of moles, C_{PL} is the molar heat capacity of the glycerol-water microdroplet, $\Delta H_{vap,A,B}$ is the enthalpy of evaporation and k_{eff} is the effective heat conductivity. We defined k_{eff} as the area average of heat conductivities of air(k_a) and substrate (k_s). k_{eff} can be written as:

$$k_{\text{eff}} = f_a k_a A_a + (1 - f_a) k_s, \tag{3.6}$$

where f_a can be defined as:

$$f_a = A_a/A_d. \tag{3.7}$$

In Eqn. (3.7) A_a is the surface area of the microdroplet that is in contact with the air
and A_d is the total surface area of the microdroplet. $\tilde{Q}_{abs}$ in Eq. (3.5) defines the ratio of the
total power absorbed by the microdroplet to the total power of the incident beam (P_{inc}).
Calculation of $\tilde{Q}_{abs}$ for a focused incident laser beam is described in Section 3.2.4. The

Table 3.1: Constants

Constant	Value	Unit
V_A	$18.0153 \cdot 10^{-6}$	m^3/mol
V_B	$73.03 \cdot 10^{-6}$	m^3/mol
R	8.314472	$J/(mol \cdot K)$
$\Delta H_{vap,A}$	40714.578	J/mol
$\Delta H_{vap,B}$	61000	J/mol
C_{PA}	75.327	$J/(mol \cdot K)$
C_{PB}	221.193	$J/(mol \cdot K)$
D_A	$24.2 \cdot 10^{-6}$	m^2/sec
D_B	$8.7710 \cdot 10^{-6}$	m^2/sec
k_a	0.02620	$W/(m \cdot K)$
k_s	1.14	$W/(m \cdot K)$
n_A	$1.33 + 1202.32 \cdot 10^{-9}i$	
n_B	$1.47 + 1811.95 \cdot 10^{-9}i$	

activity coefficients of water and glycerol are calculated by van Laar equation and Gibbs-
Duhem Equation , respectively. The van Laar equation for water activity coefficient(γ_A):

$$\ln \gamma_A = \frac{c_1}{\left(1 + \frac{c_1}{c_2}\frac{x_A}{1-x_A}\right)^2}, \tag{3.8}$$

.

The parameters $c_1 = -0.3049$ and $c_2 = -0.8551$ in Eq. (3.8) are determined by making the best fit to the experimental data by Tu and Ray [19].

The Gibbs-Duhem equation for the glycerol acvitivity coefficient(γ_B):

$$\ln \gamma_B = \frac{c_2}{c_1} \left(2\sqrt{c_1 \ln \gamma_A} + \ln \gamma_A + c_1 \right). \tag{3.9}$$
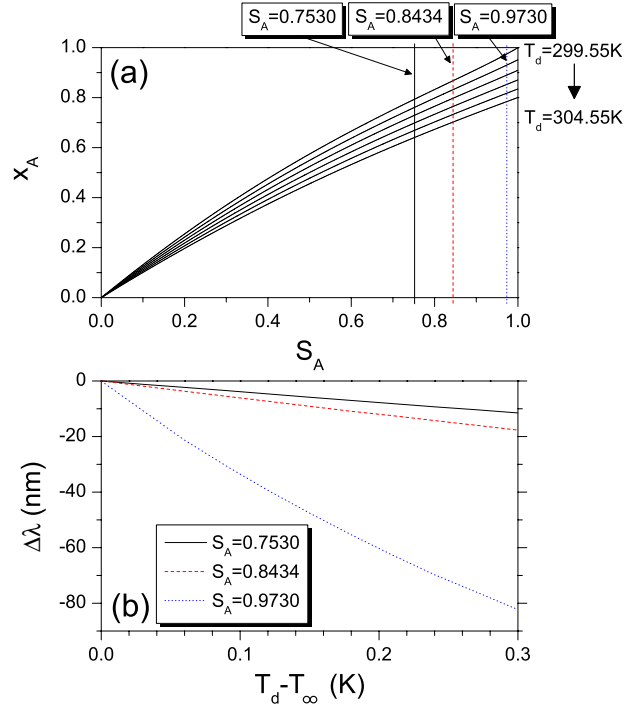
Figure 3.2: Steady state analysis assuming that glycerol is ideally nonvolatile. (a) Steady mole fraction of water as a function of relative humidity of water for various values of microdroplet temperature (T_d) assuming the temperature of the chamber (T_∞) to be 299.55 K. Vertical lines indicate the relative humidities of water used in the experiments. (b) The spectral drift in the WGMs located at around 590 nm as a function of $T_d - T_\infty$.

Fig. 3.2a shows the steady state situation between the microdroplet and the environment assuming that $T_\infty = 299.55\ K$ and glycerol is ideally nonvolatile. At the steady state S_A equals to $\gamma_A x_A \phi_A$ and T_d is larger than T_∞. When T_d increases, x_A decreases. If we look at the fixed value of S_A we can see that the change of x_A with temperature is more prominent at high relative water humidities. We also observed that when $S_A > 0.9$ the large size change of the droplet is possible with the small variation in droplet temperature. At high relative water humidities, there is very little amount of glycerol in the microdroplet. Due

to higher volatility of water than glycerol large tuning of microdroplet is obtained at high relative water humidities. For the center wavelength 590 nm, the spectral change of the WGMs as a function of $T_d - T_\infty$ is showed in Fig. 3.2b for three different S_A values. The linear equation between the spectral position of the WGMs and the normalized equtorial radius is defined as [22, 23]:

$$\frac{\Delta a}{a} = \frac{\Delta \lambda}{\lambda}, \tag{3.10}$$

.

3.2.3 *Rate Equation Model for a NaCl-water Microdroplet Standing on a Superhydrophobic Surface*

In the case of NaCl - water droplets, water is the only volatile component in the droplet. The change in the number of moles of component A (water) in the microdroplet of radius a and the change in the temperature of the microdroplet due to the time is the same as Eq.3.1 and Eq.3.5, respectively. By using the polynomial best fit given in ref.[24], the water activity coefficient (γ_A) and the solution density (d) are calculated as

$$\gamma_A = 1.0 + \sum C_i x_{WP}^i \tag{3.11}$$

$$d = 0.9971 + \sum A_i x_{WP}^i \tag{3.12}$$

where $C_1 = -6.366 \times 10^{-3}$, $C_2 = 8.624 \times 10^{-5}$, $C_3 = -1.158 \times 10^{-5}$, $C_4 = 1.518 \times 10^{-7}$, $A_1 = 7.41 \times 10^{-3}$, $A_2 = -3.741 \times 10^{-5}$, $A_3 = 2.252 \times 10^{-6}$, $A_4 = -2.06 \times 10^{-8}$, and x_{WP} represents the solute weight percent. The real and imaginary part of the refractive index were determined considering the concetration of salt amount in the microdroplet and the wavelength of the laser [24, 25, 26, 27].

3.2.4 *Generalized Lorentz-Mie Theory*

Generalized Lorenz-Mie Theory is always needed when dealing with light scattering of focused beams, as opposed to the regular Lorenz-Mie theory which describes scattering of plane waves [28]. There are three waves due to particle/laser interaction. These are the scattered wave outside the sphere, the internal wave inside the sphere, and the incident wave. The main goal is to obtain matching solutions to these electromagnetic waves by using the boundary conditions at the surface of the sphere. The electromagnetic field components are

$$E_r = \frac{\partial^2 \left(r^e\Pi\right)}{\partial r^2} + k^2 r^e\Pi, \tag{3.13}$$

$$E_\theta = \frac{1}{r}\frac{\partial^2 \left(r^e\Pi\right)}{\partial\theta\partial r^2} + \frac{k^{''}}{r sin\theta}\frac{\partial \left(r^m\Pi\right)}{\partial\Phi}, \tag{3.14}$$

$$E_\phi = \frac{1}{r sin\theta}\frac{\partial^2 \left(r^e\Pi\right)}{\partial\phi\partial r^2} - \frac{k^{''}}{r}\frac{\partial \left(r^m\Pi\right)}{\partial\theta}, \tag{3.15}$$

$$H_r = \frac{\partial^2 \left(r^m\Pi\right)}{\partial r^2} + k^2 r^m\Pi, \tag{3.16}$$

$$H_\theta = -\frac{k^{'}}{r sin\theta}\frac{\partial \left(r^e\Pi\right)}{\partial\phi} + \frac{1}{r}\frac{\partial^2 \left(r^m\Pi\right)}{\partial r\partial\phi}, \tag{3.17}$$

$$H_\phi = -\frac{k^{'}}{r}\frac{\partial \left(r^e\Pi\right)}{\partial\theta} + \frac{1}{r sin\theta}\frac{\partial^2 \left(r^m\Pi\right)}{\partial r\partial\phi}, \tag{3.18}$$

where $^e\Pi$ is the scalar potential associated with the electric field, $^m\Pi$ is the scalar potental associated with the magnetic field, $k^{'} = ik_0\bar{\epsilon}$, $k^{''} = ik_0$ and $k = k_0\sqrt{\bar{\epsilon}}$. The complex dielectric constant is $\bar{\epsilon} = \epsilon + i4\pi\sigma/\omega$. σ is the electrical conductivity. $^e\Pi$ and $^m\Pi$ satisfy the Helmhotz equation

$$\nabla^2\Pi + k^2\Pi = 0. \tag{3.19}$$

The most general seperation of variables solution of the Helmholtz equation (Eq.3.19) is

$$r\Pi = \sum_{l=0}^{\infty}\sum_{m=-l}^{l}\left[\tilde{A}_{lm}\psi_l\left(kr\right) + \tilde{B}_{lm}\chi_l\left(kr\right)\right]Y_{lm}(\theta,\phi), \tag{3.20}$$

where $\tilde{A}_{lm}$, $\tilde{B}_{lm}$ are the arbitrary constants, ψ_l and χ_l are the Ricatti-Bessel functions and $Y_{lm}(\theta,\phi)$ is the spherical harmonic function.

The wave scalar potentials of the electric and magnetic fields for the incident field (superscript i), the scattered field (superscript s) and the internal field (superscript w) are

$$r^e\Pi_{(i)} = \sum_{l=0}^{\infty}\sum_{m=-l}^{l}A_{lm}\psi_l\left(k_{ext}r\right)Y_{lm}(\theta,\phi), \tag{3.21}$$

$$r^m \Pi_{(i)} = \sum_{l=0}^{\infty} \sum_{m=-l}^{l} B_{lm} \psi_l (k_{ext} r) Y_{lm}(\theta, \phi), \tag{3.22}$$

$$r^e \Pi_{(s)} = \sum_{l=0}^{\infty} \sum_{m=-l}^{l} a_{lm} \xi_l^{(1)} (k_{ext} r) Y_{lm}(\theta, \phi), \tag{3.23}$$

$$r^m \Pi_{(s)} = \sum_{l=0}^{\infty} \sum_{m=-l}^{l} b_{lm} \xi_l^{(1)} (k_{ext} r) Y_{lm}(\theta, \phi), \tag{3.24}$$

$$r^e \Pi_{(w)} = \sum_{l=0}^{\infty} \sum_{m=-l}^{l} c_{lm} \xi_l^{(1)} (k_{int} r) Y_{lm}(\theta, \phi), \tag{3.25}$$

$$r^m \Pi_{(w)} = \sum_{l=0}^{\infty} \sum_{m=-l}^{l} d_{lm} \xi_l^{(1)} (k_{int} r) Y_{lm}(\theta, \phi), \tag{3.26}$$

where $\xi_l^{(1)} = \psi_l - i\chi_l$. χ_l have been ignored for the incident and the internal field because these functions are unbounded at the origin.

The incident, scattered and internal electromagnetic fields are provided by substituting Eqs. 3.21-3.26 into Eqs. 3.13-3.18. The coefficients that describe individual fields can be found using appropriate boundary conditions. The tangential components of the electric and magnetic fields are continuous across the sphere surface.

The coefficients that describe the scattered field are defined in terms of the incident field as;

$$a_{lm} = \frac{\psi_l' (k_{int} a) \psi (k_{ext} a) - \bar{n} \psi_l (k_{int} a) \psi_l' (k_{ext} a)}{\bar{n} \psi_l (k_{int} a) \xi_l^{(1)'} (k_{ext} a) - \psi_l' (k_{int} a) \xi_l^{(1)} (k_{ext} a)} A_{lm}, \tag{3.27}$$

$$b_{lm} = \frac{\bar{n} \psi_l' (k_{int} a) \psi (k_{ext} a) - \psi_l (k_{int} a) \psi_l' (k_{ext} a)}{\psi_l (k_{int} a) \xi_l^{(1)'} (k_{ext} a) - \bar{n} \psi_l' (k_{int} a) \xi_l^{(1)} (k_{ext} a)} B_{lm}. \tag{3.28}$$

The coefficients that describe the internal field are defined in terms of the incident field as;

$$c_{lm} = \frac{\xi_l^{(1)'} (k_{ext} a) \psi (k_{ext} a) - \xi_l^{(1)} (k_{ext} a) \psi_l' (k_{ext} a)}{\bar{n}^2 \psi_l (k_{int} a) \xi_l^{(1)'} (k_{ext} a) - \bar{n} \psi_l' (k_{int} a) \xi_l^{(1)} (k_{ext} a)} A_{lm}, \tag{3.29}$$

$$d_{lm} = \frac{\xi_l^{(1)'} (k_{ext} a) \psi (k_{ext} a) - \xi_l^{(1)} (k_{ext} a) \psi_l' (k_{ext} a)}{\psi_l (k_{int} a) \xi_l^{(1)'} (k_{ext} a) - \bar{n} \psi_l' (k_{int} a) \xi_l^{(1)} (k_{ext} a)} B_{lm}. \tag{3.30}$$

The coefficients that describe the incident field are defined as;

$$A_{lm} = \frac{a^2}{l(l+1)\psi_l\left(k_{ext}a\right)} \int_0^{2\pi} \int_0^{\pi} sin\theta E_r^i\left(a, \theta, \phi\right) \times Y_{lm}^* d\theta d\phi, \qquad (3.31)$$

$$B_{lm} = \frac{a^2}{l(l+1)\psi_l\left(k_{ext}a\right)} \int_0^{2\pi} \int_0^{\pi} sin\theta H_r^i\left(a, \theta, \phi\right) \times Y_{lm}^* d\theta d\phi, \qquad (3.32)$$

where $\bar{n}$ is the complex relative index of refraction and defined as

$$\bar{n} = \left(\bar{\epsilon}_{int}/\epsilon_{ext}\right)^{1/2}. \qquad (3.33)$$

The time-averaged power absorbed by the sphere can be defined by integrating the radial component of the external field Poynting vector over a surface enclosing the sphere. For the large integration radius, it is defined as [29, 30]

$$W_{abs} = -\frac{c}{8\pi}k_0^2\epsilon_{ext} \sum_{l=-1}^{\infty} \sum_{m=-l}^{l} l\left(l+1\right) \left[|a_{lm}|^2 + |b_{lm}|^2 + Re\left(A_{lm}a_{lm}^* + B_{lm}b_{lm}^*\right)\right]. \qquad (3.34)$$

The ratio of the total power absorbed by the sphere to the total power of the incident beam is defined as modified absorbtion efficiency ($\tilde{Q}_{abs}$). Using the value of the total power of the incident beam is $(c/16)E_0^2 w_0^2$ where E_0^2 is the electric field amplitude at the beam focus, the modified absorption efficiency is defined as

$$\tilde{Q}_{abs} = -\frac{2\alpha^2}{\pi \tilde{w}_0^2 \alpha^4 E_0^2} \sum_{l=1}^{\infty} \sum_{m=-l}^{l} l\left(l+1\right) \left[|a_{lm}|^2 + |b_{lm}|^2 + Re\left(A_{lm}a_{lm}^* + B_{lm}b_{lm}^*\right)\right]. \qquad (3.35)$$
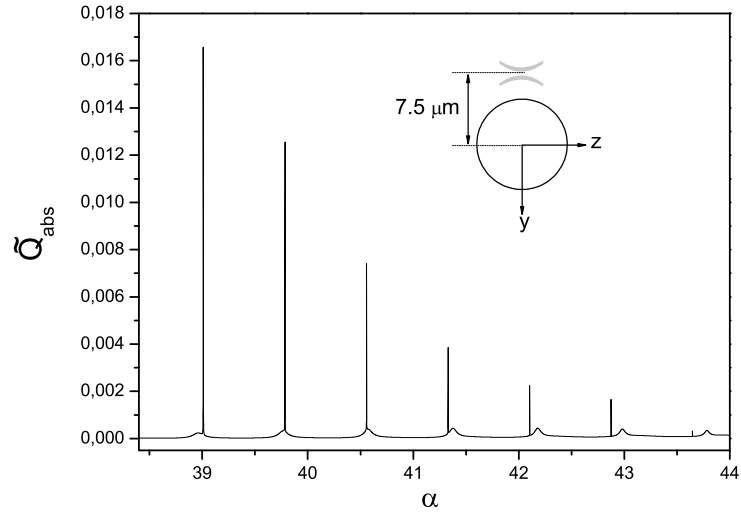
Figure 3.3: The modified absorption efficiency ($\tilde{Q}_{abs}$) as a function of the size parameter (α). Calculations are made for a sphere suspended in air by using the localized approximation to the beam-shape coefficients in generalized Lorenz-Mie theory. The laser propagating in z and polarized in x directions is focused near the vicinity of the rim of the sphere at y=7.5 μm.

The calculation of ($\tilde{Q}_{abs}$) as a function of the size parameter $\alpha = 2\pi a/\lambda$, for a 7 μm spherical particle suspended in air is shown in Fig.3.3. In this calculation, wavelength and focal waist were taken as $\lambda = 1064$ nm and $\omega_0 = 1000$ nm. Only first order TE modes are excited due to off-axis excitation [16].

3.2.5   Hysteresis Behavior in the Droplet Size Tuning

Fig. 3.4a shows the result of the $\tilde{Q}_{abs}$ calculation as a function of the size parameter, $\alpha = 2\pi a/\lambda$, where a and λ are the radius of the microdroplet and wavelength, respectively. This calculation was performed using the localized approximation to the beam-shape coefficients in generalized Lorenz-Mie theory [31, 28] with an improved algorithm [16]. The refractive index of the microdroplet was assumed to be $n = 1.33 + 1202.32 \cdot 10^{-9}i$ [26]. A Gaussian beam with a focal waist of w_0=1000 nm that is propagating in z and linearly polarized in x directions was considered to be focused 5.5 μm away from the microdroplet's center along the y direction, as shown in the inset in Fig. 3.4a. Angular momentum number and radial
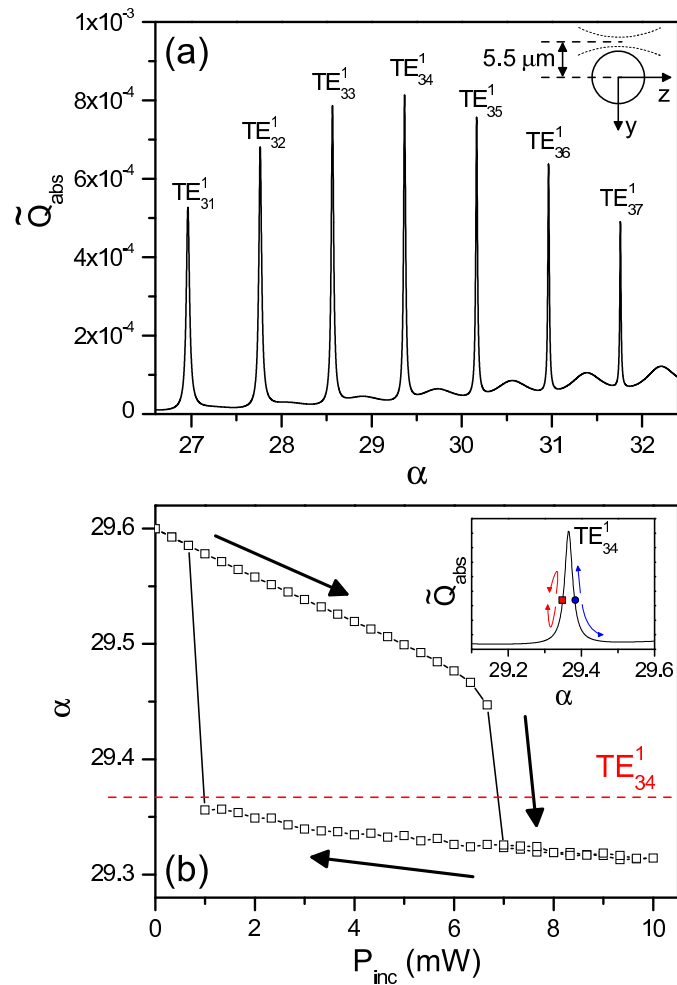
Figure 3.4: (a) The modified absorption efficiency ($\tilde{Q}_{abs}$) as a function of the size parameter
(α). Calculations are made for a sphere suspended in air by using the localized approxima-
tion to the beam-shape coefficients in generalized Lorenz-Mie theory. The laser propagating
in z and polarized in x directions is focused near the vicinity of the rim of the sphere at
y=5.5 μm, exciting first order TE modes. (b) The computational hysteresis curve as func-
tion of the incident laser power. The dashed line shows the peak position of the TE_{34}^1 WGM
absorption. Inset shows the sketch of the self-stabilization mechanism.

mode order of the high quality WGMs are shown in Fig. 3.4a. Only TE WGMs are excited

due to the selected focus point, and polarization [3].

In Fig. 3.4b we show the change in α as P_{inc} is first gradually increased from 0 to 10 mW,

and then decreased back to 0 mW, calculated using the $\tilde{Q}_{abs}$ function shown in Fig. 3.4a.

In this calculation, the initial size parameter ($\alpha = 29.6$ corresponding to $a = 5.0125$ μm) is

intentionally selected to be slightly larger than the position of the TE_{34}^1 WGM absorption that is peaked at $\alpha = 29.365$. Hysteretic behavior is clearly observed in the calculated photothermal tuning cycle. As P_{inc} is increased, α first decreases at an almost constant rate until around P_{inc}=6.7 mW where α decreases sharply due to the absorption resonance. For P_{inc} values between 7 and 10 mW, α once more decreases at an almost constant rate. As P_{inc} is decreased from 10 mW, α increases at an almost constant rate until P_{inc}=1 mW where α suddenly increases. The lower plateau observed between P_{inc}=1 and 7 mW in the photothermal tuning cycle gives the self-stable operation points that correspond to the TE_{34}^1 WGM absorption that was selected. Self-stable operation points are situated on the increasing half (region with positive slope) of a specific peak in the $\tilde{Q}_{abs}$ function, as shown with the red box in the inset of Fig. 3.4b. Around such a self-stable operation point, an increase or decrease in size are followed by an increase or decrease in $\tilde{Q}_{abs}$, respectively. These tend to bring the system back to the initial operating point, ensuring the self-stable operation. In contrast, self-stable operation is not observed around points located on the decreasing half (region with negative slope) of a peak in the $\tilde{Q}_{abs}$ function, as shown with the blue circle in the inset of Fig. 3.4b. Around such a point, an increase or decrease in size are followed by a decrease or increase in $\tilde{Q}_{abs}$, respectively. Hence the system quickly goes away from such an operation point [11].

Chapter 4

PROBING OF WGMS BY FREE SPACE LIGHT COUPLING-APPLICATIONS IN SURFACE ANALYSIS

4.1 Probing Microscopic Wetting Properties of Superhydrophobic Surfaces by Vibrated Micrometer-Sized Droplets

4.1.1 Introduction[1]

Superhydrophobic (SH) surfaces are gaining increasing attention because of their potential applications in liquid nanotechnology, e.g. in MEMS and optofluidic systems [32, 33, 34, 4]. The wetting properties of a SH surface can be described by the apparent contact angle θ that characterizes the overall energy balance of the liquid–solid–vapor interaction [35]. Several techniques exist for measuring the value of θ over the macroscopic length scales of SH surfaces ($> 100\,\mu$m) [36, 37, 38]; however, these techniques do not allow probing of the variations of θ resulting from the micron–scale heterogeneity of the surface chemistry and/or topography. Alternative methods based on AFM [13] or electron microscopy imaging [39] are restricted by the accessible range of θ ($\theta < 90^{\text{o}}$) or the ambient atmosphere humidity, respectively.

In this part, we introduce a novel method for the microscopic contact angle measurement that is based on the analysis of mechanical resonances of individual micrometer–sized liquid droplets supported by a vibrated SH surface. We exploit the spectroscopy of the optical whispering gallery modes (WGMs) excited by laser light in the fluorescently stained droplets to simultaneously identify the droplet mechanical resonances and sizes. The droplets act as optical microcavities [4] and their fluorescence spectra feature WGMs whose spectral widths depend on the droplet vibration amplitude. By monitoring the WGM width as a function of the substrate oscillation frequency for droplets of different sizes, we identify their mechanical resonances at the frequencies of the maximal WGM broadening. Droplet size is

then determined by mode–matching of the WGMs using the Lorenz–Mie scattering theory. For a given droplet, the precise value of the contact angle θ is subsequently obtained from independent measurements of the droplet mechanical resonance frequency and size using the previously developed theory for the axisymmetric sessile droplet oscillations [40, 41]. Using our technique we measure microscopic contact angles on two substrates with different levels of superhydrophobicity and find a good correlation with the average contact angles of millimetric droplets observed on the same surfaces.

We note that contact angle determination using droplet vibrational frequency measurement has been demonstrated previously only with millimeter–sized droplets [42]. However, measurement of contact angles larger than 110° was not reported in [42]. Moreover, the experiments did not employ WGMs to simultaneously determine the mechanical resonance and size of a droplet with high precision.
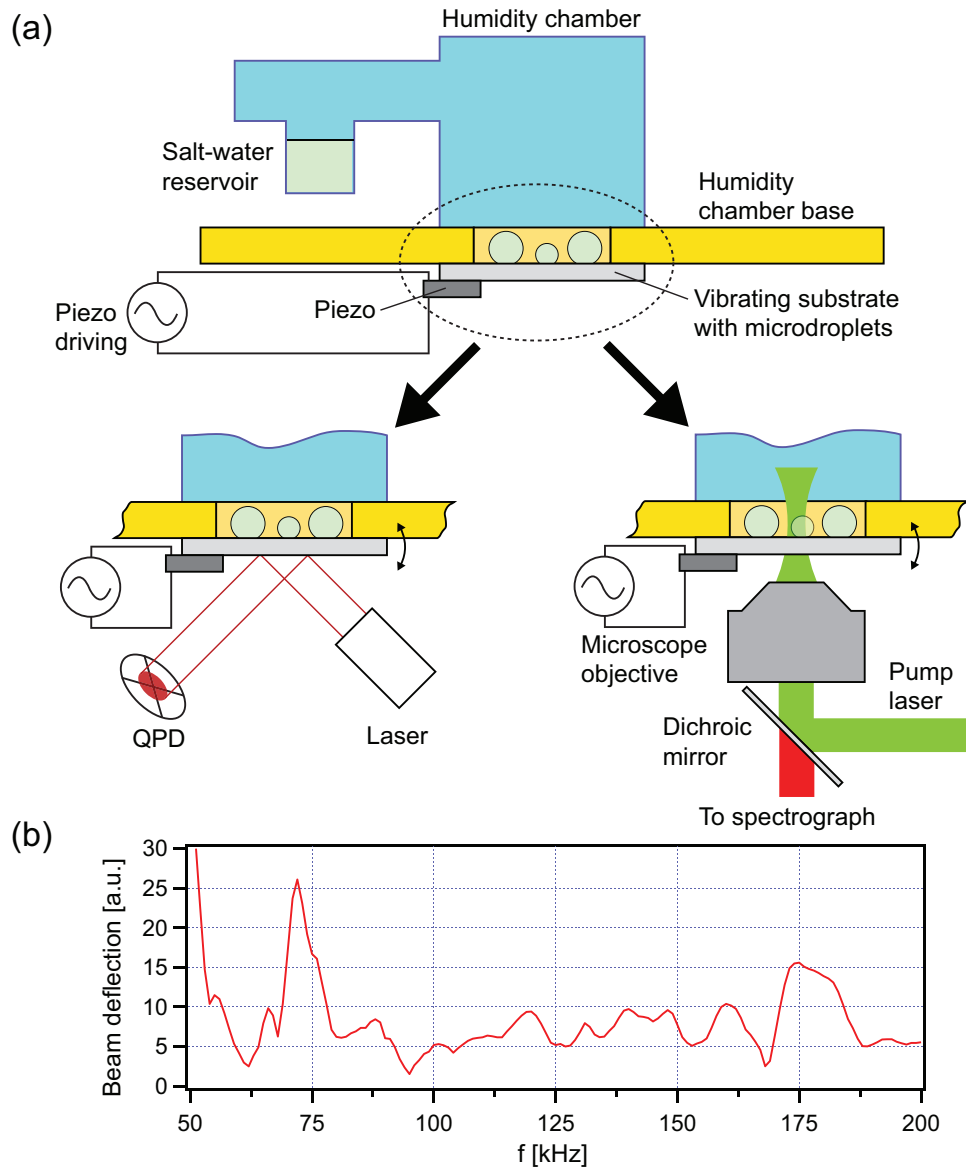
Figure 4.1: Experimental setup used for the microdroplet contact angle measurement. (a) Illustration of the controlled humidity sample chamber. [left] The frequency response of the mounted substrate to the harmonic PZT driving is characterized using an auxiliary collimated laser beam and a quadrant photodiode (QPD). [right] Actual detection of the microdroplet resonant frequency is carried out using inverted microscope configuration featuring a spectrograph. (b) Laser beam deflection from the substrate as a function of the driving frequency f. The beam deflection is directly proportional to the substrate vibration amplitude.

4.1.2 Experimental Section

The model SH surfaces used in the experiments described here are prepared by spin–coating suspensions of hydrophobically–coated silica nanoparticles (Aeroxide LE1, average particle size: 14 ± 3 nm; Evonik) onto a cleaned cover glass as described previously [43]. The super-hydrophobicity level of the surface is adjusted by suspending the nanoparticles in different solvents (ethanol or chloroform at concentration of 50 mg/ml) before spin–coating. Rhodamine B doped NaCl–water microdroplets (2.5 M NaCl, $100\,\mu$M Rhodamine B) generated by an ultrasonic nebulizer are sprayed onto the SH surface in ambient atmospheric conditions. A piezoelectric transducer (PZT) that excites the droplet oscillations perpendicular to the plane of the cover glass is glued to the opposite surface of the cover glass using Entellan microscopy mounting medium (Merck Chemicals) so that it does not obstruct the observation of the droplets (see Fig.4.1a). Subsequently, the studied substrate bearing the microdroplets is attached to the bottom part of a home–made sample chamber whose relative water humidity is fixed at 84% with a saturated water solution of KCl. Optical spectroscopic experiments are performed in the inverted microscope geometry (see Fig.4.1a, right). An air microscope objective (NA=0.8, 60x; Nikon) is used for tight focusing of the pump CW green laser ($\lambda = 532$ nm, 4.5 mW max. power) onto the rim of a selected droplet. The fluorescence excited in the droplet is then collected by the same microscope objective and directed to a 500 mm monochromator with 1200 gr/mm grating (spectral resolution: 0.07 nm, SpectraPro; Acton Research) that disperses the light before detection by a spectroscopic CCD camera (Pixis 100F; Princeton Instruments). A high voltage amplifier (WMA-300; Falco Systems) connected to the output of a function generator (33220A; Agilent) is used to drive the PZT with a $\sim$300 V peak-to-peak sinusoidal signal at varying frequencies.

For each prepared sample chamber, the vibrational response of the substrate was characterized by measuring the deflection of a laser beam reflected from the vibrating substrate with a quadrant photodiode (see Fig.4.1a, left). Fig.4.1b shows a typical vibrational response from a substrate used in the experiments. Considerable substrate vibration amplitudes are observed between 50-200 kHz. This is the critical frequency range that contains the lowest–order axisymmetric mechanical resonances of the micrometer–sized droplets studied here [40]. Some variations were observed in the vibrational responses of different substrates

used in the experiments, mainly due to variations in the elastic properties and the mounting of the cover glasses. However, the peaks featured in the substrate vibrational responses were always broad due to the amorphous nature of the cover glasses. Hence, approximately constant oscillatory forcing was ensured in the vicinity of the mechanical resonant frequencies of individual studied droplets.

4.1.3   Results and Discussion

Contact angle measurements relied on sweeping the piezo–driving frequency while recording the fluorescence spectra from individual microdroplets. Droplet mechanical resonances were then revealed after an analysis of the WGM widths as a function of the driving frequency. It should be noted that for each of the studied droplets, only a single mechanical resonant frequency was observed within the frequency range 50-200 kHz.
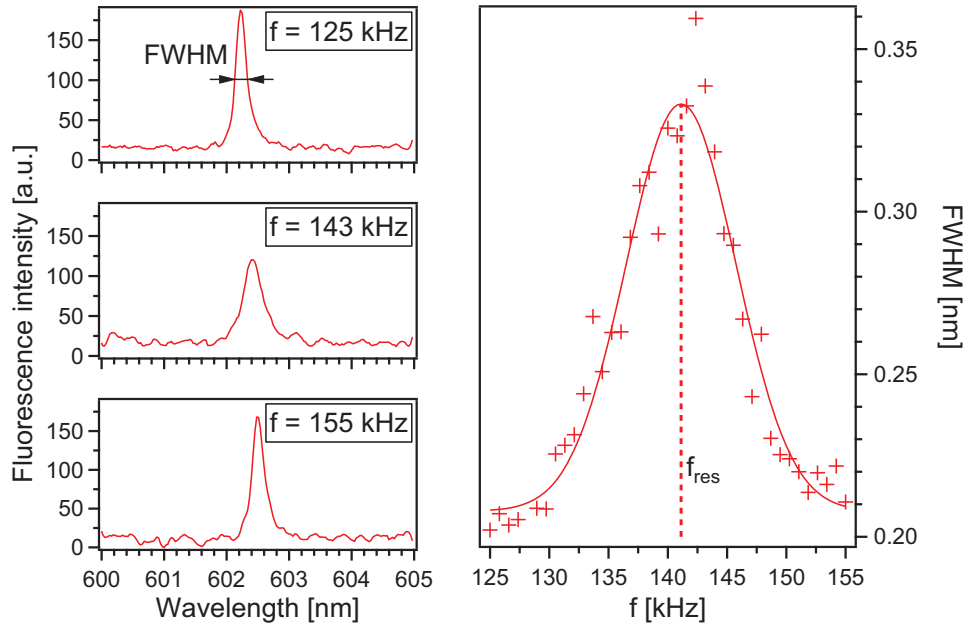
Figure 4.2: Response of surface–supported microdroplets to the harmonic oscillatory driving. (left) Fluorescence spectra of an oscillating droplet with spherical radius $R = 5.0$ μm at three different driving frequencies f. The WGM centered at 602.3 nm is characterized by its full width at half maximum (FWHM). (right) FWHM as a function of f. The crosses indicate experimental data points, the continuous line is the Gaussian fit that gives the droplet resonant frequency $f_{res}^{exp} = 141.1$ kHz.

Fig.4.2 illustrates how the full width at half maximum (FWHM) of a WGM from an

exemplary NaCl–water microdroplet changes with the mechanical driving frequency f. The WGM in the fluorescence spectrum of the vibrated droplet displays a significant broadening when the mechanical resonant frequency is approached. This is caused by the intensified droplet shape oscillations at the resonance which lower the optical Q-factor of the droplet cavity [3]. The actual resonance at $f_{\text{res}}^{\text{exp}} = 141.1$ kHz is clearly revealed by a Gaussian fit of the measured data. Vibration of sessile droplets has been recently extensively studied and various models predicting the droplet resonant frequencies have been proposed [44, 45, 46]. For our case of vertically–driven micrometric spherical droplets whose shape is completely determined by surface tension with a negligible influence of gravity, the most appropriate model of oscillations is the one developed by Strani and Sabetta [40]. Within this model, the lowest axisymmetric oscillation frequency $f_{\text{res}}^{\text{th}}$ is given by:

$$f_{\text{res}}^{\text{th}} = (2\pi)^{-1} \left[\frac{\gamma}{\rho R^3 \lambda_1(\theta)} \right]^{1/2} \tag{4.1}$$

where γ, ρ, and R correspond to the surface tension of the liquid, the density of the liquid, and the droplet spherical radius, respectively. $\lambda_1(\theta)$ is the eigenvalue associated with the lowest–frequency mode (mode number 1) that strongly depends on the contact angle θ. Consequently, for a droplet of known material properties and size, the value of θ can be determined using Eq. 4.1 and the measured resonant frequency $f_{\text{res}}^{\text{exp}}$.

Besides being extremely sensitive to small droplet vibrations, WGMs also allow an independent measurement of the droplet spherical radius R. Fluorescence spectra recorded in our experiments cover a spectral range of 39.1 nm containing at least 3 WGMs belonging to the same mode family identified by polarization and mode order. Within the framework of the Lorenz–Mie scattering theory, the value of R can be obtained from direct mode–matching of these WGMs [3, 47, 48]. In this approach, R is determined by finding a set of droplet size parameters $a_i = (2\pi R)/\lambda_i$ which provide the best match between the measured WGM spectral positions and those calculated for the droplet refractive index $n = 1.3677$. Here, λ_i denote the experimentally determined vacuum wavelengths of the WGMs contained within the given droplet fluorescence spectrum. For the case shown in Fig.4.2, mode–matching gives $R = 5.0$ μm. We estimate the uncertainty in R values (mainly given by the uncertainty in the droplet refractive index) to be less than 100 nm. Such precision cannot be obtained from the optical microscopy observation of the droplet as the identification of the droplet equatorial plane where its spherical radius can be measured is to large extent

arbitrary.
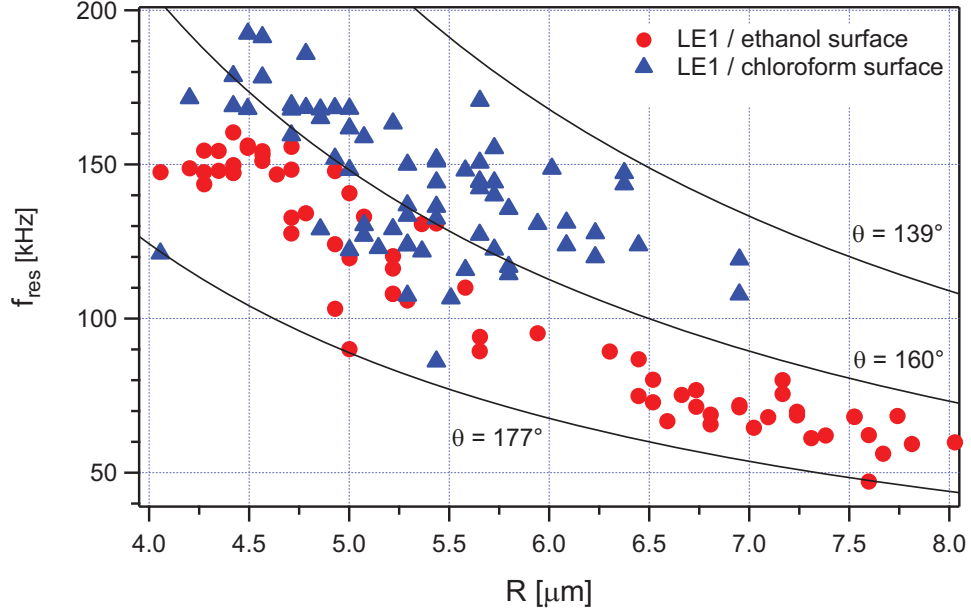
Figure 4.3: Dependence of the lowest–mode resonant frequency f_{res} on the droplet size. The circles and triangles indicate experimental data points obtained for droplets supported by the LE1/ethanol and LE1/chloroform surfaces, respectively. The lines show the resonant frequency values calculated from Eq. 4.1 for the contact angles of 177° (lower frequency limit), 160° (frequency mid-range), and 139° (upper frequency limit). Other calculation parameters for the NaCl-water microdroplet: surface tension $\gamma = 74.62$ mN/m, density $\rho = 1144.7$ kg/m^3, and refractive index $n = 1.3677$.

Fig.4.3 shows the distributions of f_{res}^{exp} for microdroplets of various spherical radii R supported by two different SH surfaces (LE1/ethanol coating - red circles, LE1/chloroform coating - blue triangles). For both of the studied surfaces, the experimental data was recorded on several substrates prepared using the procedure described above and no significant substrate–to–substrate variations were observed. Also shown in the plot are the resonant frequencies f_{res}^{th} calculated from Eq. 4.1 for several contact angles with the contact-angle–dependent eigenvalues $\lambda_1(\theta)$ determined using previously described procedure [41]. Comparison of the measured and calculated values of the lowest–mode resonant frequencies indicates that the droplet resonant behavior is indeed well described by the formalism developed by Strani and Sabeta in [40]. The spread in the measured resonant frequencies for droplets of given R can be attributed mainly to the spot–to–spot variations of the local chemistry and/or topography of the studied SH surface that are also observed in light

microscopy, AFM, and SEM images of the surfaces [49] and that lead to the contact angle hysteresis [50]. Additional uncertainty of $f_{\mathrm{res}}^{\mathrm{exp}}$ then stems from the non–uniform response of the sample chamber to the mechanical oscillatory driving (see Fig.4.1).
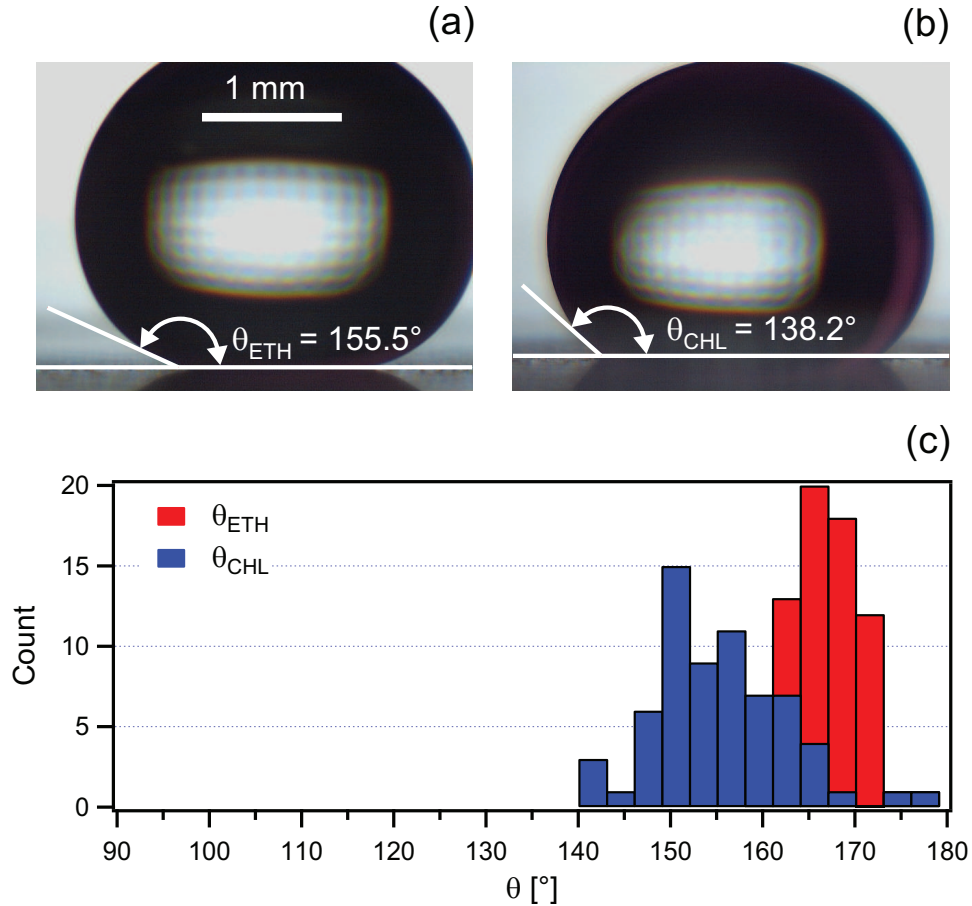
Figure 4.4: Contact angle measurements on superhydrophobic (SH) surfaces. Direct imaging of an NaCl-water droplet on (a) LE1/ethanol-coated and (b) LE1/chloroform-coated SH surfaces. (c) Histogram of the microscopic contact angles θ for the LE1/ethanol–coated (70 measurements, $\tilde{\theta}_{\mathrm{ETH}} = 166.7°$) and LE1/chloroform–coated (68 measurements, $\tilde{\theta}_{\mathrm{CHL}} = 153.8°$) SH surfaces. The contact angles are calculated from the data presented in Fig.4.3 using Eq. 4.1.

From the experimental data presented in Fig.4.3, it is evident that the mechanical resonant frequencies for the droplets of a given R differ for the LE1/ethanol–coated and LE1/chloroform–coated SH surfaces. Since the droplet material properties are identical for both cases, this deviation can only be attributed to contact angles differences between the two surfaces (see Eq. 4.1). Such dependence of the contact angle on the solvent used

for the SH layer deposition has been previously reported [51].

Fig.4.4 summarizes the results of both macroscopic and microscopic (vibration–based) contact angle measurements on the two studied SH surfaces. Macroscopic values of θ were obtained using direct imaging of droplets of stationary size generated on the surface with a syringe (see examples in Fig.4.4a,b). This procedure yielded average contact angles $\bar{\theta}_{ETH} = (154.2 \pm 9.1)°$ on the LE1/ethanol–coated SH surface (4 measurements) and $\bar{\theta}_{CHL} = (139.4 \pm 3.6)°$ on the LE1/chloroform–coated SH surface (4 measurements), respectively. From the data of Fig.4.3, microscopic contact angles were calculated through Eq. 4.1. Their distributions are shown in Fig.6.4c with the median values of the contact angles being $\tilde{\theta}_{ETH} = 166.7°$ on the LE1/ethanol–coated SH surface and $\tilde{\theta}_{CHL} = 153.8°$ on the LE1/chloroform–coated SH surface, respectively. These values agree well with the ranges of contact angles determined for microdroplets on a similar SH surface using electrical deformation [52].

As both studied SH surfaces are formed by layers of the same hydrophobic silica nanoparticles, difference in their contact angles cannot be caused by their chemical properties. It is well established that SH surfaces with multiple scales of roughness display higher contact angles than more homogeneous surfaces with the same surface chemistry [53, 54]. Comparison of the SEM images of our model SH surfaces presented in Fig.4.5 reveals a significantly higher variations in roughness of the LE1/ethanol–coated surface relative to the LE1/chloroform–coated surface. Thus, the observed contact angle difference between the two surfaces indeed stems from the surface topography change.

Several groups have applied substrate vibrations in order to induce a wetting transition or contact angle relaxation in a sessile droplet deposited on a surface displaying contact angle hysteresis [55, 56, 57]. In the measurements reported here, no such wetting transitions were observed, as verified by monitoring the WGM positions during a frequency sweep and also after the mechanical driving was turned off. If the droplet went through a wetting transition, its contact angle and, consequently, spherical radius would change abruptly resulting in an abrupt shift of the WGM positions. However, except from a few cases that were excluded from further analysis, no such abrupt changes were observed; small gradual drifts (< 0.5 nm) of the mode spectral positions are due to temperature fluctuations. Thus, we can assume that the microscopic measurements reported here probe the (metastable) wetting
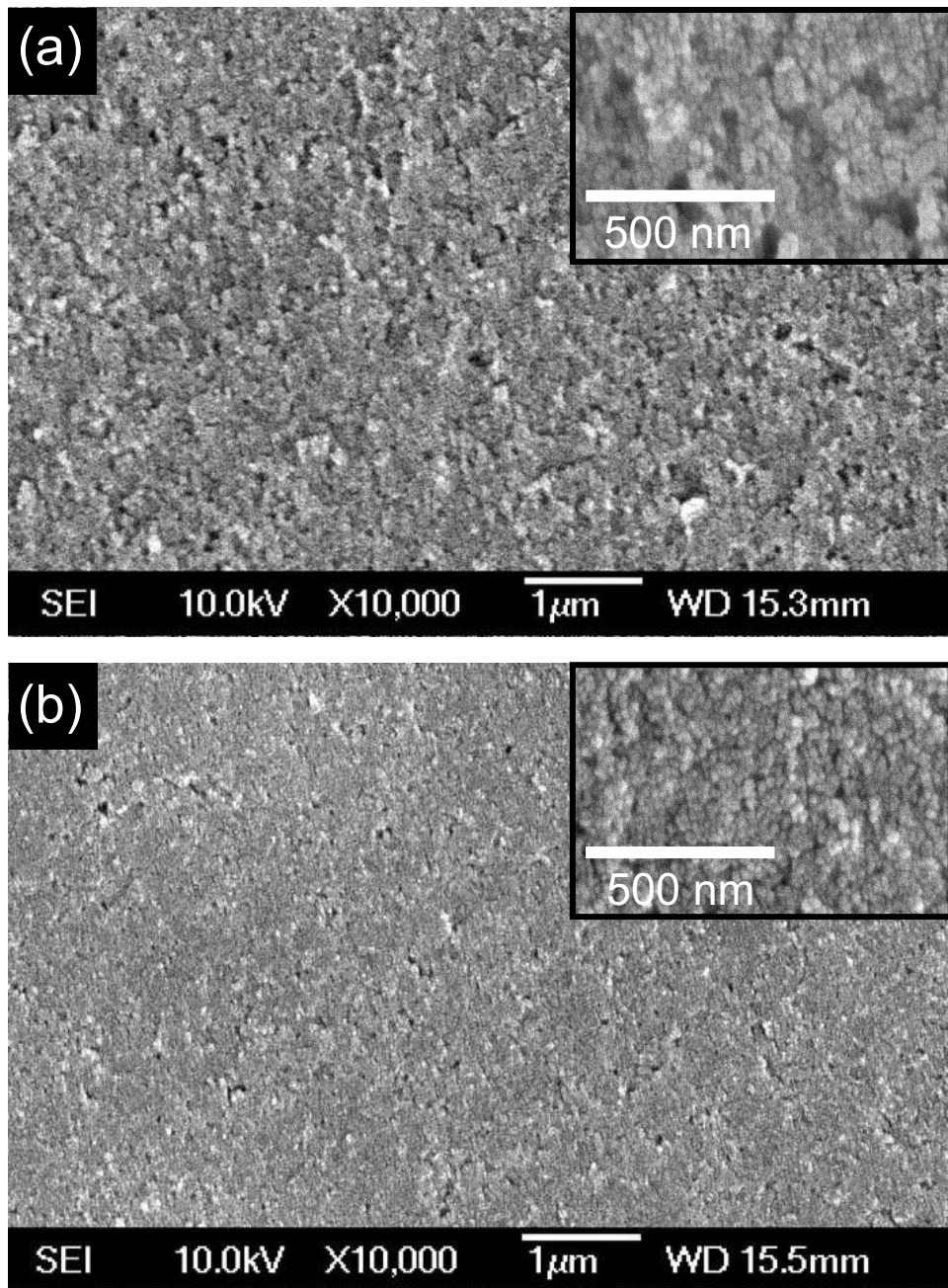
Figure 4.5: SEM images of the studied superhydrophobic surfaces. (a) LE1/ethanol–coated SH surface (b) LE1/chloroform–coated SH surface. Image insets show surface details obtained at higher magnification.

states of the droplets arising at their generation time without changing them. As our SH surfaces display contact angle hysteresis, these initial droplet wetting states may or may not correspond to the global energy minimum (the lowest energy metastable state [55]).

Comparison of the macroscopic and microscopic contact angles reveals a difference in the two values with microscopic measurements being systematically shifted to larger values by about 14°. We attribute this to wetting states that are closer to the global energy minimum [55] in macroscopic measurements where a droplet rolls easily on the surface and can readily move to the most hydrophilic region in the vicinity of the deposition point. Relaxation of the contact angle is further facilitated by mechanical agitation during the syringe retraction in these measurements.

From a practical point of view, it is worth noting that the microscopic contact angle values measured with small droplets are more appropriate for microfluidics applications as they reflect the wetting properties of the surfaces at the relevant length scale. For the typical droplet radius and contact angle values ($R = 5\,\mu$m, $\theta = 165°$) on a SH surface, the contact area between the droplet and the substrate has the radius $r = Rsin(\theta) \approx 1.3\,\mu$m; it is this radius that sets the spatial resolution limit of the contact angle measurement. We note that this resolution limit can be further reduced to $< 1\,\mu$m by employing smaller droplets for the surface probing. In order to accomplish this, a different PZT that allows efficient excitation of droplet vibrations above 200 kHz has to be used.

4.1.4   Conclusions

In conclusion, we have characterized experimentally the microscopic liquid–solid contact angles by analyzing the mechanical resonances of individual micrometric liquid droplets standing on a vibrated SH surface. For two surfaces with different superhydrophobicity levels we have compared the contact angles determined with this method to the values obtained with macroscopic droplet imaging and found a good correlation between the microscopic and macroscopic contact angle measurements. Further investigations are needed to elucidate the relation between the measured microscopic contact angle and global wetting energy minimum for the studied substrate–liquid combination. The presented microscopic contact angle probing has potential applications in the characterization of structured surfaces with complex surface chemistry patterning under a wide range of ambient atmospheric conditions, especially if combined with a precise on–demand positioning of the liquid droplets over the target surface areas.

4.2   Determination of Microdroplet Contact Angles Using Electrically Driven Droplet Oscillations[2]

Optical microcavities based on liquid microdroplets with readily tunable size, shape, and refractive index and exceptionally smooth surfaces can host high-quality optical resonances - the whispering gallery modes (WGMs) [3]. This property makes them well suited for on-chip integrated optofluidic applications, e.g. as reconfigurable optical switches, light sources, or chemical and biological sensors [58]. Several strategies have been developed for incorporating the microdroplets into optofluidic systems [1]. When dealing with droplets of aqueous (polar) liquids, it is advantageous to deposit them on a solid substrate with a superhydrophobic surface [4]. Such a surface deposition stabilizes the position of the droplets without disturbing significantly their shape and, simultaneously, enables interfacing of the droplets with other components of a lab-on-a-chip device, such as integrated waveguides and electronics.

Recently, an application of liquid-based microcavities has been proposed that uses the analysis of sessile droplet vibrations for determining the liquid-solid contact angle θ over micrometer-sized contact areas [59]. In this approach, surface-supported microdroplets were vibrated perpendicularly to the surface using a piezoelectric transducer (PZT) and the values of θ were subsequently calculated from the measured droplet mechanical resonant frequency and spherical radius using a previously developed theory of the sessile droplet axisymmetric oscillations [40]. Vibrational resonances were identified by analyzing the spectral width of the WGMs present in the fluorescence spectra of the dye-doped microdroplets as a function of the droplet vibration frequency. Microscopic contact angle measurements based on the resonant frequency analysis were able to discriminate between surfaces with different superhydrophobicity.

In this part, we extend the vibration-based contact angle measurement technique by introducing electric field driving of the microdroplet mechanical oscillations. To this end, the microdroplets are deposited in a channel formed between two planar gold electrodes on a superhydrophobic surface and subsequently excited by horizontal AC electric field applied between the electrodes (see Fig. 4.6). According to the leaky dielectrics model, this causes

---

[2]This work has been published in "Determination of Microdroplet Contact Angles Using Electrically Driven Droplet Oscillations",Appl. Phys. Lett. 98, 194101 (2011)

periodic droplet deformations that are proportional to the square of the applied electric field [60, 61]. The use of horizontal AC electric field offers an alternative, more practical mechanism for exciting the droplet vibrations. Since the direct mechanical driving of the droplet-bearing substrate with a PZT is eliminated, substrate resonances do not influence the observed droplet mechanical response. Consequently, the droplet excitation is more uniform over the range of the driving frequencies used in the experiments.

The Strani-Sabetta theory [40] describes axisymmetric vibrations of inviscid liquid droplets whose shape is completely determined by surface tension with a negligible influence of gravity. For the lowest-order vibration mode, the resonant frequency f_1 is given by $f_1 = (2\pi)^{-1} \left[\frac{\gamma}{\rho R^3 \lambda_1(\theta)} \right]^{1/2}$. Thus, for a droplet of known surface tension γ, density ρ, spherical radius R, and resonant frequency f_1, the contact angle θ can be determined from the lowest-mode eigenvalue $\lambda_1(\theta)$ calculated from the above equation [40, 41, 62]. Strictly speaking, driving the droplet oscillations with the horizontal AC electric field does not induce purely axisymmetric vibration modes as the driving force is perpendicular to the axis of symmetry of a sessile droplet. However, we show here that in the limit of small non-axisymmetric deformations and large contact angles, droplet resonant frequencies determined sequentially using PZT (axisymmetric) and horizontal field (non-axisymmetric) driving are very close. Hence, the use of the Strani-Sabetta theory is justified for the contact angle measurements based on electrically driven droplet oscillations.

We note that electrically driven oscillations in the horizontal electric field geometry have been previously reported for characterizing the mechanical frequency response of millimeter-sized water droplets [63]. In that work, however, large droplet deformations were observed that led to significant changes of the droplet contact angle during its oscillation. Also, droplets having relatively small contact angles ($\theta < 124°$) were studied and no quantitative comparison to a theoretical model was made.

Our experimental setup is depicted in Fig. 4.6. Planar electrodes are prepared by subsequent evaporation of Ti (thickness: 0.5 μm) and Au (thickness: 1 μm) on coverglass substrates in a 10^{-5} Pa vacuum chamber. A copper mask is used during evaporation in order to obtain 70-90 μm-wide insulating channels between the electrodes. Superhydrophobic surfaces are prepared by spin coating a suspension of hydrophobic silica nanoparticles (50 mg Aeroxide LE1 in 1 mL ethanol, average particle size: 14 ± 3 nm; Evonik) on cover-
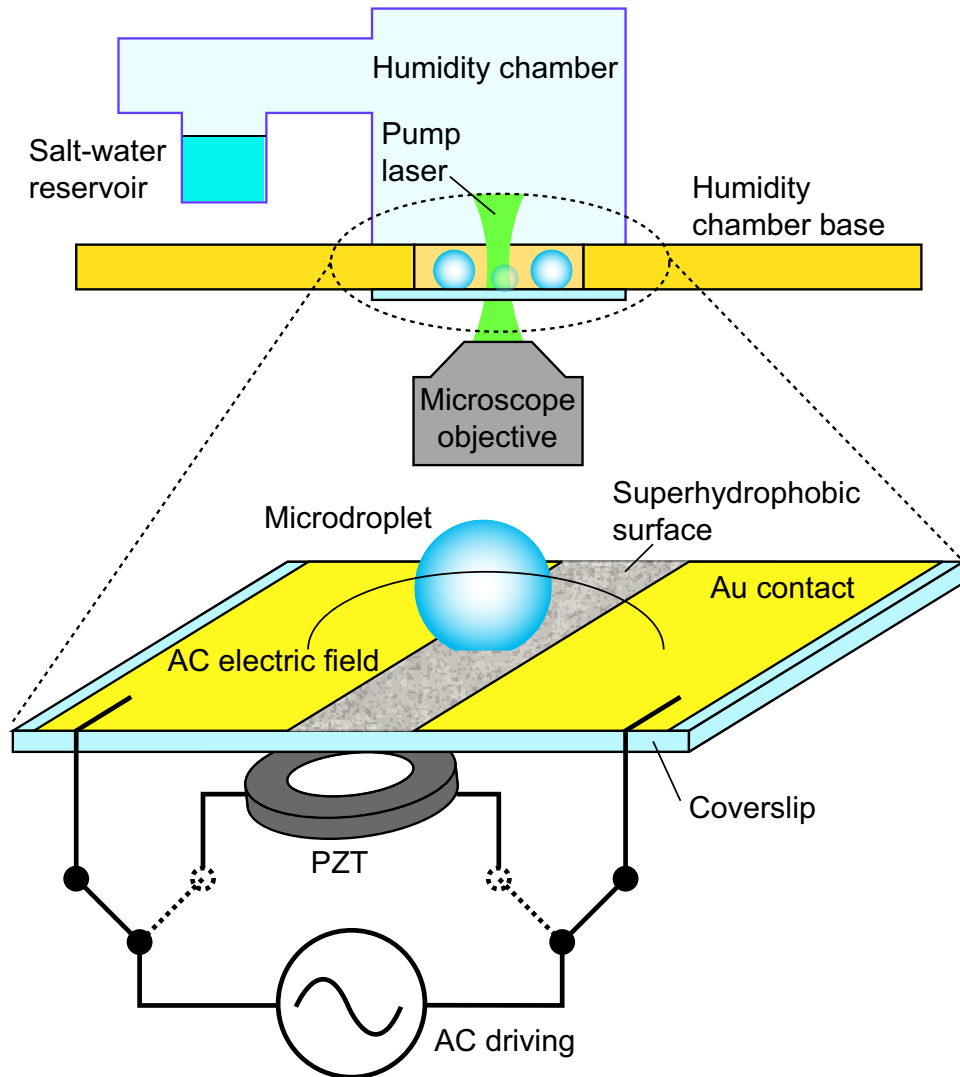
Figure 4.6: Experimental setup for contact angle measurements using vibrated microdroplets. Droplets are sequentially driven by a horizontal AC electric field and a PZT.

glasses with electrodes [43]. Rhodamine B-doped NaCl-water microdroplets (2.5 M NaCl, 100 μM Rhodamine B) are then sprayed into the channel between the Au electrodes by an ultrasonic nebulizer in ambient atmospheric conditions. A PZT is glued beneath the coverglasses for direct mechanical excitation of the droplet vibrations. Prepared coverglasses are then attached to the base of a sealed humidity chamber whose relative humidity is fixed at 84% with a saturated water solution of KCl. Experiments are performed approximately one hour after sealing the chamber, once the droplets reach their equilibrium sizes.

WGMs of dye-doped droplets are observed using fluorescence spectroscopy [43, 59]. Indi-

vidual droplets are excited in the vicinity of their rim by a 532 nm CW green laser (maximal power 4.5 mW) that is focused by an air objective (NA=0.8, 60x). The fluorescence emission is collected using the same objective and dispersed by a 500 mm monochromator with a 1200 gr/mm grating (spectral resolution: 0.07 nm). A cooled CCD camera is used for recording fluorescence spectra with an exposure time of 750 ms. High voltage oscillatory driving of the electrodes or the PZT is achieved by a high voltage amplifier attached to the output of a function generator, providing ∼300 V peak-to-peak sinusoidal voltage at varying frequencies. During the experiments, mechanical resonances are characterized using both the PZT and the horizontal electric field driving for each microdroplet. In both cases, consecutive fluorescence spectra are recorded as a function of the excitation frequency and the mechanical resonances are revealed by the analysis of the frequency dependence of the WGM spectral widths. The droplet spherical radii are determined by the WGM mode-matching as described previously [59].

Fig. 4.7a shows exemplary fluorescence spectra recorded from a droplet with a spherical radius of 5.4 μm upon horizontal electric field driving with frequencies of 105 kHz, 119 kHz, and 135 kHz. We note that, for the case of the horizontal electric field driving, excitation frequencies reported in this work are equal to twice the frequency of the AC voltage applied between the electrodes because of the quadratic dependence of the droplet deformation on the field strength. The WGM centered at ∼600.2 nm shows maximal broadening at ∼119 kHz due to the mechanical resonance of the droplet. The mechanical resonant frequency is determined by analyzing the full width at half maximum (FWHM) of the WGM as a function of the excitation frequency (Fig. 4.7b, top). A Gaussian fit to the experimental data reveals a mechanical resonant frequency of 119.3 kHz for this microdroplet. For comparison, Fig. 4.7b, bottom, shows the frequency dependence of the FWHM of the same WGM obtained from the same microdroplet upon PZT driving. In this case, the Gaussian fit gives a mechanical resonant frequency of 119.5 kHz which is very close to the value obtained by the electrical excitation. In general, near resonance, the mechanical frequency response of a droplet obtained with the electric field driving is broader than that obtained with the PZT driving. We attribute this mainly to the fact that, for the case of the PZT driving, the observed frequency response of the droplet is narrowed by multiplication of its actual frequency response by the spectrally non-uniform frequency response of the
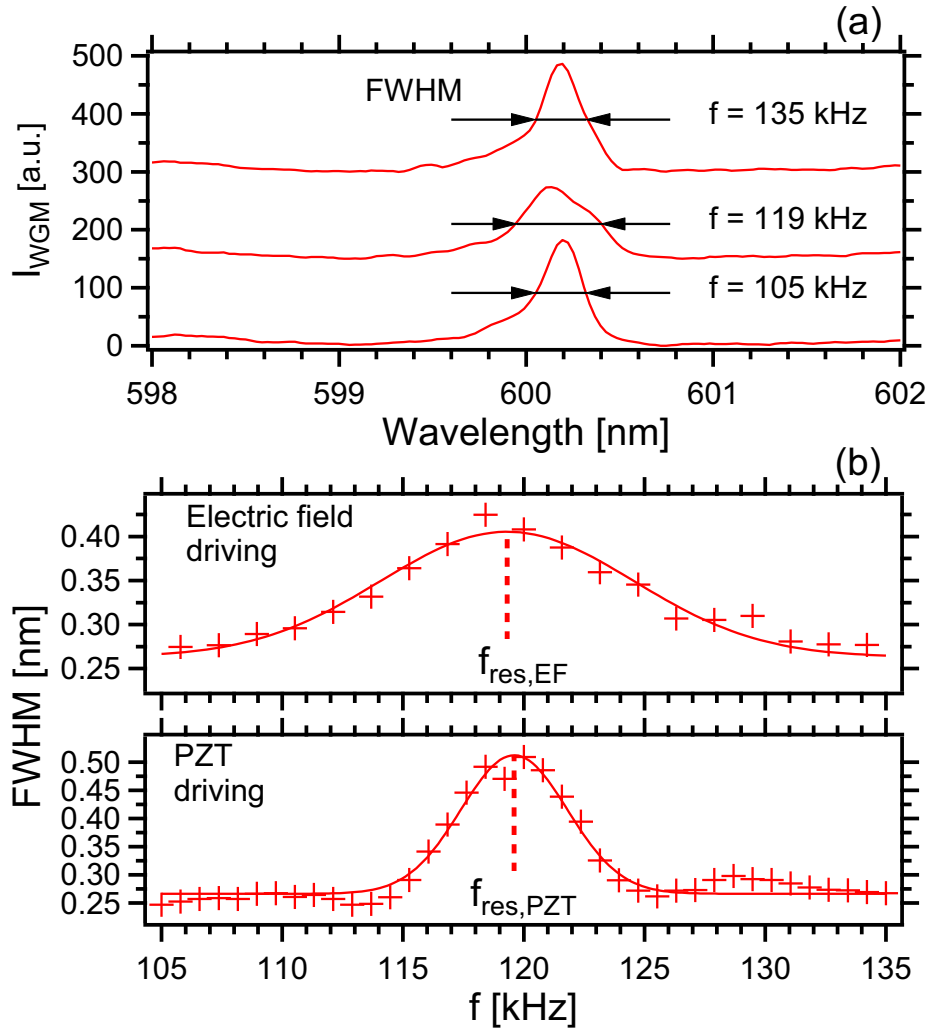
Figure 4.7: (a) Fluorescence spectra of a droplet with a spherical radius $R = 5.4$ μm excited by a horizontal AC electric field at three different frequencies f. (b) FWHM of the WGM in (a) as a function of f for horizontal electric field (top plot) and PZT (bottom plot) driving for the same droplet. Crosses indicate experimental data points, continuous lines are the Gaussian fits that reveal droplet resonant frequencies $f_{\text{res,EF}}^{\text{exp}} = 119.3$ kHz and $f_{\text{res,PZT}}^{\text{exp}} = 119.5$ kHz, respectively.

superhydrophobic substrate [59].

Fig. 4.8(a) shows the resonant frequencies of droplets with spherical radii varying between 3.5-6 μm obtained from sequential measurements performed using horizontal electric field (red circles) and PZT (blue triangles) driving. The contact angles calculated from the Strani-Sabetta theory for the experimental data presented in Fig. 4.8(a) are shown in Fig. 4.8(b). Only small relative differences between the horizontal electric field and PZT
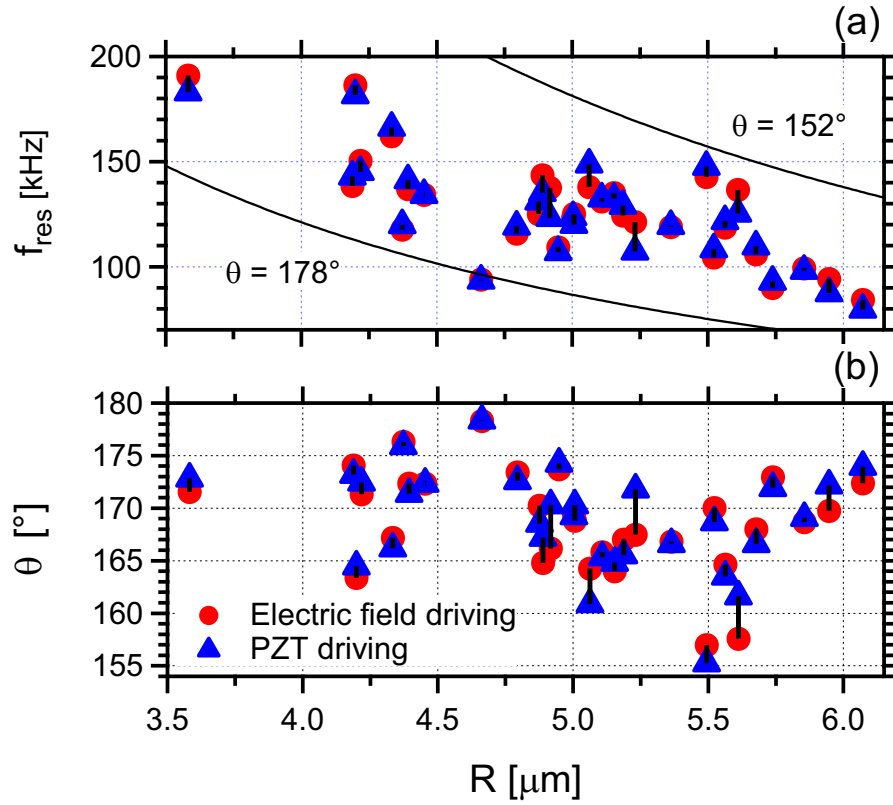
Figure 4.8: (a) Dependence of the measured mechanical resonant frequencies f_{res} on the droplet spherical radius R. Circles and triangles indicate data points obtained with horizontal electric field and vertical PZT driving, respectively. Lines show the values of f_{res} calculated using the Strani-Sabetta theory for contact angles of 178° (lower frequency limit) and 152° (upper frequency limit). Other calculation parameters for the NaCl-water microdroplets: surface tension $\gamma = 80.1$ mN/m, density $\rho = 1144.7$ kg/m^3, and refractive index $n = 1.3677$. (b) Contact angles calculated for the resonant frequencies in (a) using the Strani-Sabetta theory.

driving are observed in the measured resonant frequencies (max $\pm10\%$) and contact angles (max $\pm2\%$), with no systematic bias. These small differences that are mainly attributed to the substrate's non-uniform mechanical response during the PZT driving, indicate that in both cases, approximately axisymmetric vibrations predicted by the Strani-Sabetta theory are excited. This assumption is further justified by the relatively small ($< 0.2\%$) non-axisymmetric deformations of the droplets due the electric field intensities used for the droplet driving [52]. Hence, the Strani-Sabetta theory is well suited for the contact angle measurements reported in this letter.

In conclusion, we have studied the lowest-order vibrational resonances of microdroplets on superhydrophobic surfaces for droplet oscillations driven both horizontally with an AC electric field and vertically with a PZT. Our experimental results show that for small deformations, the horizontal electric field driving excites nearly axisymmetric droplet vibrational modes for contact angles $\theta > 150°$. Consequently, the theoretical model of the axisymmetric droplet oscillations can be used to calculate the droplet-surface contact angle. In comparison to the PZT driving, horizontal electric field driving offers a more practical mechanism for the contact angle measurement, enabling direct oscillatory excitation of the droplets, without being influenced by the substrate's mechanical response. Electric field driving can be applied to droplets immersed in another fluid instead of air. In such a situation, the amplitude of the driving will change depending on the material properties of both fluids (relative permittivity, conductivity, viscosity, and interfacial tension) [60], but the general contact angle measurement procedure is not altered. Electric field driving can also provide an easy access to the selective excitation of chosen microdroplets using suitably designed electric contact geometries which can be integrated into microfluidic systems in a straightforward way.

4.3 Measuring the Mechanical Resonances of Microdroplets Using a Quadrant Photodiode(QPD)

Detection of mechanical resonances of surface-supported liquid microdroplets from their WGM spectra allows only a limited number of spectral measurements to be carried out before the fluorescent dye inside the droplets photobleaches. In order to address this limitation, we used QPD (quadrant photodiode) instead of optical spectroscopy of WGMs to analyze the mechanical resonances of microdroplets standing on a superhydrophobic surface. The change in amplitude of oscillations on the surface of microdroplet excited by a horizontal AC electric field was measured using the QPD. With this measurement technique, we could observe the mechanical resonance frequency of the microdroplet that had small contact angles because we did not rely on the excitation of WGMs in the droplets which requires an almost complete spherical shape of the droplets. In addition to that, we did not need dye molecule, so we could make long-time observation of each microdroplet. The experimental setup is shown in Fig. 4.9. As before, microdroplets were sprayed on

the superhydrophobic surface between two gold electrodes that were used to drive droplet oscillations with horizontal AC electric field and, subsequently, mechanical oscillations of individual microdroplets were analyzed as a function of driving frequency.
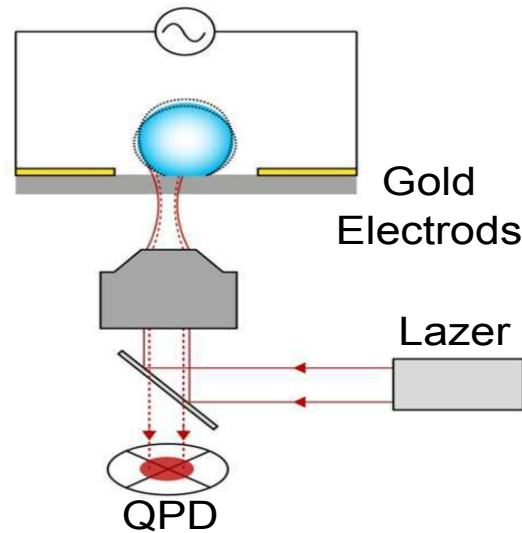
Figure 4.9: Experimental setup for the measuring the mechanical resonance of microdroplet with the use of a quadrant photodiode (QPD).

Fig. 4.10 shows the frequency responses of a microdroplet excited with increasing amplitude of the sinusoidally-varying AC voltage. The peak at 20 kHz is the fundamental mechanical resonance of the microdroplet. The peak at 160 kHz is frequency response of the instruments. If the excitation voltage increases the mechanical resonances that have higher mode orders appears on the frequency response curves. These higher-order modes do not correspond to the frequencies predicted by Strani-Sabbetta model of axisymetric oscillations. This behaviour is attributed to the departing of droplet shape from rotational symmetry with more intense driving.
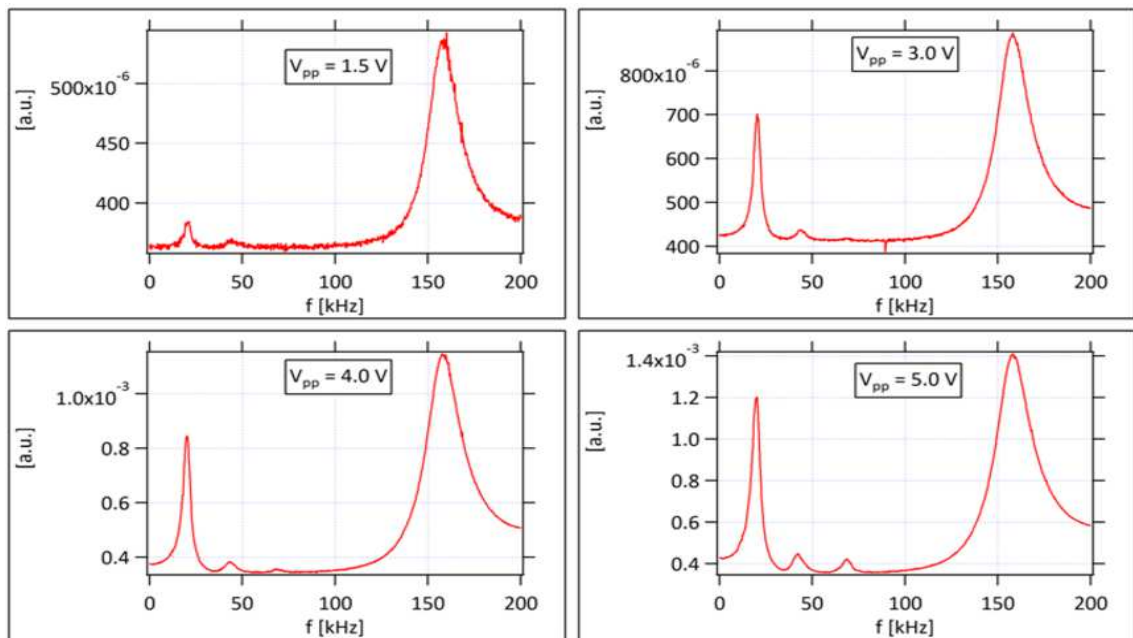
Figure 4.10: Frequency response of a microdroplet at different amplitudes of the sinusoidal excitation voltage.

Chapter 5

TAPERED OPTICAL FIBER FABRICATION AND CUSTOM MICROSCOPE SETUPS

5.1   Introduction

WGM (whispering gallery mode) microcavities are high quality resonators. The most important issue for applications of such resonators is the efficiency of the light coupling from the outside. A schematics view of a spherical WGM resonator is shown in Fig. 5.1. The associated contact line in the figure corresponds to any coupling system.
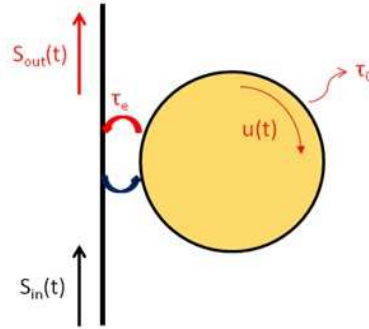
Figure 5.1: Schematic view of WGM resonator coupled to its contact line

We can consider each resonance ω_0 individually because of the high finesse of the resonator. S_{in}, S_{out}, u, τ_e ,and τ_o denote the input signal, the output signal, the amplitude of the resonator mode, the characteristic life time of the resonator mode, and intrinsic photon lifetime, respectively. The light confined in the resonator can escape from the cavity by a radiative or absorptive process with a characteristic duration τ_o and by a back coupling to the output field in the contact line. The intrinsic Q-factor and external Q-factor are defined by $Q_0 = \omega_0\tau_o/2$ and and by $Q_e = \omega_0\tau_e/2$ respectively. The overall Q-factor is determined

from the intrinsic and external Q-factors values by

$$\frac{1}{Q} = \frac{1}{Q_0} + \frac{1}{Q_e} \tag{5.1}$$

and the photon lifetime τ in the cavity is then defined by $Q = \omega_0\tau/2$. Using the coupled mode theory (CMT), the intensity transmission spectrum T reads as

$$T = \frac{(1/\tau_e - 1/\tau_0)^2 + 4\pi^2\delta^2}{1/\tau_e + 1/\tau_0)^2 + 4\pi^2\delta^2} \tag{5.2}$$

where $2\pi\delta = \omega\text{-}\omega_0$ is the frequency detuning function [64, 65]. The relative values of τ_0 and τ_e define the coupling regime of resonator. When $\tau_0 = \tau_e$, the resonator is critically coupled. It means that the losses are equal to the coupling rate. When $\tau_0 > \tau_e$ and $\tau_0 < \tau_e$, the resonator is overcoupled and undercoupled, respectively. Free propagating beams are not efficient for optical coupling due to actually weak radiative transfer to WGMs which can be seen as quasi-bound state of light trapped inside a dielectric material. Several methods have been developed to solve this problem. The oldest method used to couple light in WGM resonators is prism coupling [66, 67, 68]. This method can be improved using an angle polished fiber instead of prism [69]. Alternatively, tapered fibers have been used usually to obtain critical coupling [70, 10]. In our work, we tried to observe the critical coupling of a high-Q liquid microdroplet whispering gallery mode resonator coupled to a fiber taper. In this chapter, the design and implementation of experimental setup for tapering of optical fibers is presented. We also introduce custom-made microscope that allows observation of light coupling from tapered optical fibers to surface-supported liquid microdroplets. As a first test of our light-coupling system based on tapered optical fibers, we study WGMs of cylindrical resonator formed by a piece of bare regular optical fiber.

5.2 Fabrication of Tapered Optical Fibers

Computer-controlled experimental setup for manufacturing tapered optical fibers for applications in optical WGM spectroscopy of microdroplets was realized(see Fig. 5.2). This setup uses a hydrogen-burning torch with precisely controlled hydrogen flow rate to melt locally the fiber while simultaneously pulling it with two motorized linear stages moving in opposite directions. Pilot experiments with fiber tapering were carried out in order to optimize the conditions for reproducible manufacturing of tapers with low transmission loss
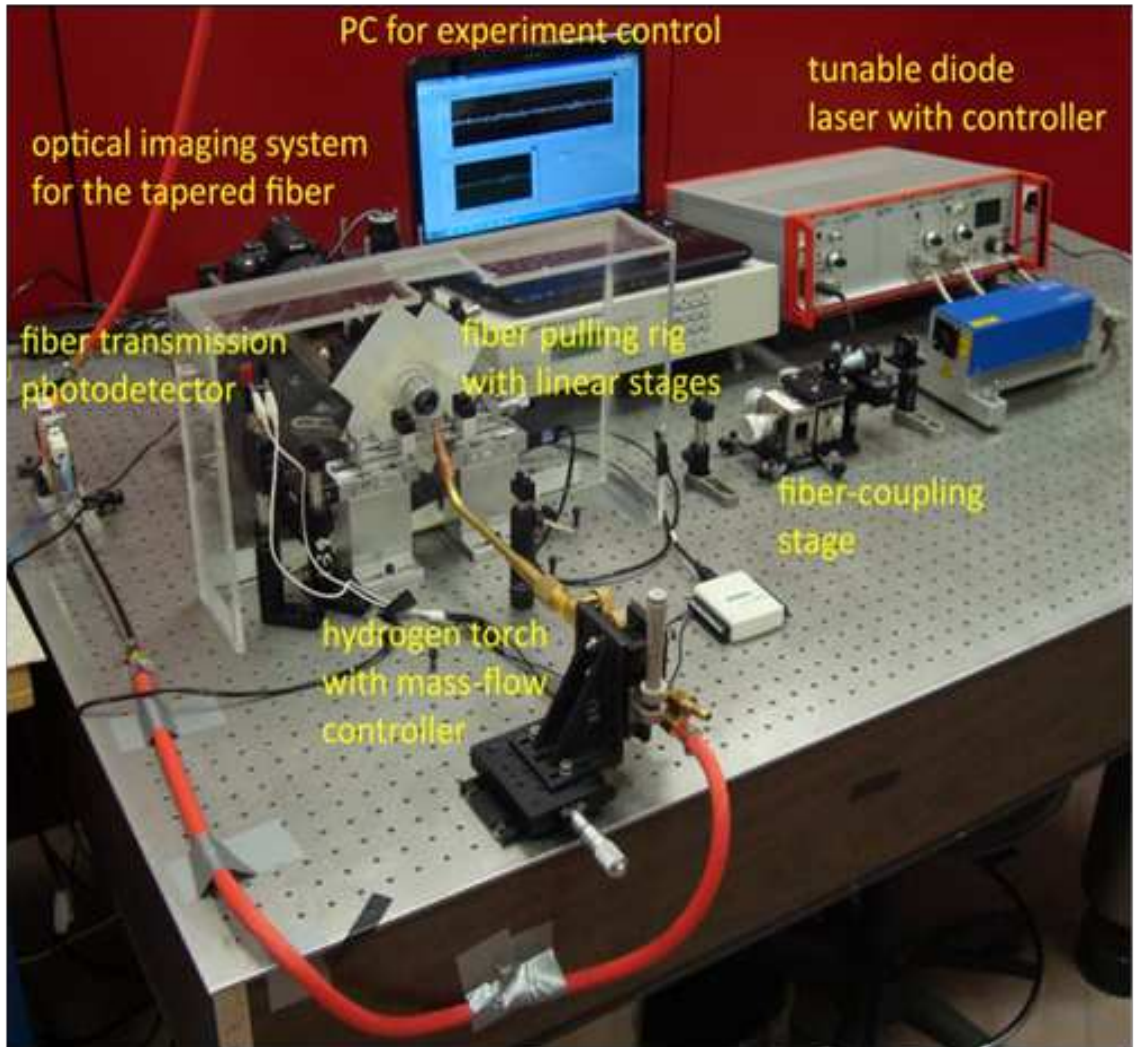
Figure 5.2: Experimental setup for manufacturing tapered optical fibers.

and dimensions appropriate for efficient coupling of light into microdroplets. The produced fiber tapers were characterized by direct optical imaging of the fiber and measurement of the taper transmission during the fiber pulling and by SEM imaging of final tapered fibers (see Fig. 5.3).
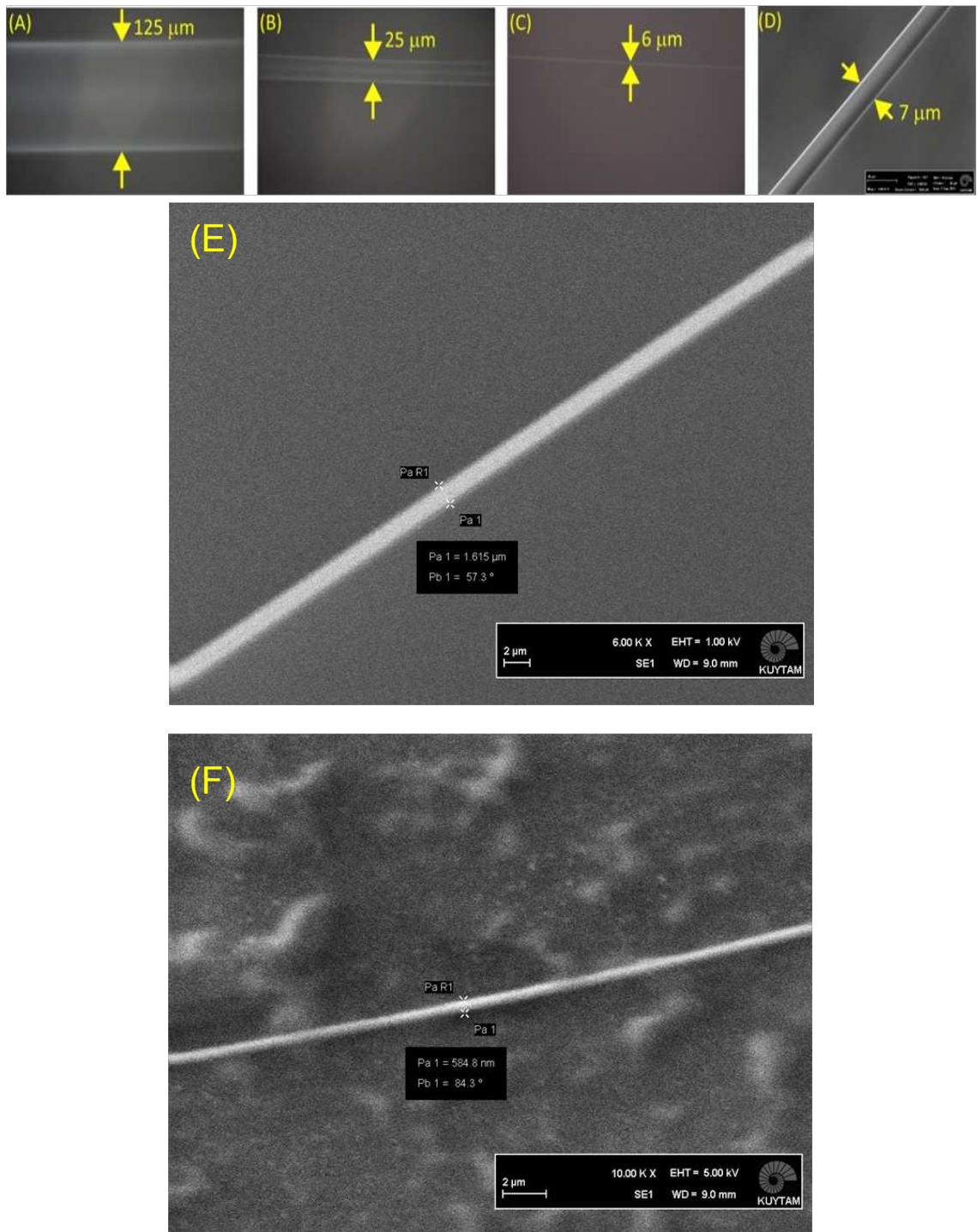
Figure 5.3: Characterization of produced fiber tapers by direct optical imaging of the fiber during the fiber pulling (A) - (C) and by SEM imaging of final tapered fibers (D),(E),(F).

Pulling conditions warranting final taper transmissions higher than 80% were found.
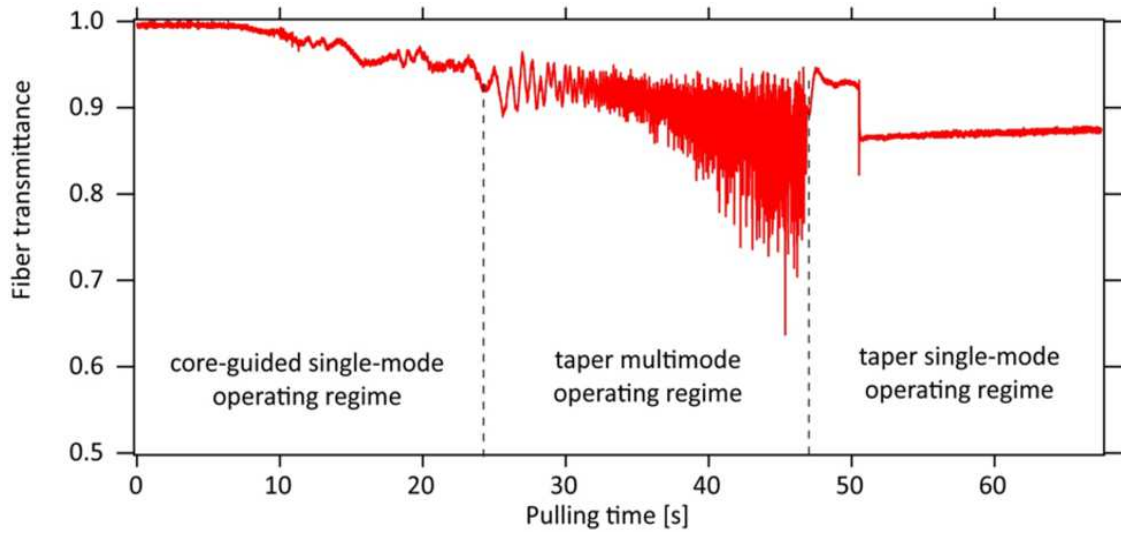
Figure 5.4: Transmission of the tapered fiber recorded during the taper pulling.

Transmission of the tapered fiber recorded during the taper pulling reveals the transition into the taper single-mode operating regime required for the WGM spectroscopy (see Fig. 5.4). As the fiber tapers, the core becomes extremely thin and the light is no longer confined between the core and cladding. Rather, the light is now confined by the boundary of the cladding and air. Once this transition occurs, multiple optical modes will be supported until the fiber is on order of 1 wavelength of light in diameter, in our case it is smaller than 1 μm. It is at this point, when the taper only supports the fundamental optical mode.

5.3 Design and Implementation of Custom Inverted Microscope for Optical Spectroscopy of Surface-supported Microdroplets Based on the Use of Tapered Optical Fibers

Custom inverted optical microscope frame providing necessary thermal and mechanical stability and flexibility for the optical spectroscopy of surface-supported microdroplets was devised and realized (see Fig. 5.5a). In order to stabilize the size of the studied droplets, the microscope features a sample chamber the relative humidity of which can be adjusted in a wide range using saturated solutions of suitable inorganic salts (relative humidity typically ranges from 53% with magnesium nitrate to 97% with potassium sulfate). Controlled 3-D positioning of the tapered fiber relative to selected individual droplets on the superhydrophobic surface was achieved with sub-micron resolution(see Fig. 5.5b).
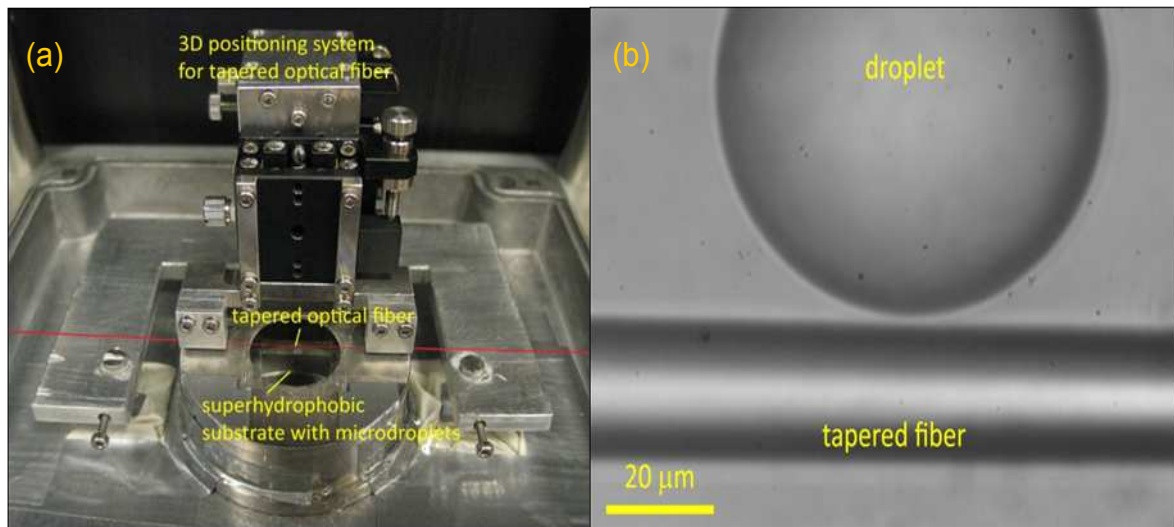
Figure 5.5: (a) 3-D positioning system for adjusting the relative position of the taper and a selected droplet with sub-micron precision. (b) Detail of a tapered optical fiber positioned in the vicinity of a surface-supported microdroplet of water/glycerol mixture.

Performance of the the microscope was evaluated in the studies of mechanical resonances of vibrated microdroplets and the analyses of the temporal stability of droplet size in the humidity sample chamber (see Fig. 5.6).
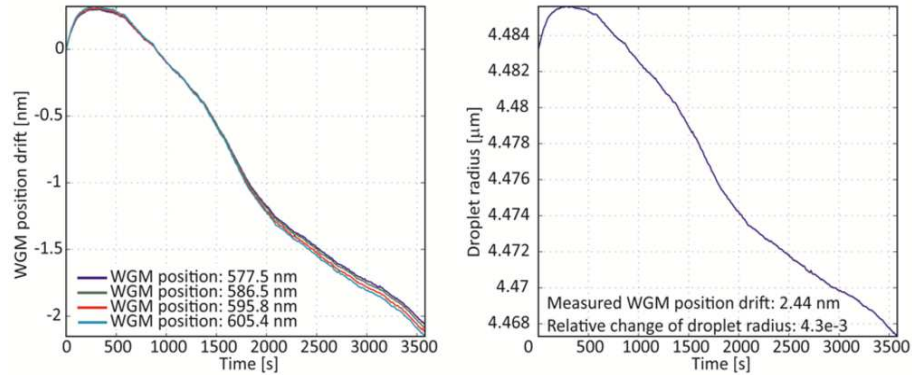
Figure 5.6: Measurements of the droplet size stability in the humidity sample chamber reveal typical shift of the WGM position on the order of 3 nm/hour. This corresponds to the relative change of the droplet size smaller than 5e-3/hour.

5.4 Whispering Gallery Mode of a Bare Optical Fiber

We tested the produced tapered fibers and the custom microscope system with a cylindrical solid microresonator. A standard 125 μm diameter single mode optical fiber was used as a cylindrical microresonator. Buffer removal was achieved using a standard fiber stripper. Light was coupled into WGMs of the cylindrical microresonator via the evanescent field generated by the tapered region of the second fiber(see Fig. 5.7).
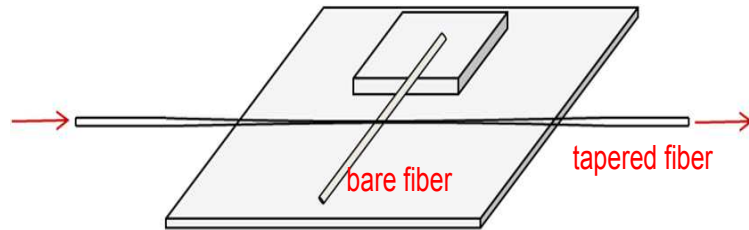
Figure 5.7: A sketch for the cylindrical solid microresonator excited by a tapered optical fiber.

The light source used to excite whispering gallery modes in the microresonator was a 5 mW Laser, tunable over the range from 632.5 nm to 637 nm(TLB-6300 Velocity, New Focus). The detectors for measuring the power transmitted through the tapered fiber during laser wavelength tuning and incident power coupled into the taper were was Thorlabs DET110 high speed silicon detectors. In order to eliminate the influence of changes in the

taper input power on the measured taper transmission spectra, the measured transmitted power was normalized by the incident power. When the two fibers were separated, the measured normalized transmitted signal was flat. Upon decreasing the distance between the two fibers, light could couple from the tapered optical fiber into the cylindrical resonator, resulting in transmission dips at specific input light wavelengths corresponding to the WGMs of the cylindrical resonator. The mode structure of the WGM spectrum depended on the position of the bare fiber relative to the tapered fiber. Small fluctuations in the position could have important effects on the relative coupling efficiencies into different modes.
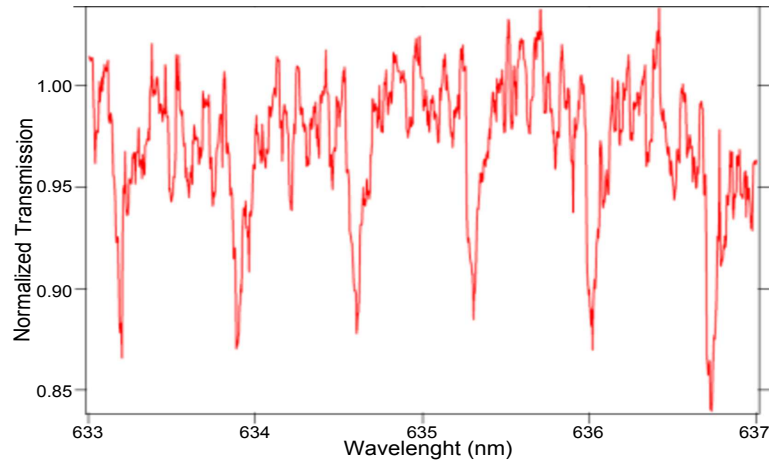
Figure 5.8: Experimentally measured WGM spectrum for a 125 μm diameter bare fiber. The free spectral range is 0.72 nm.

The series of equally spaced dips corresponded to WGMs which had different azimuthal wave numbers. By using $Q = \lambda_0/\Delta\lambda$, Q-factor of a bare fiber was calculated and found to be around 10^3. This result agrees well with the reported Q-factor of the bare fiber [71]. The free spectral range of the fiber cavity $\Delta\lambda$, *i.e.*, the spacing between two adjacent transmission dips, is given by

$$\Delta\lambda = \frac{\lambda^2}{n\pi d} \tag{5.3}$$

where n and d are the refractive index and the fiber diameter, respectively. Eq. 5.3 gives 0.71 nm for 125 μm silica fiber. This result is very close to the measured free spectral range of fiber cavity.

Chapter 6

PROBING OF ULTRAHIGH OPTICAL Q-FACTORS OF INDIVIDUAL LIQUID MICRODROPLETS IN AIR USING TAPERED OPTICAL FIBER WAVEGUIDES

6.1 Introduction[1]

Ultrahigh-quality (ultrahigh-Q) optical resonant microcavities that confine and concentrate light to small modal volumes enable optical fields to interact strongly with dipolar emitters embedded in the cavity or with mechanical degrees of freedom of the cavity [72]. Moreover, the spectral positions of their optical resonances are very sensitive to changes in the shape and / or composition of the cavity or its environment. These properties make ultrahigh-Q microcavities ideally suited for applications in cavity QED, cavity opto-mechanics, and label-free biological sensing [72, 73, 74, 75].

The Q-factor of an optical resonant mode can be defined as

$$Q = \frac{\omega}{\delta\omega} = \frac{\lambda}{\delta\lambda}, \tag{6.1}$$

where ω (λ) is the resonant frequency (wavelength) and $\delta\omega$ ($\delta\lambda$) is the resonance linewidth.

Droplet-based optical cavities have been subject to extensive theoretical and experimental studies. Chylek calculated the spacing between the neighboring WGMs of oil droplets and compared the theoretical results to experimental data with $\sim 1\%$ accuracy [76]. Eversole $et\ al.$ studied the spectral positions of WGMs and used them to determine the droplet refractive index [47, 77]. In a number of experimental investigations, dye lasing [22, 78, 79, 80, 81, 82], stimulated Raman scattering [83, 84, 7, 85], and Raman lasing [86, 87] from droplets of various liquids surrounded by air or another immiscible liquid with low index of refraction have been analyzed and characterized. At visible wavelengths, absorption-limited Q-factors of $\sim 10^8$ have been predicted for the first order WGMs of water

---

[1]This work has been published in "Probing of ultrahigh optical Q-factors of individual liquid microdroplets in air using tapered optical fiber waveguides", J. Opt. Soc. Am. B 29 (12), 3240-3247 (2012)

microdroplets in air with a size parameter $\alpha = 2\pi a/\lambda$ (a and λ being the droplet radius and the light wavelength, respectively) larger than ~ 60 [9]. Experiments involving a stream of liquid microdroplets floating in air have revealed Q-factors up to 5×10^5, using measurements of photon lifetime of light scattered elastically from the droplets [88]. In addition, experiments with cavity-enhanced energy transfer between donor and acceptor molecules have suggested Q-factors of $\sim 5 \times 10^6$ for the WGMs of single electrodynamically levitated glycerol microdroplets in air [89, 90]. Despite these demonstrations, characterization of Q-factors of liquid microdroplets in air based on direct high-resolution determination of WGM linewidths has not been reported. The main experimental challenge of such measurements lies in stabilizing the droplet position and size during the measurement and simultaneously coupling efficiently the probe laser light into the droplet.

In this chapter, we demonstrate direct, linewidth-based measurements of ultrahigh-Q factors of individual optical resonances excited in liquid microdroplets surrounded by air. The droplets were deposited on a superhydrophobic surface and their WGMs were probed using tapered optical fiber waveguides. The experimental configuration with a superhydrophobic surface is robust, easy to implement, and preserves the spherical shape of the microdroplets while stabilizing their position [4]. Thus, it simplifies significantly the measurements of Q-factors of liquid droplets in air and allows prolonged investigation of individual droplets. In our experiments, the droplet size was stabilized by adding glycerol to the aqueous droplets and keeping the droplets in a closed chamber with controlled relative humidity. We used a tapered optical fiber waveguide to couple light from a narrow-linewidth tunable laser into an individual surface-supported droplet of glycerol-water mixture and measured the fiber transmission as a function of the laser wavelength. Tapered optical fiber coupling is commonly used for characterizing ultrahigh-Q microcavities [72, 73, 74, 75]. In contrast to free space coupling, fiber tapers allow selective phase-matched excitation of individual WGMs [10] with a coupling efficiency better than 90% [70] and a spectral resolution limited only by the linewidth of the laser used. We note that Q-factors of individual liquid droplets have been previously characterized using tapered fibers [91]. In that work, the studied aqueous droplets were immersed in an immiscible cladding liquid that prevented evaporation of the droplet liquid. While this approach provided stabilization of the droplet size, simultaneous requirements of liquid immiscibility and refractive index contrast put limits on the suitable

droplet / immersion medium liquid pairs.

6.2   Experimental Setups and Procedures

The experimental setup used for the ultrahigh-Q WGM spectroscopy of surface-supported liquid microdroplets is depicted in Fig. 6.1. Tapered optical fiber waveguides were manufactured from a single-mode optical fiber (SM600; Thorlabs) by heat-pull method using a stationary hydrogen flame [8, 92]. During the taper pulling, the transmission of light from an auxiliary laser ($\lambda = 637$ nm) through the formed taper was monitored and the pulling of the fiber was halted when oscillations in the transmitted light intensity ceased. Since these oscillations arose due to interference of multiple transverse modes propagating in the fiber, their disappearance indicated single-mode operation of the taper [92]. The transmission of the final tapers was typically higher than 90% and SEM imaging revealed taper diameters in the range of 500–700 nm. The taper was mounted on a 3-axis piezo stage (Tritor 102SG; Piezosystem Jena) that allowed fine positioning of the taper with respect to the droplet with a resolution better than 2 nm. Individual droplets of glycerol-water mixture were deposited on the superhydrophobic surface at ambient room humidity ($\sim 42 - 44\%$) using a glass microcapillary connected to a syringe. The initial concentration of glycerol in the mixture was 47.8% w/w; however, this increased after the droplet deposition due to the evaporation of water in the low-humidity ambient environment. Subsequently, the surface with a single droplet and the mounted taper were enclosed in a chamber having a total volume of ~ 1.9 L with its relative humidity adjusted to 53% by a saturated solution of magnesium nitrate. At this relative humidity and with an ambient temperature of ~ 23 °C, the equilibrium concentration of glycerol in the droplet is 77.1% w/w [93] which corresponds to a refractive index $n_D = 1.439$ [27]. The experiments were carried out within 2 hours after the droplet deposition. During this time, the humidity in the sample chamber gradually approached the equilibrium value of 53% and the droplet size roughly stabilized. Typical equilibrium radius of droplets used in the Q-factor measurements ranged from ~ 100 μm to ~ 200 μm. Light from a tunable external-cavity diode laser (tuning range 632.5–637 nm, linewidth < 300 kHz, Velocity 6304; New Focus) was coupled into the tapered fiber that was then brought to the proximity of the droplet to induce coupling between the taper and the droplet. While approaching the taper to the droplet, we recorded simultaneously the taper transmission

spectra and stopped approaching when we observed resonant transmission dips with a sufficient modulation depth (more than 20%). Since efficient coupling between the taper and the droplet requires overlap of evanescent fields of the two objects, the distance between the taper and the droplet was on the order of the penetration depth of the evanescent field $d = \lambda/(2\pi(n_D^2 - 1)^{1/2})$ [94]. For our experimental conditions, $d \approx 100$ nm. In order to minimize the absorption of the pump laser light in the droplet liquid, we carried out the measurements in the visible part of the spectrum where both water and glycerol are virtually non-absorbing. The laser power was monitored both at the input and the output of the tapered fiber and the measured taper transmission was normalized by the input power in order to cancel out the laser power variations during wavelength tuning. Wavelength scans of the tunable probe laser were carried out at low and high resolutions. During the low-resolution scans, the position of the tuning mirror inside the laser was changed by a DC motor with a spectral resolution of 0.02 nm over the whole 4.5 nm tuning range. These low-resolution scans were used to determine the free spectral range of the droplet cavity. Due to the DC motor actuation of the tuning mirror, the low-resolution scans were slow (scan duration ~ 100 s).

In contrast, droplet WGM spectra with the resolution limited by the laser linewidth (<300 kHz) were acquired in the high-resolution scans that were performed within the ~ 90 GHz mode-hop free tuning range by the displacement of the tuning mirror with a piezoelectric transducer. The calibration of wavelength tuning in the high-resolution scans was carried out using a scanning Fabry-Perot interferometer. The high-resolution spectra over the full fine-tuning range of $\sim$125 pm with the laser linewidth-limited resolution of $\sim$0.4 fm could be acquired in approximately 2 seconds.

6.3   Results

6.3.1   Stability of Droplet Shape and Size

Figure 6.2 shows a side view of a representative glycerol-water microdroplet standing on a superhydrophobic surface. This figure illustrates the very good sphericity of the droplet shape and its high contact angle on the superhydrophobic surface (typically $> 155°$). We analyzed the droplet shape by locating the droplet contour in the images and fitting this contour with a circle using a custom-written routine implemented in IgorPro (WaveMetrics).
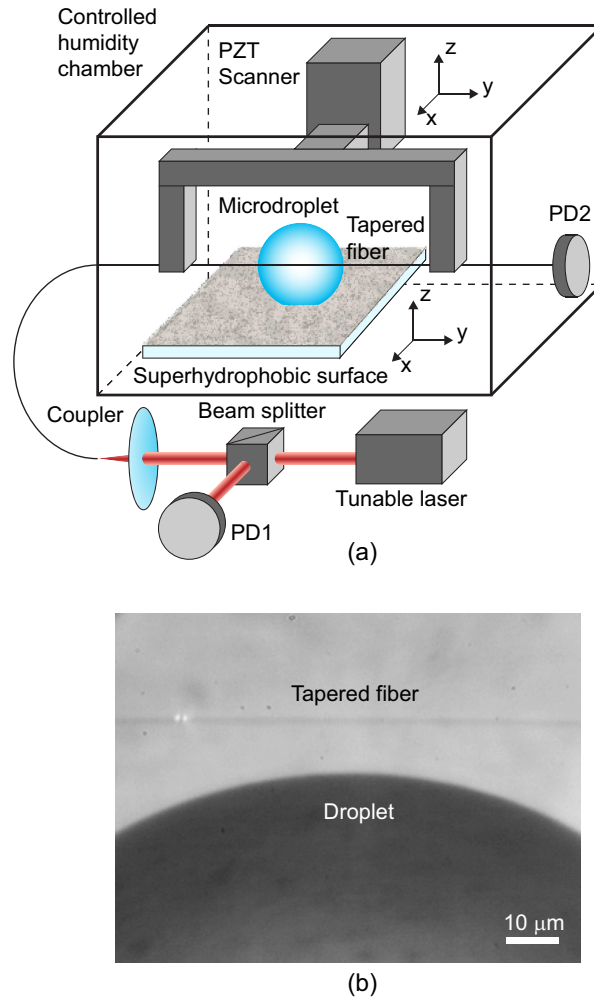
Figure 6.1: (a) Experimental setup for ultrahigh-Q spectroscopy of surface-supported liquid microdroplets. PD1 (PD2) – photodetectors monitoring the light power at the input (output) of the tapered fiber. (b) Image of a surface-supported glycerol-water microdroplet with a tapered fiber positioned in its equatorial plane (view along the z-axis).

From the shape analysis, we obtained the relative rms difference between the true droplet contour and the best-fit circle $D/a \approx 0.2\,\%$ where D is the absolute rms difference between the true contour and the fit and a is the droplet radius. The droplet was deformed towards an oblate spheroid which is consistent with gravity-induced deformation (see Section 6.3.2). In order to asses the stability of surface-supported droplets, we monitored the same droplet exposed to the ambient room conditions (average relative humidity $\sim 55\%$, temperature 25°C) for an extended period of time (up to three days). Comparison of the top and bottom images in Fig. 6.2 that were acquired with a time separation of 24 hours shows that
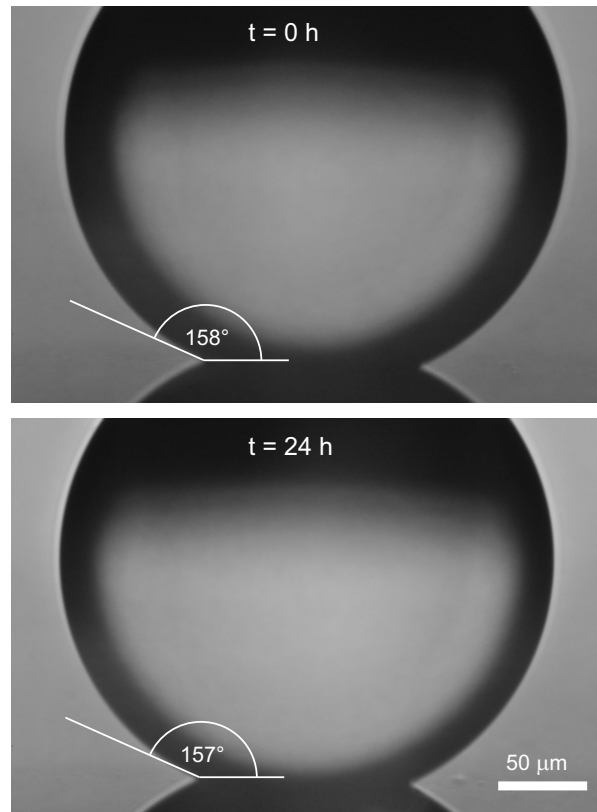
Figure 6.2: Images of a glycerol-water microdroplet standing on a superhydrophobic surface
(side view along the surface plane). Images were acquired at different times t elapsed since
the droplet generation.

a prolonged exposure of the droplet to ambient atmosphere did not have any influence on
the droplet contact angle and overall shape. The droplet shape analysis revealed a slight
decrease of the droplet size in 24 hours (relative radius change $\sim 2\%$). This size change can
be attributed to the fluctuations in the ambient room humidity between the acquisition of
the subsequent images.

In Fig. 6.3, a typical low-resolution transmission spectrum of a tapered fiber waveguide
coupled to a microdroplet is shown. The average optical input power coupled into the taper
was approximately $60\,\mu$W. Despite the residual variations of the non-resonant transmission
background during the wavelength scan, sharp transmission dips corresponding to the exci-
tation of individual WGMs of the droplet cavity are clearly visible. The overall structure of
the WGM spectra is rather complex with the mode degeneracy largely lifted due to a slight
droplet deformation by gravity and contact line pinning on surface inhomogeneities (see
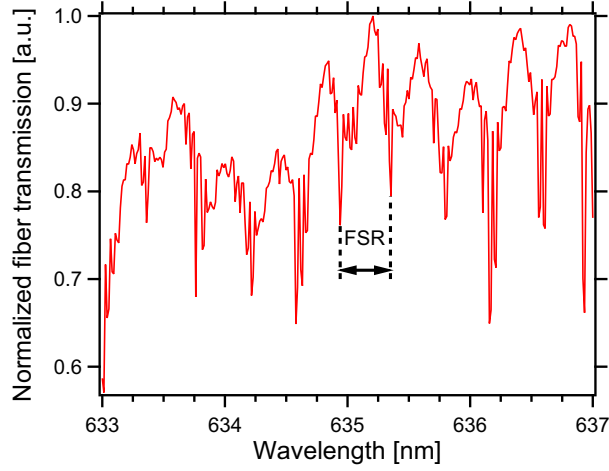
Figure 6.3: Low-resolution transmission spectrum of a tapered fiber waveguide coupled
to a glycerol-water droplet in air as a function of the pump laser wavelength. Spectrum
acquisition time was ~ 100 s. FSR indicates the free spectral range of the microdroplet
cavity (FSR = 0.414 nm).

also the discussion in Section 6.3.2). Thus, we did not attempt to assign the observed taper

transmission dips to specific mode orders. Using the asymptotic formula of Chylek [95]

$$a = \frac{\lambda^2}{2\pi\,\text{FSR}} \frac{\arctan([n_D^2 - 1]^{1/2})}{([n_D^2 - 1]^{1/2})} \tag{6.2}$$

and assuming an effective refractive index of $n_D = 1.439$ for the glycerol-water mixture at

53% relative humidity, we calculated the droplet radius a from the free spectral range (FSR)

of 0.414 nm at the mean wavelength $\lambda = 635$ nm to be $a = 120\,\mu$m. This value matched

well the radius of ~ 127 μm obtained from the droplet image analysis, considering ambiguity

in defining precisely the location of the droplet boundary in the image that furthermore

depends on microscope focusing. For droplets much larger than the light wavelength, the

FSR given by Eq. (6.2) is rather insensitive to the droplet radius changes Δa (the FSR

change $\Delta\text{FSR} \sim -(\lambda/a)^2\Delta a$) [95, 76]. On the other hand, the observed shift of the absolute

WGM positions $\Delta\lambda$ scales with Δa as [65]

$$\Delta\lambda = \left(\frac{\lambda}{a}\right)\Delta a. \tag{6.3}$$

Consequently, at $\lambda = 635$ nm and $a = 120\,\mu$m, even a modest resolution of $\Delta\lambda = 0.1$ nm in

detecting the WGM position corresponds to the smallest resolvable change of the droplet

radius $\Delta a = 18.9$ nm which is well below the typical effective pixel size of CCD detectors

used in high-resolution optical microscopy (~ 65 nm, assuming physical pixel size $6.45\,\mu\mathrm{m}$ and 100-times optical magnification [96]). Hence, tracking of the absolute position of a selected WGM provides much more precise information on the droplet size changes than the analysis of the droplet image. For this reason, all quantifications of the droplet size changes in the following text are based on the WGM position tracking.
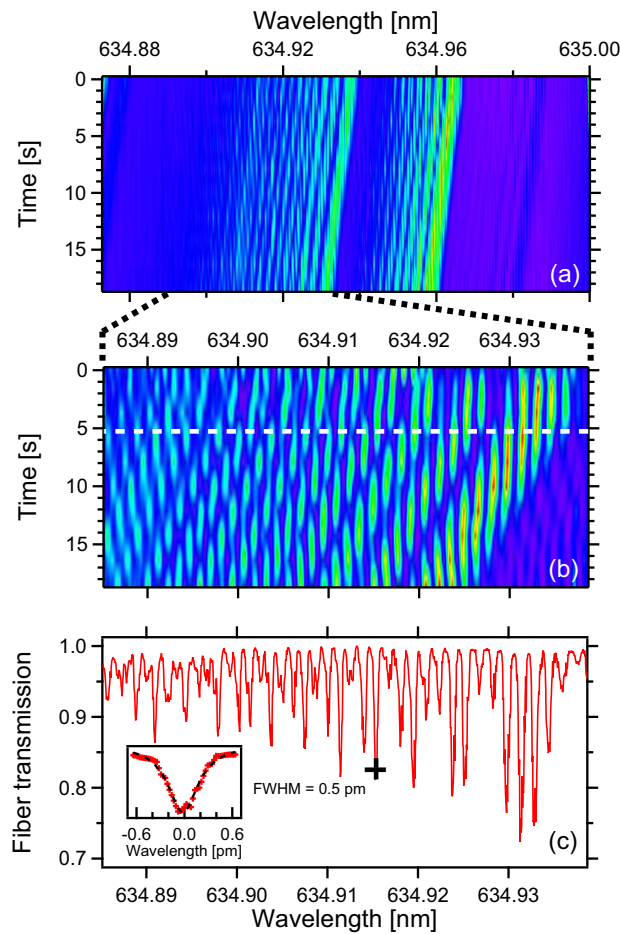
Figure 6.4: High-resolution transmission spectrum of a tapered fiber waveguide coupled to a glycerol-water droplet in air as a function of the pump laser wavelength and time. (a) Time series of transmission scans over the whole fine-tuning range of the laser (spectral interval width ~ 125 pm). (b) Time series of transmission scans over the tuning range occupied by a group of WGMs shown in the left part of spectral map (a) (spectral interval width ~ 54 pm). (c) Spectral profile of the tapered fiber transmission along the dashed white line shown in spectral map (b). Black cross denotes a representative WGM used for the Q-factor analysis (see graph inset and text). Average droplet radius was $130\,\mu\mathrm{m}$ and rate of the droplet radius change was $-0.17\,\mathrm{nm/s}$.

Repeated high-resolution wavelength scans of the taper transmission revealed spectral

shifting of the observed WGM structure that indicated changes of the droplet size. In Figs. 6.4a,b, an illustration of the WGM structure drifting as a whole to the blue end of the spectrum is given. Here, blue-shifting of the modes indicates decreasing size of the droplet that is accompanied by shortening of the resonant modal path in the droplet; correspondingly, red-shifting of the modes is the sign of the droplet size increase. In general, the droplet radius evolves with time as a result of a complex interplay between evaporation and condensation processes and, thus, the size of the loaded droplet can both decrease and increase. The dynamics of changes of the droplet size then depends on the total probe power coupled into the droplet and deviations from the thermodynamic equilibrium between the liquid and gas phases in the humidity chamber. For the example spectral recording presented in Fig. 6.4, the rate of the droplet radius change determined from Eq. (6.3) for the measured spectral drift of $-0.83\,\mathrm{pm/s}$ and the average droplet radius of $130\,\mu\mathrm{m}$ was $-0.17\,\mathrm{nm/s}$. Since our experiments were typically carried out on the time scale of ~ 2 hours, the above rate of the droplet size change corresponds to the relative droplet size stability of $\sim 0.9\,\%$ over the duration of an experiment.

6.3.2 Lifting of Azimuthal Mode Degeneracy

A spherical resonant cavity with radius a and refractive index n_s can host WGMs characterized by a radial mode number n, an angular mode number l, and an azimuthal mode number $m = \pm l, \pm(l-1), ..., 0$. For a perfect sphere, the azimuthal modes m corresponding to a given l are spectrally $(2l+1)$-degenerate. Deformation of the sphere towards a spheroid with polar and equatorial radii r_p, r_e, respectively, leads to the lifting of the azimuthal mode degeneracy. Resonant frequency of the mth mode is then given by [97, 98]:

$$\omega(m) = \omega_0 \left(1 - \frac{e}{6} \left[1 - \frac{3m^2}{l(l+1)} \right] \right). \tag{6.4}$$

Here, ω_0 is the frequency of the original degenerate mode of the unperturbed sphere and the eccentricity of the spheroid is $e = (r_p - r_e)/a$. The value of e is positive for a prolate spheroid and negative for an oblate spheroid.

The equilibrium shape of droplets deposited on a superhydrophobic surface is the result of the interplay between the forces of surface tension and gravity. In general, sessile droplets tend to be flattened by gravity, and for small deformations the droplet shape is well ap-

proximated by an oblate spheroid [99]. Besides gravity, the droplet shape can be perturbed by other factors, the most prominent of which is inhomogeneity of the superhydrophobic surface that causes pinning and distortion of the droplet contact line. Consequently, the droplet shape departs from that of a perfect sphere or a rotationally symmetrical spheroid. All additional distortions that increase the droplet eccentricity lead to further frequency splitting of the azimuthal m-modes.

Droplet eccentricity e can be estimated from the measured mode frequency splitting. From Eq. (6.4), the frequency difference $\Delta\omega(m)$ between two neighboring m-modes is

$$
\begin{aligned}
\Delta\omega(m) &= \omega(m+1) - \omega(m) = \\
&= \frac{\omega_0 e}{l(l+1)}\left[m + \frac{1}{2}\right].
\end{aligned}
\tag{6.5}
$$

For a glycerol-water droplet with radius $a = 130\,\mu$m and refractive index $n_s = 1.44$ probed with a mean laser wavelength $\lambda = 635$ nm, the approximate value of l is:

$$
l \approx \frac{2\pi\,a\,n_s}{\lambda} \approx 1852 \gg 1.
\tag{6.6}
$$

Moreover, in our experimental geometry (excitation of droplet WGMs via a tapered fiber located at the droplet equatorial plane), we excite most efficiently the WGMs with $|m| \approx l$ and the intensity of the observed WGMs falls off rapidly with increasing value of $(l - |m|)$ [91]. Hence, Eq. (6.5) simplifies to

$$
\Delta\omega(m) \approx \frac{\omega_0 e}{l^2}\left[m + \frac{1}{2}\right] \approx \frac{\omega_0 e}{l},
\tag{6.7}
$$

and, upon substituting (6.6) into (6.7), we obtain

$$
e \approx \frac{\Delta\omega(m)}{\omega_0}\frac{2\pi\,a\,n_s}{\lambda} = \frac{2\pi\,a\,n_s\,\Delta\lambda}{\lambda^2},
\tag{6.8}
$$

where $\Delta\lambda$ is the measured mode splitting. For the spectrum presented in Fig. 6.4c, the spacing of neighboring modes is ≈ 1.5 pm. Because of the mode excitation symmetry (the taper located in the droplet equatorial plane), odd azimuthal modes are not excited and the observed mode separation is actually equal to $2\Delta\lambda$ [91]. Therefore, $\Delta\lambda \approx 0.75$ pm and the droplet eccentricity $e \approx 2.2 \times 10^{-3}$. This value of eccentricity is comparable to the rms droplet shape distortion of $\sim 2 \times 10^{-3}$ that was obtained from the droplet shape analysis presented in Section 6.3.1.

6.3.3   Q-Factor Measurements

In order to characterize the Q-factors of WGMs of surface-supported liquid microdroplets, we conducted series of relatively fast, high-resolution spectral scans over a narrow spectral range of 54 pm within 2.06 s. In Fig. 6.4c, an example of such high-resolution spectral recording is presented for a group of WGMs collectively drifting to the blue end of the spectrum. This group of WGMs consists of an intense long-wavelength mode accompanied by a number of shorter-wavelength modes whose intensities decrease with decreasing wavelength. Such a spectrum is consistent with a family of WGMs with the same angular and radial mode numbers and different azimuthal mode numbers originating from the degeneracy lifting in a sphere deformed towards an oblate spheroid (see Section 6.3.2). Here, the longest-wavelength mode corresponds to the highest absolute value of the azimuthal mode number that belongs to the modes circulating in the droplet equatorial plane [97, 98]. In accordance with Eq. (6.2), the relative positions of individual WGMs are virtually unaffected by the droplet size drift. A Lorentzian fit of a representative WGM denoted by a black cross in Fig. 6.4c gave the mode FWHM $\delta\lambda = 0.5$ pm. Knowing $\delta\lambda$, Q-factor at the mean laser wavelength $\lambda = 635$ nm could be determined using Eq. (6.1). Since the droplet size changed slightly during the spectrum acquisition, Q-factor should be calculated after correcting the measured FWHM for the spectral drift of WGMs. Our high-resolution spectral scans were carried out from red to blue wavelengths; thus, for a blue-drifting mode, the true FWHM of the mode is smaller than the measured one. Taking into account the measured rate of the WGM position drift of ~ 0.8 pm/s and the spectral acquisition rate of 54 pm/2.06 s ≈ 26.2 pm/s, we obtain the true FWHM of ~ 0.485 pm and, consequently, Q-factor of 1.31×10^6 for the selected WGM.

Images of a glycerol-water microdroplet on a superhydrophobic surface presented in Fig. 6.2 suggest that the droplet shape and contact angle are stable on the time scale of hours. This implies that the optical properties of surface-supported microdroplet cavities should not change significantly after the droplet deposition.

In Fig. 6.5, time evolution of the Q-factor of a single microdroplet is presented within the interval of ~ 1 hour following the droplet deposition. Values of Q-factors were determined using the above described procedure. In order to minimize the possibility of forming a liquid bridge between the tapered fiber and the droplet, the taper was repeatedly moved
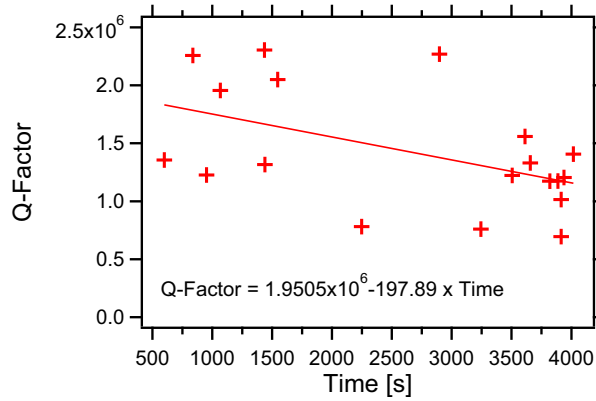
Figure 6.5: Time evolution of the Q-factor of degeneracy-lifted azimuthal WGMs of a
surface-supported microdroplet. Time $t = 0$ s corresponds to the droplet deposition on the
surface. Crosses represent experimental data, line is the linear fit of this data. Average
droplet radius was $150\,\mu$m.

towards and away from the droplet between consecutive Q-factor measurements. Therefore,
it is likely that modes with different angular and azimuthal numbers were characterized in
individual measurements shown in Fig. 6.5. As illustrated by this figure, the characteris-
tic Q-factors of degeneracy-lifted azimuthal WGMs of the droplet decreased slightly with
time. While we did not observe any discernible changes in the droplet shape over several
hours, it is likely that contaminant particles originating from the droplet liquid and / or
slowly dissolving superhydrophobic surface accumulated at the liquid-air interface during
this time. Such accumulation of contaminant particles would then lead to an increase in
the light scattering at the droplet surface and, thus, increased loss of the cavity which is
equivalent to a lower Q-factor. It is worth noting it is not possible to observe directly
binding of individual nanoparticles forming the superhydrophobic surface to the droplet
since the mass of nanoparticles ($\sim$3.8 attogram / particle) is too small to cause a detectable
shift of the WGM positions [100]. Hence, accumulation of nanoparticles on the droplet
surface manifests itself as a continuous process rather than a sequence of discrete jumps
of the WGM properties. In addition, unlike with solid cavities, contaminant particles on
liquid surfaces are not immobilized but instead diffuse in and out of the WGM field which
further smears the optical response of the cavity. Despite the slight decrease with time, the
droplet Q-factor remains on the order of 10^6. Consistence of this value with the expected
experimental limits on the measured Q-factors is discussed in the next section.

6.4   Experimental Limits on Measured Q-factors

6.4.1   Contributions to Overall Q-Factor of a Resonant Cavity

In general, the overall quality factor Q defined by Eq. (6.1) consists of several components:

$$\frac{1}{Q} = \frac{1}{Q_{\text{rad}}} + \frac{1}{Q_{\text{mat}}} + \frac{1}{Q_{\text{s.s.}}}, \tag{6.9}$$

where $1/Q_{\text{rad}}$ characterizes losses of the resonant cavity due to radiation, $1/Q_{\text{mat}}$ describes losses due to material absorption and bulk scattering, and $1/Q_{\text{s.s.}}$ is the contribution of scattering from surface inhomogeneities [65, 101]. In perfect spheres with $2a/\lambda \geq 15$, radiative quality factor $Q_{\text{rad}} > 10^{11}$ [101]. In spheroids characterized by eccentricity e, photon paths generally depart from ideal circularity. This results in a lowering of Q_{rad} relative to undeformed spheres which is proportional to e^2 and negligible for WGMs with modal paths localized in the equatorial plane of the spheroid [102]. As these are the modes we predominantly excite and characterize in our experimental geometry, we can assume that the value of Q_{rad} is approximately unaltered by the droplet deformation. Material-related quality factor Q_{mat} represents typically the main limit for the overall Q. This contribution can be expressed as

$$Q_{\text{mat}} = \frac{2\pi \, n_s}{\alpha \, \lambda}, \tag{6.10}$$

where α is the linear absorption coefficient of the cavity material and n_s is the cavity refractive index at wavelength λ. For glycerol-water mixture at $\lambda = 635$ nm, $\alpha \approx 2.8 \times 10^{-3} \text{cm}^{-1}$ [103] and $n_s = 1.44$ [27], and, thus, $Q_{\text{mat}} \approx 5 \times 10^7$. Finally, $Q_{\text{s.s.}}$ can be expressed as

$$Q_{\text{s.s.}} = \frac{\lambda^2 \, a}{\pi^2 \, \Delta^2 \, B}, \tag{6.11}$$

with Δ being the rms size of surface inhomogeneities and B their correlation length [101]. For glycerol-water droplets, thermal fluctuations of the droplet shape lead to $\Delta \approx 0.07$ nm (see Eq. (6.12)) and B can be estimated from the characteristic wavenumber q of the maximal liquid surface roughness ($q \sim 10^7 \text{ cm}^{-1}$) as $B \approx 2\pi/q \approx 6.3$ nm [104]. Assuming further that the droplet radius $a = 130 \, \mu\text{m}$, $Q_{\text{s.s.}} \approx 1.7 \times 10^{11}$.

From the above analysis, it follows that the expected limit on the intrinsic value of Q-factor measured in our experiments is set by Q_{mat} at the level of $\approx 5 \times 10^7$. This limit, however, is approximately 10 times larger than the maximum observed Q-factors. As argued

in Section 6.4.2, we attribute this difference to thermally-induced droplet shape fluctuations
that lower the Q-factor values measured with the use of tapered optical fibers.

6.4.2   Fluctuation of Mode Position Due to Thermally-Induced Droplet Shape Fluctuations

Due to thermal excitation, droplet shape undergoes random dynamic distortions with a
characteristic amplitude given by [105]:

$$\Delta = \left[\frac{k_B T}{4\pi\gamma}\right]^{1/2},\tag{6.12}$$

where k_B is the Boltzmann constant, γ is the glycerol surface tension(63.4 mN/m) and T is
the thermodynamic temperature. For a glycerol droplet at room temperature $T = 293°\text{K}$,
$\Delta \approx 0.07$ nm.

According to Eq. (6.4), the frequency $\omega(m)$ of the mth azimuthal mode depends linearly
on the droplet eccentricity e. Thus, a change in e leads to a corresponding change in $\omega(m)$:

$$\text{d}\omega(m) = -\frac{\omega_0}{6}\left[1 - \frac{3m^2}{l(l+1)}\right]\text{d}e.\tag{6.13}$$

Assuming droplet volume conservation upon deformation into a spheroid (i.e. $r_p\,r_e^2 = a^3$), a
shape distortion Δ in the direction of the droplet polar radius r_p is associated with a change
in eccentricity δe:

$$\delta e = \left[1 + \frac{1}{2}\left(\frac{a}{r_p}\right)^{3/2}\right]\frac{\Delta}{a}.\tag{6.14}$$

For glycerol–water microdroplets supported by a superhydrophobic surface, the droplet
distortion from sphericity is very small ($e \approx 2.2 \times 10^{-3}$) and also $\Delta/a \ll 1$. Thus, $r_p \approx a$
and

$$\delta e \approx \frac{3}{2}\frac{\Delta}{a}.\tag{6.15}$$

Upon substituting (6.15) into (6.13), we obtain a relative frequency spread of the mth mode
position as:

$$\frac{\text{d}\omega(m)}{\omega_0} = -\frac{1}{6}\left[1 - \frac{3m^2}{l(l+1)}\right]\frac{3}{2}\frac{\Delta}{a}.\tag{6.16}$$

Assuming again $l \gg 1$ and $|m| \approx l$, this simplifies to

$$\frac{\text{d}\omega(m)}{\omega_0} = \frac{1}{2}\frac{\Delta}{a}.\tag{6.17}$$

For the considered values of $\Delta = 0.07$ nm and $a = 130\,\mu\text{m}$, $\text{d}\omega(m)/\omega_0 \approx 2.7 \times 10^{-7}$. As
the amplitude Δ of the thermally-induced droplet shape fluctuations is much smaller than

the static droplet deformation due to gravity and contact line pinning $\Delta_g \approx ea \approx 286$ nm, degeneracy-lifted azimuthal modes of thermally-vibrating droplets remain well resolved and do not mix with each other [105].

Thermal fluctuations of the droplet shape typically occur in the frequency range of $\sim 10^5$ Hz. On the other hand, spectroscopic characterization of the droplet WGMs using a tapered fiber and a narrow–linewidth tunable laser was carried out on the time scale of ~ 1 s. Hence, the spectral measurement detects an "effective" width of the WGM given by (6.17). This in turn corresponds to an effective quality factor Q_{eff}

$$Q_{\text{eff}} = \frac{\omega_0}{\text{d}\omega(m)} = \frac{2a}{\Delta} \approx 3.7 \times 10^6. \tag{6.18}$$

It is this value of Q_{eff} (and not the intrinsic quality factor of the modes set by the value of Q_{mat} in our system) which represents an upper limit on the quality factors measurable with the current experimental setup. This finding is consistent with the experimental data presented in Figs. 6.4 and 6.5.

6.5   Conclusion

In this article, we have presented systematic experimental characterization of ultrahigh-Q resonant modes (WGMs) of liquid microdroplets surrounded by air. To this end, we have deposited the droplets of glycerol-water mixture on superhydrophobic surfaces with high contact angles and used light coupling from a tapered optical fiber waveguide to record the droplet WGM spectra. The measured Q-factors exceeded 10^6 and were stable on the time scale of an hour. We have shown that slight residual deformations of the droplet shape due to the presence of the superhydrophobic surface with the contact angle smaller than 180 degrees do not represent a restriction in the ultrahigh-Q spectroscopic measurements. Despite the high experimental values of the Q-factor, we have not reached the fundamental limit set by the light absorption in the droplets; our measurements have been limited by the thermally-induced shape fluctuations of the droplets. Even though the stability of the droplet size in air has been greatly improved by controlling the humidity of the ambient atmosphere, some residual drift of the droplet radius has been observed. This issue can be further improved by active photothermal control of the droplet size [93]. The experimental configuration involving a superhydrophobic surface has allowed for the first time prolonged

spectroscopic measurements on individual liquid droplets in air and simplified significantly efficient phase-matched light coupling into the droplets. Hence, it represents a well-suited platform for characterizing liquid-based micro-optical components.

Chapter 7

SIZE STABILIZATION OF SURFACE-SUPPORTED LIQUID
AEROSOLS USING TAPERED OPTICAL FIBER COUPLING

7.1   Introduction[1]

Liquid aerosol research is important for a large variety of fields including atmospheric chem-
istry and physics, combustion science, plasma physics, and health science [106, 107]. Such
studies require experimental tools for simultaneous manipulation and high-resolution char-
acterization of individual liquid aerosol particles. This is a challenging task due to the
airborne nature of aerosols which makes them difficult to localize and renders their chemi-
cal and physical properties (e.g. composition, size, and mixing state) very sensitive to the
composition and temperature of the surrounding gas. Localization of liquid aerosols has
been up to date successfully achieved with various approaches including the use of optical
levitation [6], electrodynamic levitation [108], acoustic levitation [109], optical tweezers [7],
and superhydrophobic surfaces [4]. In contrast, precise size stabilization is still an unresolved
issue that limits prolonged studies of individual liquid aerosol particles. Currently, size sta-
bilization of liquid aerosols is mostly accomplished by adding non-volatile components (e.g.
inorganic salt or glycerol) into their composition and keeping them in chambers with fixed
environmental conditions. This approach, however, is insufficient for high-resolution aerosol
characterization due to the difficulties in precise control of the environmental conditions
leading to size instabilities of the liquid aerosol particles.

Recently, an alternative method for self-stabilization of the size of aqueous microdroplets
based on heating with a free-space propagating laser beam has been demonstrated and
successfully applied to microdroplets immobilized on a superhydrophobic (SH) surface [110,
111] or by optical tweezers [112]. In these demonstrations, stable locking of the droplet size
resulted from the competition between droplet growth due to the condensation in a high-

---

[1]This work has been published in "Size-stabilization of surface-supported liquid aerosols using tapered
optical fiber coupling", Opt. Lett. 38 (5), 793-795 (2013)

humidity chamber and shrinkage due to the evaporation caused by resonant absorption of the
heating laser light either directly by water [111, 112] or by a dissolved fluorescent dye [110].
The stability of the droplet size was characterized by monitoring the spectral positions of
the droplet whispering gallery modes (WGMs) via fluorescence spectroscopy [110, 111] or
Raman spectroscopy [112].

Here, we demonstrate long-term size-stabilization of individual microdroplets standing
on a SH surface and coupled to single tapered optical fibers which guide simultaneously a
tunable red laser for the WGM probing [113] and an infrared (IR) heating laser. The use
of a tapered optical fiber for coupling both lasers into the droplets increases significantly
the coupling efficiency in comparison to the free-space arrangement adopted previously [10].
Moreover, droplet size stabilization and high-resolution WGM spectroscopy can be carried
out concurrently, with almost no increase in the setup complexity. We note that self-
stabilization of a solid microcavity coupled to a tapered fiber has been previously shown [114]
using cavity expansion and refractive index change caused by laser heating as the underlying
physical mechanisms.

7.2   Theory of Size-stabilization

Laser-induced heating of droplets depends strongly on the droplet radius a. When a is in
resonance with the heating laser wavelength (λ_H), light absorption and associated heating
can increase by several orders of magnitude. As shown by Karadag *et al.* [111], the size of a
growing droplet that is initially out of resonance with heating laser WGMs can be stabilized
at a certain size parameter $\alpha_S = 2\pi a_S/\lambda_H$ at which the water evaporation and condensation
precisely balance each other; this α_S is slightly blue-detuned with respect to a WGM of the
heating laser. Upon reaching α_S, further increase of size above a_S tunes the droplet closer
to the absorption resonance. This in turn causes increased heating which drives the droplet
back to α_S. Similarly, decrease of size with respect to a_S leads to a stronger condensation
since the heating power decreases farther from the resonance. Again, the droplet is driven
back to α_S. This mechanism then leads to the self-locking of the droplet size.

7.3   Experimental Setup

The experimental setup and procedures used for the size stabilization of surface-supported liquid microdroplets were similar to those described in Ref. [113]. SH surfaces were prepared by spin coating of hydrophobic silica nanoparticles suspended in isopropanol on cleaned glass substrates. Subsequently, individual microdroplets of aqueous solution of $MgCl_2$ (initial concentration 2 mM) with a typical radius $a = 245\,\mu m$ were manually deposited on the SH surface with a glass microcapillary. A fiber taper manufactured from a single-mode optical fiber optimized for 633 nm by heat-and-pull technique served to couple both probe and heating lasers into and out of the microdroplet [113, 10]. An XYZ piezo-stage was used to position the taper within the proximity of the droplet to allow light coupling. The microdroplet deposited on the SH surface was kept in a sealed chamber with its relative humidity fixed at 84% by a saturated water solution of KCl.
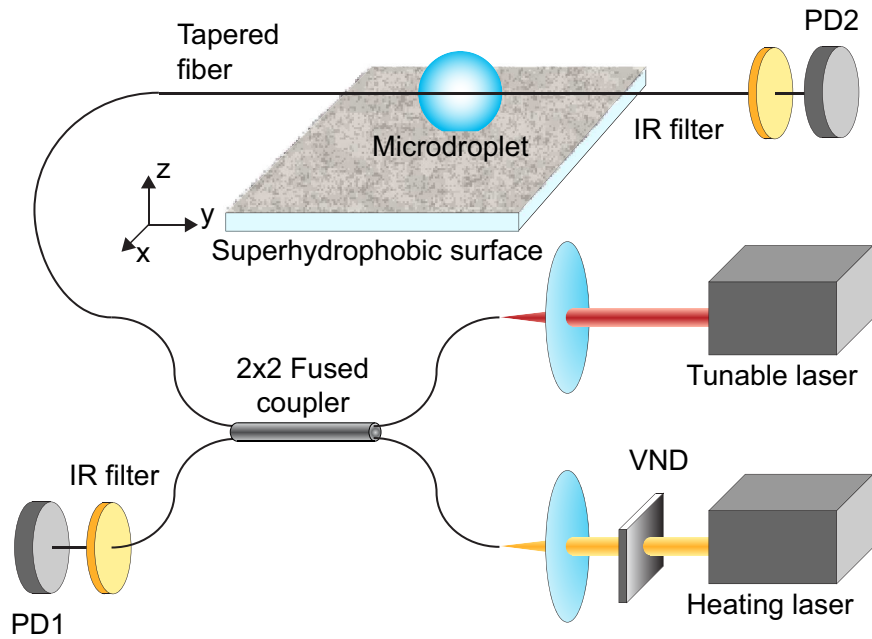
Figure 7.1: Experimental setup for size-stabilization of surface-supported liquid micro-droplets. PD1 (PD2) – photodetectors monitoring the light power at the input (output) of the tapered fiber.

A tunable probe laser ($\lambda_P = 638$ nm, tuning range 0.056 nm, linewidth < 300 kHz) and a fixed wavelength heating laser ($\lambda_H = 1064$ nm, linewidth < 17 MHz) were combined in the same tapered fiber using a fused fiber coupler(see Fig. 7.1) . In order to minimize

the absorption of the tunable probe laser light in the droplet liquid, we performed the measurements in the visible part of the spectrum where water is virtually non-absorbing. In contrast, the heating laser wavelength was selected to be in the IR region where water absorption is more than two orders of magnitude larger than that at visible wavelengths.

7.4   Results
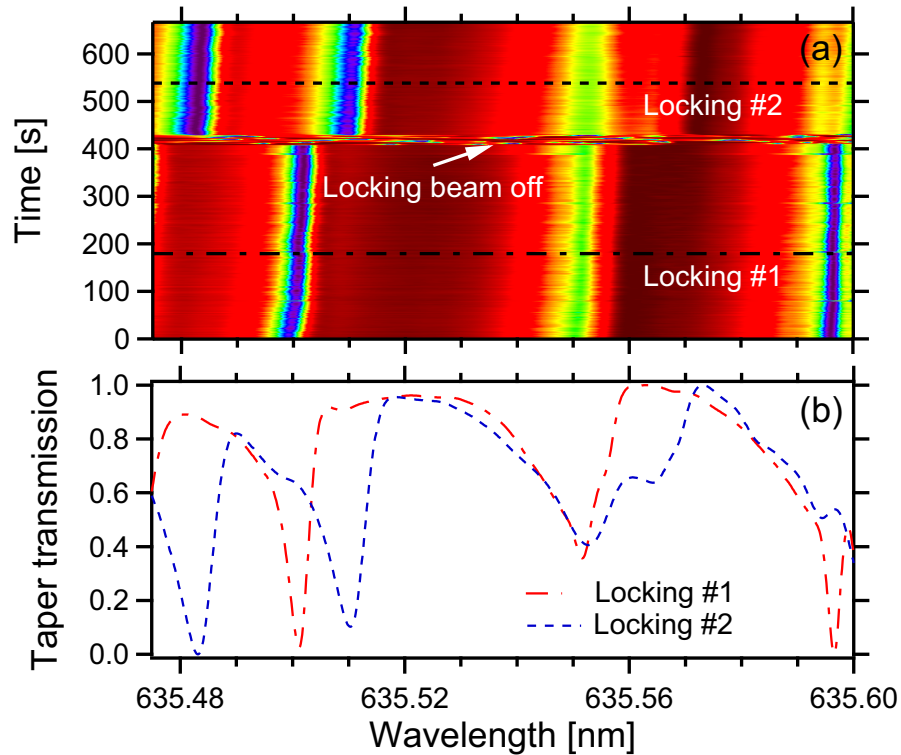
Figure 7.2: (a) 2-D plot of consecutive WGM spectra of a droplet stabilized by IR laser heating. At time t = 410 s, the heating laser was blocked during 10 spectral acquisitions and then unblocked again, resulting in a change of the stabilized droplet size. (b) Details of the droplet WGM spectra along the dash-dotted and dashed lines shown in (a). Droplet size was $245\,\mu$m

Fig. 7.2(a) shows a two-dimensional (2-D) plot of consecutive WGM spectra recorded from a microdroplet exhibiting size-locking. Laser powers used in this experiment were measured at the output of the fiber taper as 16.5 μW and 0.35 mW for the probe and heating lasers, respectively. Average acquisition time of an individual spectrum (a single horizontal line in the image) was 2.064 s. Prior to the spectrum acquisition, the microdroplet

was prepared at 73% ambient relative humidity and then placed in a closed sample chamber
with humidity fixed at 84%. Hence, upon chamber loading, microdroplet growth due to the
gradual condensation was observed. Results shown in Fig. 7.2 were recorded immediately
after the chamber loading, before the microdroplet reached its equilibrium size. For times
$t < 410$ s, both the probe and the heating lasers were coupled to the tapered fiber. During
this period, spectral positions of the WGMs remained virtually constant with only a small
red shift $\Delta\lambda = 3.1$ pm over the total acquisition time. This slow spectral shift can be
attributed to the gradual increase of the chamber relative humidity towards its saturation
value. With higher humidity, the condensation rate increases and, thus, new equilibrium
between evaporation and condensation is established at a slightly longer wavelength closer
to the heating beam resonance. $\Delta\lambda$ can be converted into the residual drift of the droplet
radius Δa as $\Delta a = \Delta\lambda(a/\lambda_P)$ [113]. For $a = 245\,\mu$m and $\lambda_P = 638$ nm, $\Delta a = 1.2$ nm. For
times 410 s $< t < 430$ s, the heating laser was blocked which resulted in a large spectral
drift of the droplet WGMs towards the red end of the spectrum due to condensation in the
chamber. Subsequently, the heating laser was unblocked again, starting at time $t = 430$
s until the final acquisition time $t = 635$ s. During this period, spectral positions of the
WGMs were again almost constant, suggesting size-stabilization of the microdroplet with
a similar rate of the residual drift of the droplet size as in the first locking period. We
note that the spectral positions of the WGMs during the first ($t = \langle 0 - 410 \rangle$ s) and second
($t = \langle 430 - 635 \rangle$ s) size-stabilized periods are not the same (see Fig. 7.2(b)). This indicates
locking of the microdroplet to different absorption resonances of the heating laser which
correspond to different droplet sizes.

In order to study the dynamics of the droplet self-stabilization after a sudden change of
environmental conditions, we carried out experiments in which we periodically modulated
the heating laser power and monitored the droplet response. Figs. 7.3 and 7.4 provide an
illustration of the droplet size-locking dynamics. In Fig. 7.3(a), a low-Q WGM spectrum
of a size-stabilized droplet is shown ($Q \approx 2.1 \times 10^5$). After acquiring this spectrum, the
probe laser was tuned to the droplet WGM wavelength indicated by an arrow in Fig. 7.3(a).
Subsequently, the heating laser was repeatedly blocked for 100 ms and then unblocked again
and the taper transmission was simultaneously recorded at the fixed WGM wavelength.
The time trace of the recorded taper transmission is shown in Fig. 7.3(b). In the time
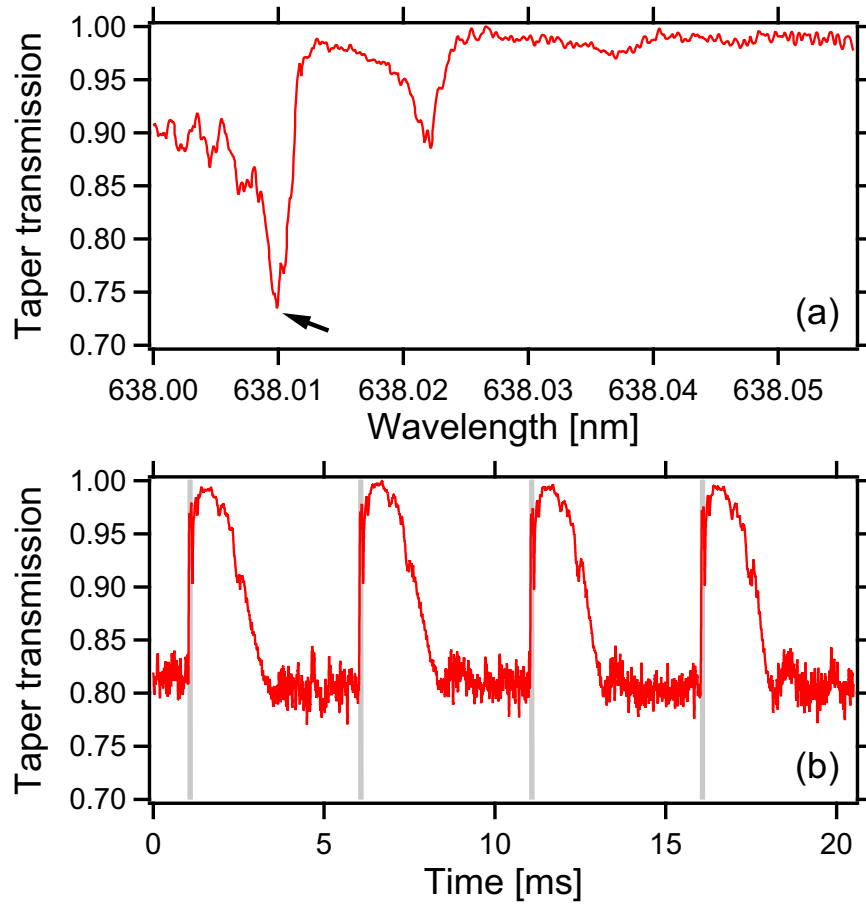
Figure 7.3: (a) Low-Q WGM spectrum of a size-locked microdroplet. (b) Time trace of the
taper transmission at a fixed wavelength of the probe laser denoted by arrow in (a). Gray
vertical stripes indicate time intervals during which the heating laser was blocked.

interval between 0 s and 1 s, the droplet size is locked and the taper transmission remains
constant at its minimum value corresponding to the WGM resonance. At time $t = 1$ s,
brief blocking of the heating laser leads to a fast increase of the droplet size. Since the
probe wavelength is fixed, such increase of the droplet size corresponds to an increase of
the droplet size parameter. This is equivalent to a shift to the blue-end of the spectrum
of Fig. 7.3(a) that was acquired with a constant droplet size and changing wavelength.
Thus, taper transmission quickly increases. After unblocking the heating laser, the droplet
starts evaporating again and the droplet size parameter eventually decreases back towards its
resonant value. This results in a gradual decrease of the taper transmission with an intensity
profile that follows the spectral features of the blue shoulder of the selected WGM resonance.
Fig. 7.4 shows a similar dynamic response recorded for a high-Q WGM ($Q \approx 1.4 \times 10^6$) with
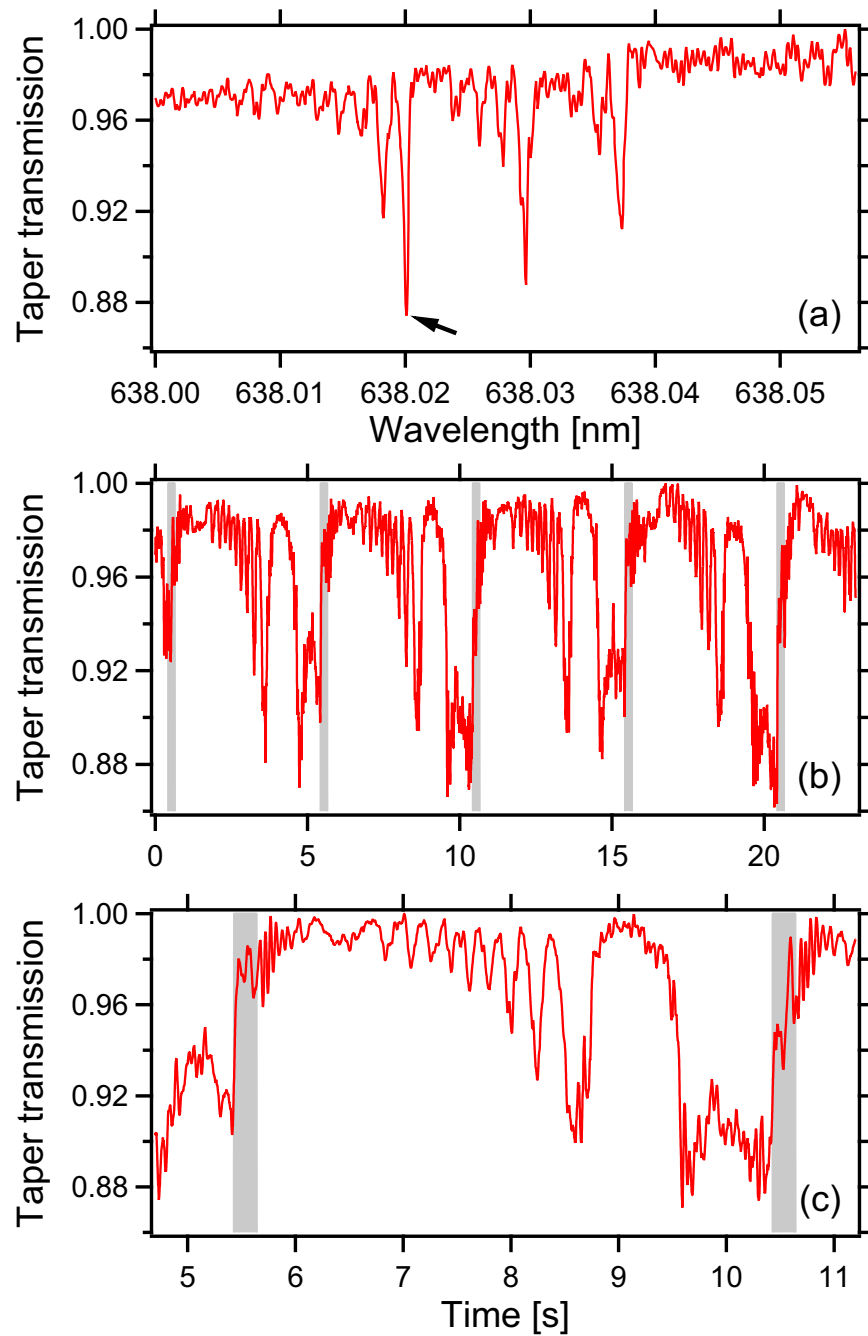
Figure 7.4: (a) High-Q WGM spectrum of a size-locked microdroplet. (b) Time trace of
the taper transmission at a fixed wavelength of the probe laser denoted by arrow in (a).
Gray vertical stripes indicate time intervals during which the heating laser was blocked. (c)
Detail of the time trace shown in (b).

a largely lifted degeneracy of the different azimuthal modes (see Fig. 7.4(a)). In this case,

the temporal profile of the taper transmission is rather complex, reflecting again the shape

of the spectrum in the blue shoulder of the selected WGM resonance. Indeed, the depths of individual spectral dips observed in the wavelength scan and the time trace (compare corresponding dip numbers in Figs. 7.4(a) and (c)) are in a good agreement. As shown in Figs. 7.3(b) and 7.4(b) upon repeated blocking of the heating laser, the shape of the temporal response remains almost constant. This indicates that the whole process is fully reversible.

7.5 Conclusion

We have demonstrated long-term self-stabilization of the size of salt-water microdroplets standing on a superhydrophobic surface and coupled to a tapered optical fiber guiding independent probe and heating lasers. The size self-stabilization resulted from the competition between resonant heating of the droplets by an infrared laser and water condensation in ambient environment with controlled relative humidity. Thanks to the narrow linewidth of the heating laser, stabilization of the microdroplet radius with a precision down to ~1.2 nm was achieved. This technique can be useful for ultrahigh-resolution characterization of liquid aerosols and applications of liquid optical microcavities which require size stabilization such as frequency combs [115].

Chapter 8

CONTROLLING WGMS OF SURFACE-SUPPORTED LIQUID AEROSOLS

8.1 Introduction

Liquid aerosols represent unique optical resonant microcavities that hold potential for many fields of research because of their high Q-factors and low mode volumes [85]. However, the use of droplet-based optical resonators in some applications which require controllable high resolution tuning and/or stabilization of high-Q whispering gallery modes (WGM) of the resonator (for example, sensing and cavity-quantum electrodynamics experiments), is challenging [116]. Recently, spectral tuning of WGMs of dye-doped droplets standing on a superhydrophobic surface by evaporation/condensation [93] and electric field [117] has been demonstrated. In these experiments, spectral positions and Q-factors of the droplet WGMs were determined from far-field fluorescence spectra. However, due to the limited resolution of optical spectroscopy, it was not possible to observe and control the spectral positions of high-Q modes with sufficient precision. In order to overcome this problem, we have recently introduced prolonged self-stabilization and high-resolution WGM characterization of single microdroplets standing on a superhydrophobic surface using a fixed wavelength heating infrared (IR) laser and tunable red probe laser which were coupled to the droplet with a tapered optical fiber waveguide [118]. In this chapter, we follow up on the previous stabilization experiments and demonstrate controllable tuning of WGMs of self-stabilized surface-supported liquid aerosol using a tunable IR heating laser which has a very narrow linewidth.

8.2 Experimental Setup

The experimental setup used for the size tuning and high-resolution spectroscopy of surface-supported liquid microdroplets is shown in Fig. 8.1. Superhydrophobic (SH) surfaces were prepared by spin coating of hydrophobically coated silica nanoparticles which were dissolved
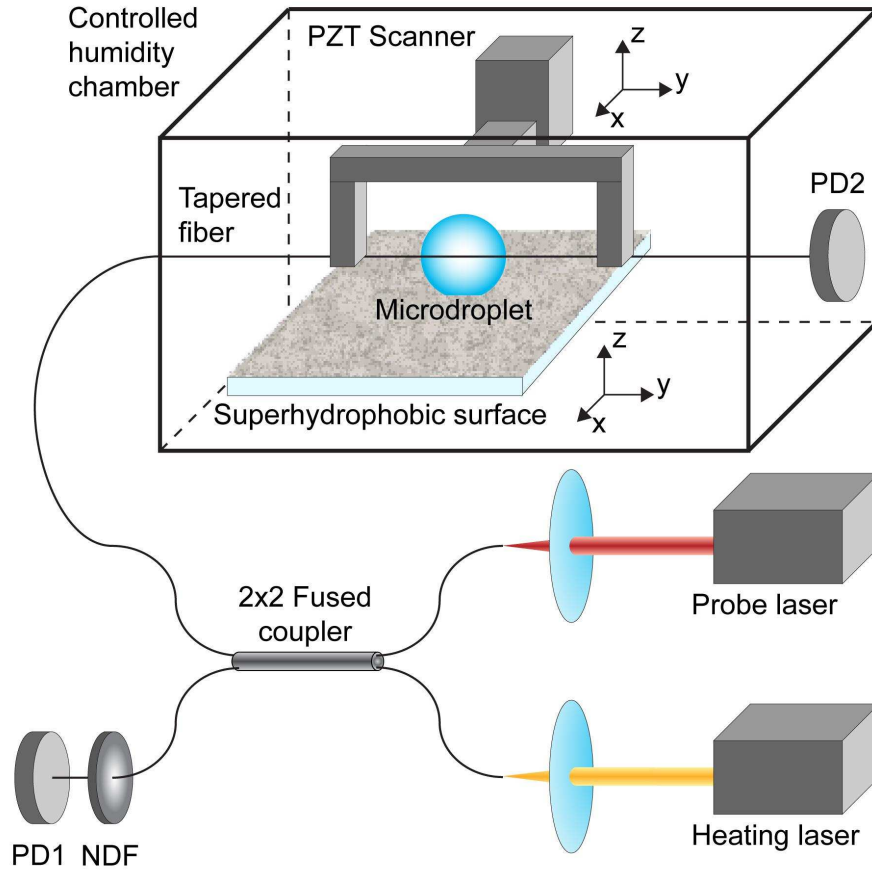
Figure 8.1: Experimental setup for self-stabilization of surface supported liquid microdroplets. PD1 (PD2) - photodetectors monitoring the light power at the input (output) of the tapered fiber, NDF -neutral density filter.

in isopropanol [118]. The deposition of individual microdroplets on SH surface was done manually by using a glass microcapillary connected to a syringe. We made use of LiCl-doped microdroplets, because the relative humidity of a saturated solution of LiCl is 11% it is much lower the room humidity 50% and, thus, the droplets containing this salt tend to evaporate less. The initial concentration of LiCl-water mixture was 2 mM. The microdroplet deposited on SH surface was placed in a sealed humidity chamber. The chamber humidity was fixed to 53% by using a saturated solution of $Mg(NO_3)_2$, because we need some initial condensation in the droplets that can be countered by the IR laser heating At this relative humidity and with an ambient temperature of ≈ 23 °C, the refractive index of LiCl-water microdroplet is $n_D = 1.347$ [27]. A fiber taper manufactured from a standard single mode optical fiber by

heat-and pull technique was used to couple light into and out of the microdroplet [10]. Using XYZ piezo-stage with 2 nm resolution, the fiber taper was positioned within the proximity of the droplet to allow evanescent coupling. A tunable probe external-cavity diode laser (λ_{probe} = 638 nm, tuning range 0.032 nm, linewidth <300 kHz) and a tunable heating external cavity diode laser (λ_H = 1500-1630 nm, linewidth <40 MHz) were coupled into the same tapered fiber. Lasers used in this demonstration have much narrower linewidths compared to those used in the previous demonstrations [110, 111, 112]. In order to minimize the absorption of the tunable probe laser light in the droplet liquid, we performed the measurements in the visible part of the spectrum where water is virtually non-absorbing. In contrast, the heating laser wavelength was selected to be in the near IR region where the water absorption is more than four orders of magnitude higher than at visible wavelengths. The probe laser power was monitored both at the input and the output of the tapered fiber and the measured taper transmission was normalized by the input power in order to eliminate the laser power variations during probe wavelength tuning. Both evaporation due to infrared laser heating and condensation due to high humidity within the sealed chamber have role in the self-stabilization process. As reported Karadag et al. [111], there is a certain size parameter $\alpha = 2\pi a/\lambda_H$ which the droplet of radius a is in resonance with the heating laser wavelength. At this certain droplet size, condensation rate and evaporation rate are equal, resulting in a stable droplet size. When the droplet is locked to the wavelength of the heating laser, its size can be tuned controllably by changing the heating laser wavelength.

8.3   Results

Figure 8.2a shows a taper transmission spectrum recorded with the tunable probe laser from a LiCl microdroplet with a 120 μm radius, the size of which was self-stabilized with the heating laser. The heating laser wavelength was fixed at 1558.220 nm. The Q-factor of WGM A was around 2×10^5. Figure 8.2b shows a two-dimensional plot of consecutive transmission spectra recorded from the same droplet. In this plot, horizontal axis corresponds to the spectral coordinate while the vertical axis corresponds to the number of acquisition. During 95 acquisitions, the IR laser wavelength was increased by 5 pm at each 5 acquisitions from 1558.220 nm to 1558.270 nm then decreased to 1558.220 nm. As expected, when we increase λ_H , at a given droplet size, size parameter becomes smaller than the equilibrium value at
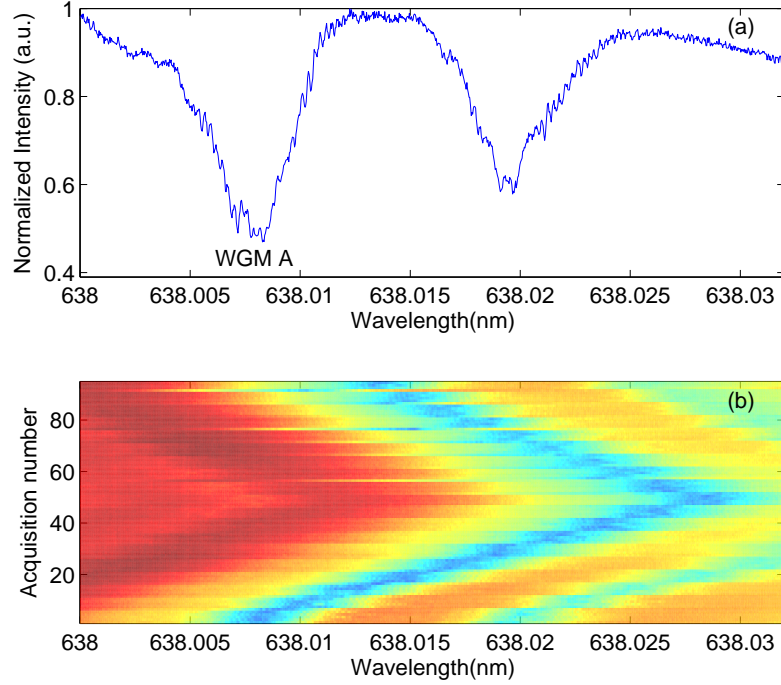
Figure 8.2: (a) WGM spectrum of a stabilized droplet recorded at a fixed wavelength of the heating laser. (b) 2D consecutive WGM spectra of the same droplet recorded for increasing (frames 1 to 50) and decreasing (frames 51 to 95) wavelength of the heating laser.

which condensation is balanced by evaporation. Thus, absorption decreases (we tune the droplet away from the resonance), condensation dominates, and the droplet grows in size. Intuitively, for a larger heating laser wavelength, we need a bigger droplet to fit the same number of wavelengths along the droplet perimeter in resonance. This size increase leads to a red-shift in spectral positions of WGMs of both heating and probe laser beams.

$$\frac{\Delta\lambda_{probe}}{\lambda_{probe}} = \frac{\Delta\lambda_H}{\lambda_H} = \frac{\Delta a}{a} \tag{8.1}$$

According to Eq. 8.1, 50 pm heating laser wavelength tuning ($\Delta\lambda_H$) reveals 20.5 pm probe laser wavelength tuning ($\Delta\lambda_{probe}$). As seen in Fig. 8.2, the red-shift of WGM A is around 20 pm during heating laser wavelength tuning. This result agrees well with the calculated value. However, there is a discrepancy between initial and final spectral positions of WGMs, after completing one tuning cycle. This spectral position difference was attributed

to the change of the droplet contact angle during evaporation [119] and wavelength accuracy of the heating laser.
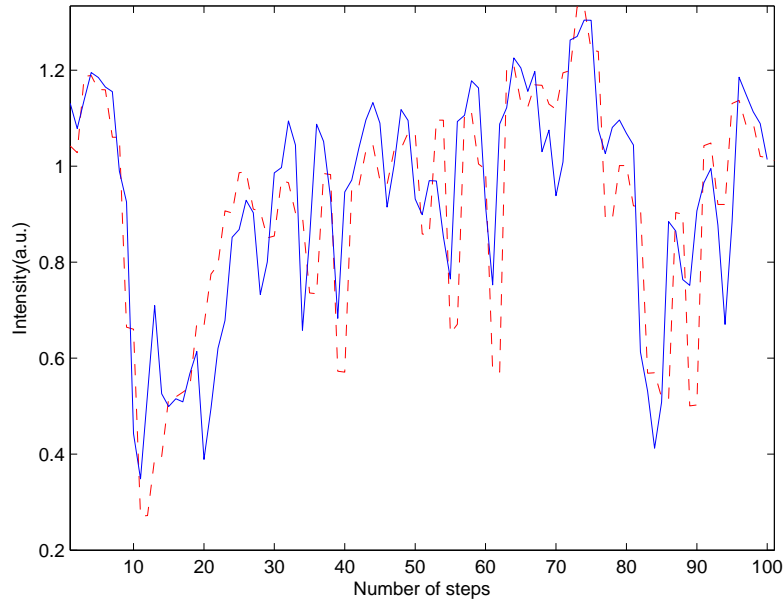
Figure 8.3: Tapered fiber transmission spectra from a self-stabilized droplet during forward and backward tuning of the heating laser wavelength λ_H. Probe laser wavelength was fixed at $\lambda_{probe} = 638$ nm.

Figure 8.3 shows normalized transmission intensity of the tapered fiber recorded during λ_H tuning cycle at a fixed λ_{probe} as a function of the number of tuning steps. The wavelength scan of λ_H was between 1550 nm and 1549 nm in 0.01 nm steps. Scanning of λ_H causes changes of the droplet size; if λ_{probe} is fixed, these size changes result in the modulation of the taper transmission as the droplets is gradually tuned in and out of resonance with λ_H. According to Eq. 8.1, 1 nm scan corresponds to 80 nm change in droplet radius. Despite this large radius change, spectral positions of WGMs during the forward and backward parts of the tuning cycle were almost preserved as shown in Fig. 8.3. The intensity difference of the same WGM between backward and forward scan indicates that the coupling efficiency between droplet and tapered fiber was different. According to asymptotic formula of Chylek et al. [120], free spectral range (FSR) of a 120 μm radius droplet for 1550 nm was calculated as 2.59 nm. Thus, in our 1 nm scan of the heating laser wavelength, we did not observe

periodically repeating WGM structure from which FSR could be determined.

8.4   Conclusion

As a conclusion, we have demonstrated controllable tuning of high-Q WGMs of self-stabilized droplet sustained on a superhydrophobic surface. It is possible to use this technique to obtain droplet-based tunable frequency combs [121] and add-drop filters [122].

Chapter 9

CONCLUSION

In this thesis, ultrahigh Q-factors of microdroplets standing on superhydropbobic sur-
face were investigated as a tool for optofluidic applications. First, to gain a better under-
standing, basic properties of the microsphere microcavity were summarized. The resonance
wavelengths of the microsphere, which were the solutions of Maxwell equations fulfilling
boundary conditions at the sphere surface were calculated.

In the following chapter, superhydrophobic surface preparation was explained. Then
lumped system formulation of the mass and heat transfer between the microdroplet and
the chamber was given. The modified absorption efficiency ($\tilde{Q}_{abs}$) of a spherical parti-
cle suspended in air was calculated using the localized approximation to the beam-shape
coefficients in generalized Lorenz-Mie theory.

Initial experiments were done by using free-space excitation of WGMs in surface-supported
microdroplets. A novel method for the microscopic contact angle measurement was pre-
sented that is based on the analysis of mechanical resonances of individual micrometer–
sized liquid droplets supported by a vibrated SH surface or oscillatory deformations of
micrometer-sized NaCl-water droplets by an AC electric field. In addition to that a QPD
(quadrant photodiode) instead of optical spectroscopy of WGMs was used to analyze the
mechanical resonances of microdroplets standing on a superhydrophobic surface.

A sub-micron tapered optical fiber waveguide was manufactured to couple light from
a narrow-linewidth tunable laser into an individual surface-supported droplet of glycerol-
water mixture and measured the fiber transmission as a function of the laser wavelength
was measured. Linewidth-based measurements of ultrahigh-Q factors of individual optical
resonances excited in liquid microdroplets were reported.

Long-term size-stabilization resulting from balance between the condensation in a high-
humidity chamber and shrinkage due to the evaporation of individual microdroplets standing
on a SH surface and coupled to single tapered optical fibers which guide simultaneously a

tunable red laser for the WGM probing and an infrared (IR) heating laser was achieved. In addition to self-stabilization we demonstrated controllable tuning of WGMs of self-stabilized surface-supported liquid aerosol using a tunable IR heating laser which has a very narrow linewidth. Fine control of WGMs of microdroplets can has potential applications in chemical and biological sensing and also in frequency comb generation.

BIBLIOGRAPHY

[1] D. Psaltis, S. R. Quake, and C. Yang, "Developing optofluidic technology through the fusion of microfluidics and optics," Nature **442**, 381–386 (2006).

[2] M. Li and C. K. Ober, "Block copolymer patterns and templates," Materials Today **9**, 30–39 (2006).

[3] M. H. Fields, J. Popp, and R. K. Chang, "Nonlinear optics in microspheres," in "Progress in Optics," , vol. 41, E. Wolf, ed. (Elsevier, 2000), pp. 1–95.

[4] A. Kiraz, A. Kurt, M. A. Dündar, and A. L. Demirel, "Simple largely tunable optical microcavity," Appl. Phys. Lett. **89**, 081118 (2006).

[5] S. Arnold, M. Neuman, and A. B. Pluchino, "Molecular spectroscopy of a single aerosol particle," Opt. Lett. **9**, 4–6 (1984).

[6] A. Ashkin and J. M. Dziedzic, "Optical levitation of liquid drops by radiation pressure," Science **187**, 1073 (1975).

[7] R. J. Hopkins, L. Mitchem, A. D. Ward, and J. P. Reid, "Control and characterisation of a single aerosol droplet in a single-beam gradient-force optical trap," Phys. Chem. Chem. Phys. **6**, 4924 (2004).

[8] T. A. Birks and Y. W. Li, "The shape of fiber tapers," J. Lightwave Technol. **10**, 432–438 (1992).

[9] A. Serpengüzel, J. C. Swindal, R. K. Chang, and W. P. Acker, "Two-dimensional imaging of sprays with fluorescence, lasing, and stimulated Raman scattering," Appl. Opt. **31**, 3543–3551 (1992).

[10] J. C. Knight, G. Cheung, F. Jacques, and T. A. Birks, "Phase-matched excitation of whispering-gallery-mode resonances by a fiber taper," Opt. Lett. **22**, 1129–1131 (1997).

[11] Y. Karadag, "Spectral tuning of liquid microdroplets standing on a superhydrophobic surface by using a focused infrared laser or electrowetting," Master's thesis, Koc Universty (2009).

[12] M. A. Dundar, "Inducing a novel optical microcavity: A glycerol/water microdroplet on a superhydrophobic surface," Master's thesis, Koc Universty (2007).

[13] A. Checco, P. Guenoun, and J. Daillant, "Nonlinear dependence of the contact angle of nanodroplets on contact line curvature," Phys. Rev. Lett. **91**, 186101 (2003).

[14] H. Azzouz, "Liquid droplet dye laser," Master's thesis, Technical Universty of Denmark (2005).

[15] G. Grehan, B. Maheu, and G. Gouesbet, "Scattering of laser beams by mie scatter centers: numerical results using a localized approximation," Appl. Opt. **25**, 3539–3548 (1986).

[16] J. A. Lock, "Improved gaussian beam-scattering algorithm," Appl. Opt. **34**, 559–570 (1995).

[17] J. A. Lock, "Excitation efficiency of a morphology-dependent resonance by a focused gaussian beam," J. Opt. Soc. Am. A **15**, 2986–2994 (1998).

[18] A. K. Ray, R. D. Johnson, and A. Souyri, "Dynamic behavior of single glycerol droplets in humid air streams," Langmuir **5**, 133–140 (1989).

[19] H. Tu and A. K. Ray, "Measurement of activity coefficients from unsteady state evaporation and growth of microdroplets," Chem. Eng. Comm. **192**, 474–498 (2005).

[20] R. G. Picknett and R. J. Bexon, "The evaporation of sessile or pendant drops in still air," J. Colloid Interface Sci. **61**, 336–350 (1977).

[21] G. McHale, S. Aqil, N. J. Shirtcliffe, M. I. Newton, and H. Y. Erbil, "Analysis of droplet evaporation on a superhydrophobic surface," Langmuir **21**, 11053–11060 (2005).

[22] S.-X. Qian, J. B. Snow, H. M. Tzeng, and R. K. Chang, "Lasing droplets: Highlighting the liquid-air interface by laser emission," Science **231**, 486 (1986).

[23] V. V. Datsyuk, "Optics of microdroplets," J. Mol. Liq. **84**, 1308–1316 (2001).

[24] I. N. Tang, A. C. Tridico, and K. H. Fung, "Thermodynamic and optical properties of sea salt aerosols," J. Geophys. Res. **102**, 23269–23275 (1997).

[25] D. Segelstein, "The complex refractive index of water," Master's thesis, University of Missouri, Kansas City (1981).

[26] E. J. G. Peterman, F. Gittes, and C. F. Schmidt, "Laser-induced heating in optical traps," Biophys. J. **84**, 1308–1316 (2003).

[27] D. R. Lide, *CRC Handbook of Chemistry and Physics, Internet Version 2012, <http://www.hbcpnetbase.com>* (CRC Press, 2012).

[28] G. Gouesbet and J. A. Lock, "Rigorous justification of the localized approximation to the beam-shape coefficients in generalized lorenz-mie theory. ii. off-axis beams," J. Opt. Soc. Am. A **11**, 2516–2525 (1994).

[29] J. P. Barton, D. R. Alexander, and S. A. Schaub, "Internal and near-surface electromagnetic fields for a spherical particle irradiated by a focused laser beam," J. Appl. Phys. **64**, 1632–1639 (1988).

[30] J. P. Barton, D. R. Alexander, and S. A. Schaub, "Internal fields of a spherical particle illuminated by a tightly focused laser beam: Focal point positioning effects at resonance," J. Appl. Phys. **65**, 2900–2906 (1989).

[31] J. A. Lock and G. Gouesbet, "Rigorous justification of the localized approximation to the beam-shape coefficients in generalized lorenz-mie theory. i. on-axis beams," J. Opt. Soc. Am. A **11**, 2503–2515 (1994).

[32] M. Nosonovsky and B. Bhushan, "Superhydrophobic surfaces and emerging applications: Non-adhesion, energy, green engineering," Curr. Opin. Colloid Interface Sci. **14**, 270–280 (2009).

[33] B. Bhushan, "Nanotribology and nanomechanics of mems/nems and biomems/bionems materials and devices," Microelectron. Eng. **84**, 387–412 (2007).

[34] J. P. Rothstein, "Slip on superhydrophobic surfaces," Annu. Rev. Fluid Mech. **42**, 89–109 (2010).

[35] P. G. de Gennes, "Wetting: statics and dynamics," Rev. Mod. Phys. **57**, 827–863 (1985).

[36] K. K. S. Lau, J. Bico, K. B. K. Teo, M. Chhowalla, G. A. J. Amaratunga, W. I. Milne, G. H. McKinley, and K. K. Gleason, "Superhydrophobic carbon nanotube forests," Nano Lett. **3**, 1701–1705 (2003).

[37] C. Journet, S. Moulinet, C. Ybert, S. T. Purcell, and L. Bocquet, "Contact angle measurements on superhydrophobic carbon nanotube forests: Effect of fluid pressure," Europhys. Lett. **71**, 104–109 (2005).

[38] Y.-L. Hung, Y.-Y. Chang, M.-J. Wang, and S.-Y. Lin, "A simple method for measuring the superhydrophobic contact angle with high accuracy," Rev. Sci. Instrum. **81**, 065105 (2010).

[39] Y.-T. Cheng, D. E. Rodak, A. Angelopoulos, and T. Gacek, "Microscopic observations of condensation of water on lotus leaves," Appl. Phys. Lett. **87**, 194112 (2005).

[40] M. Strani and F. Sabetta, "Free vibrations of a drop in partial contact with a solid support," J. Fluid Mech. **141**, 233–247 (1984).

[41] R. W. Smithwick and J. A. M. Boulet, "Vibrations of microscopic mercury droplets on glass," J. Colloid Interface Sci. **130**, 588–596 (1989).

[42] S. Yamakita, Y. Matsui, and S. Shiokawa, "New method for measurement of contact angle (droplet free vibration frequency method)," Jpn. J. Appl. Phys. **38**, 3127–3130 (1999).

[43] A. Kiraz, Y. Karadag, S. C. Yorulmaz, and M. Muradoglu, "Reversible photothermal tuning of a salty water microdroplet," Phys. Chem. Chem. Phys. **11**, 2597–2560 (2009).

[44] X. Noblin, A. Buguin, and F. Brochard-Wyart, "Vibrated sessile drops: Transition between pinned and mobile contact line oscillations," Eur. Phys. J. E **14**, 395–404 (2004).

[45] F. Celestini and R. Kofman, "Vibration of submillimeter-size supported droplets," Phys. Rev. E **73**, 041602 (2006).

[46] G. McHale, S. J. Elliott, M. I. Newton, D. L. Herbertson, and K. Esmer, "Levitation-free vibrated droplets: Resonant oscillations of liquid marbles," Langmuir **25**, 529–533 (2009).

[47] J. D. Eversole, H.-B. Lin, and A. J. Campillo, "Cavity-mode identification of fluorescence and lasing in dye-doped microdroplets," Appl. Opt. **31**, 1982–1991 (1992).

[48] J. D. Eversole, H.-B. Lin, and A. J. Campillo, "Input/output resonance correlation in laser-induced emission from microdroplets," J. Opt. Soc. Am. B **12**, 287 (1995).

[49] M. Y. Yüce, A. L. Demirel, and F. Menzel, "Tuning the surface hydrophobicity of polymer/nanoparticle composite films in the wenzel regime by composition," Langmuir **21**, 5073 (2005).

[50] A. Marmur, "Thermodynamic aspects of contact angle hysteresis," Adv. Colloid Interface Sci. **50**, 121–141 (1994).

[51] M. Y. Yüce, "Preparation and characterization of hydrophobic surfaces," Master's thesis, Koç University (2006).

[52] S. C. Yorulmaz, M. Mestre, M. Muradoglu, B. E. Alaca, and A. Kiraz, "Controlled observation of nondegenerate cavity modes in a microdroplet on a superhydrophobic surface," Opt. Commun. **282**, 3024–3027 (2009).

[53] M. Nosonovsky, "Multiscale roughness and stability of superhydrophobic biomimetic interfaces," Langmuir **23**, 3157–3161 (2007).

[54] N. J. Shirtcliffe, G. McHale, M. I. Newton, G. Chabrol, and C. C. Perry, "Dual-scale roughness produces unusually water-repellent surfaces," Adv. Mater. **16**, 1929–1932 (2004).

[55] S. Mettu and M. K. Chaudhury, "Stochastic relaxation of the contact line of a water drop on a solid substrate subjected to white noise vibration: Roles of hysteresis," Langmuir **26**, 8131–8140 (2010).

[56] T. S. Meiron, A. Marmur, and I. S. Saguy, "Contact angle measurement on rough surfaces," J. Colloid Interface Sci. **274**, 637–644 (2004).

[57] E. Bormashenko, R. Pogreb, G. Whyman, and M. Erlich, "Resonance cassie-wenzel wetting transition for horizontally vibrated drops deposited on a rough surface," Langmuir **23**, 12217–12221 (2007).

[58] S. K. Y. Tang, R. Derda, Q. Quan, M. Loncar, and G. M. Whitesides, "Continuously tunable microdroplet-laser in a microfluidic channel," Opt. Express **19**, 2204–2215 (2011).

[59] A. Jonas, Y. Karadag, N. Tasaltin, I. Kucukkara, and A. Kiraz, "Probing microscopic wetting properties of superhydrophobic surfaces by vibrated micrometer-sized droplets," Langmuir **27**, 2150–2154 (2011).

[60] S. Torza, R. G. Cox, and S. G. Mason, "Electrohydrodynamic deformation and burst of liquid drops," Phil. Trans. R. Soc. A **269**, 295–319 (1971).

[61] N. Bentenitis and S. Krause, "Droplet deformation in dc electric fields: The extended leaky dielectric model," Langmuir **21**, 6194–6209 (2005).

[62] R. W. Smithwick and J. A. M. Boulet, "Electrically driven oscillations of a mercury-droplet electrode," J. Colloid Interface Sci. **150**, 567–574 (1992).

[63] T. Yamada, T. Sugimoto, Y. Higashiyama, M. Takeishi, and T. Aoki, "Resonance phenomena of a single water droplet located on a hydrophobic sheet under ac electric field," IEEE Transactions on Industry Applications **39**, 59–65 (2003).

[64] H. A. Haus, *Waves and Fields in Optoelectronics* (Prentice-Hall, 1984).

[65] G. C. Righini, Y.Dumeige, P. Feron, M. Ferrari, G. N. Conti, D. Ristic, and S. Soria, "Whispering gallery mode microresonators: Fundamentals and applications," Rivista Del Nuovo Cimento **34**, 435–488 (2011).

[66] Y. Treussart, V. S. Ilchenko, J. Roch, J. Hare, V. L. Seguin, J. Raimond, and S. Haroche, "Evidence for intrinsic kerr bistability of high-q microsphere resonators in superfluid helium," Eur. Phys. J. D **1**, 235–238 (1998).

[67] V. Braginsky, M. Gorodetsky, and V. Ilchenko, "Quality-factor and nonlinear properties of optical whispering-gallery modes," Physics Letters A **137**, 393–397 (1989).

[68] M. L. Gorodetsky and V. S. Ilchenko, "Optical microsphere resonators: optimal coupling to high-q whispering-gallery modes," JOSA B **16**, 147–154 (1999).

[69] V. S. Ilchenko, X. S. Yao, and L. Maleki, "Pigtailing the high-q microsphere cavity: a simple fiber coupler for optical whispering-gallery modes," Optics Letters **24**, 723–725 (1999).

[70] M. Cai, O. Painter, and K. J. Vahala, "Observation of critical coupling in a fiber taper to a silica-microsphere whispering-gallery mode system," Phys. Rev. Lett. **85**, 74–77 (2000).

[71] A. Boleininger, T. Lake, S. Hami, and C. Vallance, "Whispering gallery modes in standard optical fibres for fibre profiling measurements and sensing of unlabelled chemical species," Sensors **10**, 1765–1781 (2010).

[72] K. J. Vahala, "Optical microcavities," Nature **424**, 839 (2003).

[73] T. J. Kippenberg and K. J. Vahala, "Cavity opto-mechanics," Opt. Express **15**, 17172–17205 (2007).

[74] A. M. Armani, R. P. Kulkarni, S. E. Fraser, R. C. Flagan, and K. J. Vahala, "Label-free, single-molecule detection with optical microcavities," Science **317**, 783–787 (2007).

[75] F. Vollmer and S. Arnold, "Whispering-gallery-mode biosensing: label-free detection down to single molecules," Nature Methods **5**, 591–596 (2008).

[76] P. Chylek, "Resonance structure of Mie scattering: distance between resonances," J. Opt. Soc. Am. A **7**, 1609–1613 (1990).

[77] J. D. Eversole, H.-B. Lin, A. L. Huston, A. J. Campillo, P. T. Leung, S. Y. Liu, and K. Young, "High-precision identification of morphology-dependent resonances in optical processes in microdroplets," J. Opt. Soc. Am. B **10**, 1955–1968 (1993).

[78] H.-B. Lin, A. L. Huston, B. L. Justus, and A. J. Campillo, "Some characteristics of a droplet whispering-gallery-mode laser," Opt. Lett. **11**, 614–616 (1986).

[79] H. B. Lin, J. D. Eversole, and A. J. Campillo, "Spectral properties of lasing microdroplets," J. Opt. Soc. Am. B **9**, 43–50 (1992).

[80] A. Kiraz, A. Sennaroglu, S. Doganay, M. A. Dundar, A. Kurt, H. Kalaycioglu, and A. L. Demirel, "Lasing from single, stationary, dye-doped glycerol/water microdroplets located on a superhydrophobic surface," Opt. Commun. **276**, 145–148 (2007).

[81] M. Tanyeri, R. Perron, and I. M. Kennedy, "Lasing droplets in a microfabricated channel," Opt. Lett. **32**, 2529–2531 (2007).

[82] S. K. Y. Tang, Z. Li, A. R. Abate, J. J. Agresti, D. A. Weitz, D. Psaltis, and G. M. Whitesides, "A multi-color fast-switching microfluidic droplet dye laser," Lab Chip **9**, 2767–2771 (2009).

[83] J. B. Snow, S.-X. Qian, and R. K. Chang, "Stimulated Raman scattering from individual water and droplets at morphology-dependent resonances," Opt. Lett. **10**, 37–39 (1985).

[84] H. B. Lin, J. D. Eversole, and A. J. Campillo, "Continuous-wave stimulated Raman scattering in microdroplets," Opt. Lett. **17**, 828–830 (1992).

[85] R. Symes, R. M. Sayer, and J. P. Reid, "Cavity enhanced droplet spectroscopy: Principles, perspectives and prospects," Phys. Chem. Chem. Phys. **6**, 474–487 (2004).

[86] A. Sennaroglu, A. Kiraz, M. A. Dündar, A. Kurt, and A. L. Demirel, "Raman lasing near 630 nm from stationary glycerol-water microdroplets on a superhydrophobic surface," Opt. Lett. **32**, 2197–2199 (2007).

[87] Y. Karadag, M. Gündoğan, M. Y. Yüce, H. Cankaya, A. Sennaroglu, and A. Kiraz, "Prolonged Raman lasing in size-stabilized salt-water microdroplets on a superhydrophobic surface," Opt. Lett. **35**, 1995–1997 (2010).

[88] J.-Z. Zhang, D. H. Leach, and R. K. Chang, "Photon lifetime within a droplet: temporal determination of elastic and stimulated Raman scattering," Opt. Lett. **13**, 270–272 (1988).

[89] S. Arnold and L. M. Folan, "Energy transfer and the photon lifetime within an aerosol particle," Opt. Lett. **14**, 387–389 (1989).

[90] P. T. Leung and K. Young, "Theory of enhanced energy transfer in an aerosol particle," J. Chem. Phys. **89**, 2894–2899 (1988).

[91] M. Hossein-Zadeh and K. J. Vahala, "Fiber-taper coupling to whispering-gallery modes of fluidic resonators embedded in a liquid medium," Opt. Express **14**, 10800–10810 (2006).

[92] F. Orucevic, V. Lefevre-Seguin, and J. Hare, "Transmittance and near-field characterization of sub-wavelength tapered optical fibers," Opt. Express **15**, 13624–13626 (2007).

[93] A. Kiraz, Y. Karadağ, and M. Muradoğlu, "Large spectral tuning of a water/glycerol microdroplet by a focused laser: Characterization and modeling," Phys. Chem. Chem. Phys. **10**, 6446–6454 (2008).

[94] M. Born and E. Wolf, *Principles of Optics: Electromagnetic Theory of Propagation, Interference and Diffraction of Light* (Cambridge University Press, 1999), 7th ed.

[95] P. Chylek, "Partial-wave resonances and the ripple structure in the Mie normalized exctinction cross section," J. Opt. Soc. Am. **66**, 285–287 (1976).

[96] J. C. Waters, "Accuracy and precision in quantitative fluorescence microscopy," J. Cell Biol. **185**, 1135–1148 (2012).

[97] H. M. Lai, P. T. Leung, K. Young, P. W. Barber, and S. C. Hill, "Time–independent perturbation for leaking electromagnetic modes in open systems with application to resonances in microdroplets," Phys. Rev. A **41**, 5187–5198 (1990).

[98] G. Chen, M. M. Mazumder, Y. R. Chemla, A. Serpengüzel, R. K. Chang, and S. C. Hill, "Wavelength variation of laser emission along the entire rim of slightly deformed microdroplets," Opt. Lett. **18**, 1993–1995 (1993).

[99] V. A. Lubarda and K. A. Talke, "Analysis of the equilibrium droplet shape based on an ellipsoidal droplet model," Langmuir **27**, 10705–10713 (2011).

[100] S. Arnold, R. Ramjit, D. Keng, V. Kolchenko, and I. Teraoka, "Microparticle photophysics illuminates viral bio-sensing," Faraday Discuss. **137**, 65–83 (2008).

[101] M. L. Gorodetsky, A. A. Savchenkov, and V. S. Ilchenko, "Ultimate Q of optical microsphere resonators," Opt. Lett. **21**, 453–455 (1996).

[102] H. M. Lai, C. C. Lam, P. T. Leung, and K. Young, "Effect of perturbations on the widths of narrow morphology–dependent resonance in Mie scattering," J. Opt. Soc. Am. B **8**, 1962–1973 (1991).

[103] G. M. Hale and M. R. Querry, "Optical constants of water in the 200-nm to 200 um wavelength region," Appl. Opt. **12**, 555–563 (1973).

[104] L. F. Phillips, "A geometrical explanation for the enhanced small–scale roughness of a liquid surface," J. Phys. Chem. B **108**, 1986–1991 (2004).

[105] H. M. Lai, P. T. Leung, and K. Young, "Limitations on the photon storage lifetime in electromagnetic resonances of highly transparent microdroplets," Phys. Rev. A **41**, 5199–5204 (1990).

[106] J. P. Reid and L. Mitchem, "Laser probing of single-aerosol droplet dynamics," Annu. Rev. Phys. Chem. **57**, 245–271 (2006).

[107] D. McGloin, D. R. Burnham, M. D. Summers, D. Rudd, N. Dewar, and S. Anand, "Optical manipulation of airborne particles: techniques and applications," Faraday Discuss. **137**, 335–350 (2008).

[108] S. Arnold and L. M. Folan, "Fluorescence spectrometer for a single electrodynamically levitated microparticle," Rev. Sci. Inst. **57**, 2250 (1986).

[109] H. Azzouz, L. Alkhafadiji, S. Balslev, J. Johansson, N. A. Mortensen, S. Nilsson, and A. Kristensen, "Levitated droplet dye laser," Opt. Express **14**, 4374–4379 (2006).

[110] A. Kiraz, A. Kurt, M. A. Dündar, M. Y. Yüce, and A. L. Demirel, "Volume stabilization of single, dye-doped water microdroplets with femtoliter resolution," J. Opt. Soc. Am. B **24**, 1824–1828 (2007).

[111] Y. Karadag, M. Mestre, and A. Kiraz, "Photothermal self-stability and optical bista-bility of a nacl-water microdroplet on a superhydrophobic surface," Phys. Chem. Chem. Phys. **11**, 7145–7151 (2009).

[112] M. Guillon, R. E. H. Miles, J. P. Reid, and D. McGloin, "Thermo-optical resonance locking of an optically trapped salt-water microdroplet," New J. Phys. **11**, 103041 (2009).

[113] A. Jonáš, Y. Karadag, M. Mestre, and A. Kiraz, "Probing of ultrahigh optical q-factors of individual liquid microdroplets on superhydrophobic surfaces using tapered optical fiber waveguides," J. Opt. Soc. Am. B **29**, 3240–3247 (2012).

[114] T. Carmon, L. Yang, and K. J. Vahala, "Dynamical thermal behavior and thermal self-stability of microcavities," Opt. Express **12**, 4742–4750 (2004).

[115] P. Del'Haye, A. Schliesser, O. Arcizet, T. Wilken, R. Holzwarth, and T. J. Kippenberg, "Optical frequency comb generation from a monolithic microresonator," Nature **450**, 1214–1217 (2007).

[116] M. Pllinger, D. O'Shea, F. Warken, and A. Rauschenbeutel, "Ultrahigh-q tunable whispering-gallery-mode microresonator," Phys. Rev. Lett. **103**, 053901 (2009).

[117] A. Kiraz, Y. Karadağ, and A. F. Coskun, "Spectral tuning of liquid microdroplets standing on a superhydrophobic surface using electrowetting," Appl. Phys. Lett. **92**, 191104 (2008).

[118] Y. Karadag, A. Jonáš, I. Kucukkara, and A. Kiraz, "Size-stabilization of surface-supported liquid aerosols using tapered optical fiber coupling," Opt. Lett. **38(10)**, 793–795 (2013).

[119] X. Chen, R. Ma, J. Li, C. Hao, W. Gao, B. L. Luk, S. C. Li, S. Yao, and Z. Wang, "Evaporation of droplets on superhydrophobic surfaces: Surface roughness and small droplet size effects," Phys. Rev. Lett. **109**, 116101 (2012).

[120] P. Chylek, J. T. Kiehl, and M. K. W. Ko, "Optical levitation and partial-wave reso-
nances," Physical Review A: Atomic, Molecular, and Optical Physics **18**, 2229 (1978).

[121] A. A. Savchenkov, A. B. Matsko, V. S. Ilchenko, I. Solomatine, D. Seidel, and
L. Maleki, "Tunable optical frequency comb with a crystalline whispering gallery
mode resonator," Phys. Rev. Lett. **101**, 093902 (2008).

[122] F. Monifi, J. Friedlein, S. K. Ozdemir, and L. Yang, "A robust and tunable add-drop
filter using whispering gallery mode microtoroid resonator," Journal of Lightwave
Technology **21**, 3306–3315 (2012).

VITA

Yasin Karadağ was born in Istanbul, Turkey on November 1, 1983. He received his B.Sc. degree in physics from Bilkent University, Ankara, Turkey, in 2007. He joined the M.Sc. program in Physics at Koç University in 2007. He received his M.Sc. degree from Koç University in 2009. His master thesis work was titled as *Spectral Tuning of Liquid Microdroplets Standing on a Superhydrophobic Surface by Using a Focused Infrared Laser or Electrowetting.* He has been a doctoral student in Koç University Physics Department since 2009. He is a student member of International Society for Optical Engineering (SPIE) and Optical Society of America(OSA).

List of Publications

1. A. Kiraz, S. Ç. Yavuz, Y. Karadağ, A. Kurt, A. Sennaroglu, and H. Çankaya. "Large spectral tuning of liquid microdroplets standing on a superhydrophobic surface using optical scattering force" Appl. Phys. Lett. **91**, 231102 (2007)

2. A. Kiraz, Y. Karadağ, and A. F. Coskun. "Spectral tuning of liquid microdroplets standing on a superhydrophobic surface using electrowetting" Appl. Phys. Lett. **92**, 191104 (2008)

3. A. Kiraz, Y. Karadağ, and M. Muradoğlu. "Large spectral tuning of a water-glycerol microdroplet by a focused laser: characterization and modeling" Phys. Chem. Chem. Phys. **10**, 6446-6454 (2008)

4. A. Kiraz, Y. Karadag, S. C. Yorulmaz, and M. Muradoglu. "Reversible photothermal tuning of a salty water microdroplet" Phys. Chem. Chem. Phys. **11**, 2597-2600 (2009)

5. Y. Karadag, M. Mestre, and A. Kiraz, "Photothermal self-stability and optical bistability of single NaCl-water microdroplets on a superhydrophobic surface", Phys. Chem. Chem. Phys. **11**, 7145-7151 (2009)

6. M. Mestre, Y. Karadag, S. C. Yorulmaz, M. Gundogan, and A. Kiraz, "Photothermal Tuning and Size Locking of Salt-Water Microdroplets on a Superhydrophobic Surface", Int. J. Optomechatronics 3 (4), 303-318 (2009)

7. Y. Karadag, M. Gundogan, M. Y. Yuce, H. Cankaya, A. Sennaroglu, and A. Kiraz, "Prolonged Raman lasing in size-stabilized salt-water microdroplets on a superhydrophobic surface", Opt. Lett. **35** (12), 1995-1997 (2010)

8. A. Jonáš, Y. Karadag, N. Tasaltin, I. Kucukkara, and A. Kiraz, "Probing Microscopic Wetting Properties of Superhydrophobic Surfaces by Vibrated Micrometer-Sized Droplets", Langmuir **27** (6), 2150-2154 (2011)

9. Y. Karadag, A. Jonáš, N. Tasaltin, and A. Kiraz, "Determination of Microdroplet Contact Angles Using Electrically Driven Droplet Oscillations", Appl. Phys. Lett. **98**, 194101 (2011)

10. A. Jonáš, Y. Karadag, M. Mestre, and A. Kiraz, "Probing of ultrahigh optical Q-factors of individual liquid microdroplets in air using tapered optical fiber waveguides", J. Opt. Soc. Am. B **29** (12) 3240-3247 (2012)

11. Y. Karadag, A. Jonáš, I. Kucukkara, and A. Kiraz, "Size-stabilization of surface-supported liquid aerosols using tapered optical fiber coupling", Opt. Lett. **38** (5), 793-795 (2013)

12. Y. Karadag , M. Aas, A. Jonáš, S. Anand, D. McGloin, and A. Kiraz, "Dye lasing in optically manipulated liquid aerosols", Opt. Lett. **38** (10), 1669-1671 (2013)